8-2014

A Spectroscopic Study of Anomalous Stellar Populations in M67

Courtney McGahee
Clemson University, cmcgahe@g.clemson.edu

A Spectroscopic Study of Anomalous Stellar Populations in M67

A Dissertation
Presented to
the Graduate School of
Clemson University

In Partial Fulfillment
of the Requirements for the Degree
Doctor of Philosophy
Physics

---

by
Courtney Elizabeth McGahee
August 2014

Accepted by:
Dr. Jeremy King, Committee Chair
Dr. Sean Brittain
Dr. Bradley Meyer
Dr. Jens Oberheide

Abstract

A population of stars exists in the old, open cluster M67, whose photometry, color magnitude diagram locations and associated evolutionary states cannot be explained by current, standard single star evolution theory. These stars are often referred to as "yellow straggler" stars. Yellow stragglers have been identified in multiple star clusters suggesting that these stars constitute a real population. Additionally, according to independent studies, at least some of the yellow straggler stars in M67 are likely cluster members. Therefore, cluster non-membership is not a sufficient explanation for the observed anomalous photometry of these stars.

It is possible that the yellow stragglers occupy their precarious color magnitude diagram positions as a result of the evolution of mass transfer blue straggler stars. These are stars which have been formed by Roche Lobe overflow mass transfer in close binary systems. If this the case for the yellow stragglers, it is hypothesized that they could potentially exhibit two spectroscopic characteristics that can be indicative of this type of mass transfer system. Specifically, variable radial velocities can be used to indicate that the yellow stragglers exist in binary systems and enhancements of s-process elements in yellow stragglers can indicate Roche Lobe overflow mass transfer from a once asymptotic giant branch star which has since evolved into a white dwarf.

This dissertation details the radial velocity survey and the chemical abundance analysis that have been conducted to investigate the yellow stragglers with regard to this hypothesis. The radial velocity survey revealed that eight of the ten yellow stragglers studied exhibit variable radial velocities indicating that the yellow straggler population of M67 possess a high binary frequency. However, the chemical abundance analysis revealed that none of the yellow stragglers exhibited enhancements of the s-process elements Y and Ba. Therefore, a history which involves Roche Lobe overflow mass transfer cannot be confirmed for the yellow straggler stars.

Acknowledgments

First and foremost, I would like to thank Dr. Jeremy R. King for his patience, guidance and humor, without which, this project could not have been completed. Through his support and endless encouragement he has taught me how to stand on my own as a scientist.

I would also like to express sincere thanks to Constantine Deliyannis for his gracious hospitality, advice and assistance with this project.

Thank you to all of my dissertation committee members: Jeremy King, Sean Brittain, Bradley Meyer, Jens Oberheide and Dieter Hartmann. Your willingness to serve, patience and cooperation on matters of timing and scheduling are greatly appreciated.

Lastly, I'd like to express my heartfelt gratitude to my family and friends for their support, their belief in me and their kind words of encouragement over the years.

Table of Contents

List of Tables

List of Figures

Chapter 1

Introduction

Star clusters have provided the means to investigate theories of stellar evolution by providing a set of coeval stars with approximately the same chemical composition but with differing masses. Studying star clusters, as entities in and of themselves, in addition to studying the stars in those clusters has laid the groundwork for much of the current standard theory of stellar evolution. Scientists have successfully theorized and observed how differing stellar mass and chemical composition affect not only the evolution of the stars in the cluster, but also the evolution of the cluster itself. Because clusters form the building blocks of the galaxy, a thorough understanding of the dynamics of star clusters is crucial to our understanding of the dynamics of the galaxy. However, even after a century of studying star clusters, unresolved issues remain. For example, populations of stars exist in the color magnitude diagrams of star clusters whose photometry and associated evolutionary state cannot be explained by current, standard single star evolution theory. One such population is considered in this study: the "yellow stragglers."

It is possible that the yellow stragglers (YSs) occupy their precarious color magnitude diagram locations as a result of being formed by mass transfer in close binary systems. There exist two spectroscopic characteristics that can be indicative of such a mass transfer system. Specifically, variable radial velocities can be used to establish the binary nature of such systems and enhancements of slow neutron capture, or s-process nucleosynthesis elements can reveal a mass transfer history. In this study, information regarding these two characteristics has been sought for the yellow stragglers found in the color magnitude diagram of the old, open cluster M67. The yellow straggler population of M67 exhibits a high binary frequency, however, s-process element enhancements were not observed

for any of the yellow straggler stars. This dissertation will detail the methods employed to study these objects and will discuss some of the implications of the results.

1.1 M67

Three specific characteristics of M67 make it an ideal cluster to study for this particular project. The first is that M67 is an open cluster as opposed to a globular cluster. Open clusters tend to to have fewer members and tend to be less gravitationally bound than globular clusters. Therefore, open clusters are typically subject to less crowding in the field of view making it easier to resolve individual stars, particularly towards the cluster center. The second characteristic that is advantageous in studying M67 is its age. At roughly 4 Gyr, M67 is one of the oldest open clusters observed. Its age is necessary in the current study because the advanced evolutionary states of low mass stars will be need to be considered. For many of these stars, these late evolutionary states are typically not reached for billions of years. The third favorable characteristic of M67 is its spatial location. M67 has galactic coordinates: $l = 215.688°$ and $b = 31.923°$ (Yadav et al., 2008). From an earth-centric point of view, this places M67 not only away from the galactic center but also slightly above the galactic plane. Therefore, M67 has relatively few contaminating field stars in its field of view and is subject to little interstellar reddening. The color excess reported by Taylor (2007) is only $E(B-V) = 0.04$ mag. Furthermore, M67 is located roughly 900 pc (Yadav et al., 2008) away from the earth, allowing many of the stars in M67 to be observed with medium-class, ground based telescopes. This, in turn, makes M67 data more accessible in a long term survey like the one that has been conducted for this study.

1.2 The Color Magnitude Diagrams of Star Clusters

The color magnitude diagrams of star clusters provide an efficient way to identify potential YSs. A color magnitude diagram (CMD) for M67 was used to accomplish this specific task as will be explained in §2, however, this currently warrants a brief review of the information that can be gleaned from a CMD.

Figure 1.1 shows a plot of the CMD for M67, constructed from the available Yadav et al. (2008) photometry for stars that lie in the field of view of the cluster. Stars that reside along the

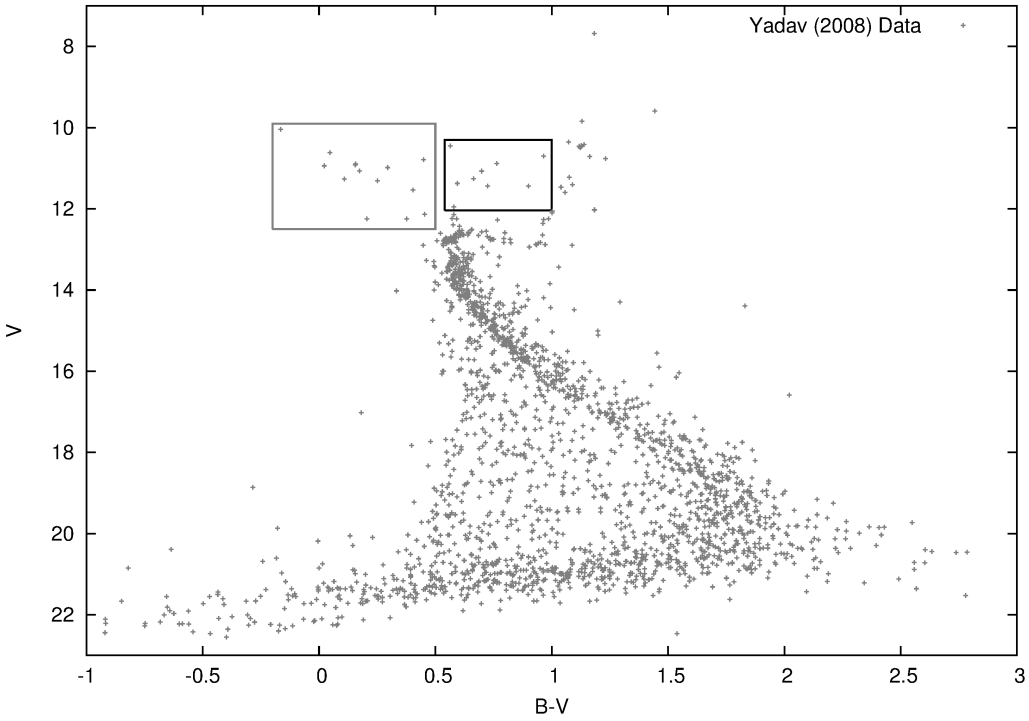

Figure 1.1: The color magnitude diagram (CMD) for M67is presented here using the available photometry for stars in the field of view of M67 from Yadav et al. (2008). Note that this CMD is plotted in terms of the parameters V and B-V. The parameter, V, is the visual magnitude of a star; the value of V decreases toward the top of the plot, however, this corresponds to brighter stars. The parameter, B-V, is referred to as the color index of a star and is, in fact, the difference between the "blue" or B magnitude and the V magnitude of a star. The smaller the value of B-V, the bluer the star. The yellow stragglers (YSs) observed in this study are mostly located within the smaller black box. The blue stragglers observed in this study are mostly contained within the larger gray box.

ridge running from relatively faint and red CMD positions ($B - V \sim 1.0$, $V \sim 16.0$) to relatively bright and blue positions, constitute the cluster's main sequence (MS). The "turnoff" point for the cluster is located at the brighter, bluer end of the MS (roughly at $B - V \sim 0.6$, $V \sim 13.5$). Stars that are located at about the same visual magnitude but are redward of the turnoff constitute the cluster's subgiant branch (SGB) and consequently are referred to as subgiant (SG) stars. The red giant branch (RGB), asymptotic giant branch (AGB) and red clump of the cluster are more difficult to point out because they are sparsely populated compared to the MS and SGB. The stars that trace out a wide band from about $B - V \sim 1.0$, $V \sim 12.5$ to $B - V \sim 1.4$, $V \sim 10.0$ collectively reside in the CMD positions that are associated with these evolved states.

The photometry of the stars that reside in the CMD regions described above can be understood and predicted by stellar atmosphere models in the context of standard single star evolution theory. For example, Prialnik (2000) points out in her book on stellar structure and evolution that the photometry of a MS star and the length of the star's MS lifetime can be predicted primarily by the star's mass. The ability to predict these characteristics lies in the assumption that MS stars exist in both hydrostatic equilibrium and thermal equilibrium.

The assumption that a MS star exists in hydrostatic equilibrium requires that the star experiences an outward pressure that is balanced by the gravitational force inward. More massive MS stars will experience greater gravitational forces than less massive stars and will therefore have to experience greater outward pressures in order to exist in hydrostatic equilibrium. To achieve a greater outward pressure requires that a more massive star must attain a higher temperature than a less massive star. A higher temperature results in two photometric effects: a higher luminosity and a bluer color. These characteristics result because stars radiate approximately like blackbodies. Wein's law states that the peak wavelength in which a star emits light is inversely proportional to its temperature:

$$\lambda_{\text{peak}} = \frac{\text{b}}{\text{T}} \tag{1.1}$$

where b is Wein's displacement constant. The Stefan-Boltzmann law can be used to show that the luminosity of the star is directly proportional to its effective temperature:

$$\text{L} = 4\pi\text{R}^2\sigma\text{T}_{\text{eff}}^4 \tag{1.2}$$

where R is the radius of the star and σ is the Stefan-Boltzmann constant. These relationships show that higher temperatures will result not only in greater luminosities, but also shorter peak wavelengths, or bluer colors, for more massive stars. These more massive MS stars are therefore found on the brighter, bluer end of the MS.

The assumption that a MS star exists in thermal equilibrium requires that the star generates energy at the same rate that it radiates that energy away. Ultimately, this assumption allows the star's mass to dictate the amount of time it will spend burning hydrogen on the MS. The amount of time a star spends burning hydrogen on the MS can simply be thought of as the amount of nuclear fuel available for burning, divided by the rate at which the star consumes the available fuel (hydrogen in this case). The fuel available for burning will be proportional to the star's mass and the rate of

fuel consumption equals the rate of energy generation. The assumption of thermal equilibrium for a MS star requires that the rate of energy generation equal the rate that the energy is radiated away, i.e. the luminosity. Therefore, the amount of time a star spends burning hydrogen on the MS can then be expressed in a way that relates the MS lifetime to both the mass and the luminosity of the star:

$$\tau_{\rm MS} \propto \frac{\rm M}{\rm L} \tag{1.3}$$

However, both empirical information as well as manipulations of the stellar structure equations indicate that along the MS, the luminosity of the stars is proportional to the mass cubed. Therefore, the time spent burning hydrogen on the MS is inversely proportional to a star's mass squared:

$$\tau_{\rm MS} \propto \frac{1}{\rm M^2} \tag{1.4}$$

It can now be seen that more massive stars will reach the end of their MS lifetimes, or "turn off," and will evolve away from locations associated with the MS in the CMD before stars with lower masses. Because the more massive stars are found at the bluer, brighter end of the MS, this indicates that as the cluster ages, the number of massive stars that have turned off of the MS will increase and the location of the turnoff point will recede to fainter and redder positions on the CMD.

The SGB, RGB, and AGB phases of evolution are also well understood. Our ability to model these various evolutionary states can be tested by using a procedure known as isochrone fitting. The general idea behind generating an isochrone is to model the evolution of single stars of varying masses that have all been subjected to the same set of cluster parameters. For example, the isochrone that has been fit to the stars in M67 for the current project (see Figure 1.2) is indicated by the solid line. This isochrone has been derived from the theoretical photometry of stars of various masses that each have an initial metallicity value of [M/H] = 0.12 dex, have each been subjected to an interstellar reddening value of $\rm E(B-V) = 0.01$ and a distance modulus of $\rm (m-M)_o = 9.75$ and have been allowed to evolve to an age of 3.6 Gyrs. It can be seen from this figure, that the resulting photometry of single star evolution models as indicated by the 3.6 Gyr isochrone, is capable of mimicking the observed photometry of the cluster stars.

In addition to the populations of stars in the CMD of M67 that are well understood and predicted by single star evolution theory, there are other populations of stars whose photometry is not sufficiently explained. There are two such populations that will be referred to in this introduction:

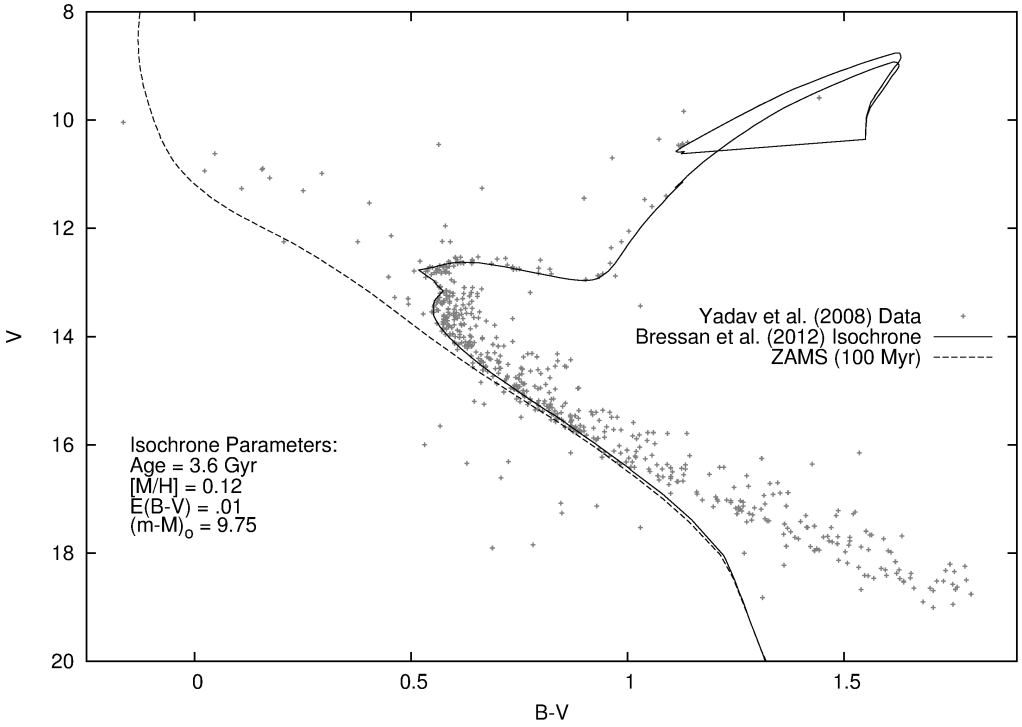

Figure 1.2: The CMD plotted here includes only the photometry for stars in the Yadav et al. (2008) study that have membership probabilities $> 60\%$. The solid line in this plot represents a PARSEC isochrone[1](Bressan et al., 2012) generated for M67 using the values listed in the plot for the parameters: age, metallicity ([M/H]), reddening (E(B-V)) and distance modulus ($(m - M)_o$). The dashed line indicates a zero age main sequence (ZAMS) for M67; the ZAMS is estimated by a 100 Myr PARSEC isochrone with the same [M/H], E(B-V) and $(m - M)_o$ values that were used to generate the 3.6 Gyr isochrone.

the yellow straggler stars (YSs) and the blue straggler stars (BSs). The BSs are stars that are both bluer and brighter than the turnoff for the cluster and are sometimes referred to as an extension of the cluster's MS. The majority of the BSs in M67 can be found encompassed by the larger gray box in Figure 1.1. The YSs are stars that are brighter than the cluster turnoff and have colors that are intermediate between that of the turnoff and the RGB. The majority of the M67 YSs can be found in the smaller black box in the Figure 1.1. The observed photometry of the stars in both of these populations cannot be explained using the current standard theory. The following sections will identify and discuss the details of some of the complications that arise in attempting to explain the photometry of both the blue and yellow straggler stars.

[1]http://stev.oapd.inaf.it/

1.3 Review of the Yellow Stragglers

The stars that comprise the anomalous stellar population that will be focused on in the current study are often referred to as the "yellow straggler stars" (YSs). The population of M67 YSs that were studied for the present work can be seen in Figure 1.3 with their associated photometric uncertainties (Yadav et al., 2008) and their identification numbers assigned presently. Note that Table 2.1 cross references the identification numbers from different studies for convenience. Currently, there is no understood evolutionary state that would be associated with the photometry exhibited by the YSs, however, similar YS populations have been identified in both open and globular clusters (Eggen & Sandage, 1964; Kinman, 1965; van den Bergh et al., 1980; Hesser et al., 1984; Janes & Smith, 1984; Ferraro et al., 1991, 1992; Clark et al., 2004). The existence of YSs in multiple clusters indicates that they are real population. Subsequently, some of the studies listed have briefly investigated potential reasons that YSs possess anomalous photometry.

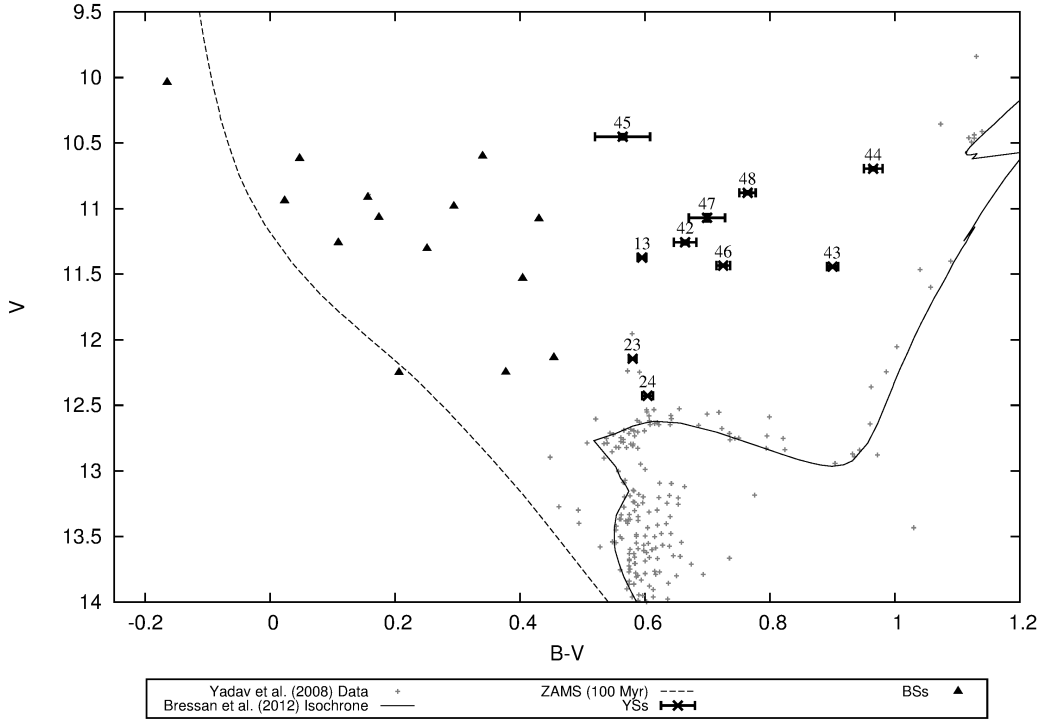

Figure 1.3: The M67 YSs are plotted in this CMD with their associated photometric uncertainties and the identification numbers assigned in the current work. The M67 BSs are plotted with filled triangles for reference. Note the 100 Myr, or ZAMS, and 3.6 Gyr isochrones have also been included for reference.

The terminology "yellow stragglers" follows that presented by Hesser et al. (1984) and Ferraro et al. (1991, 1992). However, some authors refer to these objects as "red stragglers" (Janes & Smith, 1984) and some use the term "blue subgiants" (Kinman, 1965). The lack of a consensus on something as simple as a name for these objects is likely a result of the fact that there is currently no consensus on what type of objects the yellow stragglers (YSs) actually are. van den Bergh et al. (1980) recognized a YS population in the dying globular cluster E3, but referred to them as BSs, however, Hesser et al. (1984) point out that the BSs referred to by van den Bergh et al. (1980) actually posses intermediate colors and are not a simple extension of the cluster's MS. Hesser et al. (1984) went on to say that "there is no simple or entirely convincing explanation" of the positions of these stars in the cluster's CMD. They subsequently offer three potential explanations: 1) the YSs exist in binaries 2) an "unusual state of stellar evolution" has allowed the YSs to evolve as single stars from the MS to their current CMD locations or 3) an alternative "unusual state of stellar evolution" has allowed the YSs to evolve as single stars from the giant branch to their current CMD locations. Ferraro et al. (1991, 1992) suggest that based on the colors, magnitudes and central spatial locations of these objects in at least some clusters, these objects could be the result of "spurious blends" of two stars, implying that these objects could simply be optical binaries. Janes & Smith (1984) target two M67 YSs in particular, arguing that they can both be explained as spectroscopic binaries and they state that previous radial velocity data from Mathieu et al. (1986) support this hypothesis. Perhaps more interestingly, Landsman et al. (1997) report that that one of the YSs involved in the Janes & Smith (1984) study has a confirmed white dwarf (WD) companion and state that it seems likely that the system has experienced an episode of mass transfer in its history. Furthermore, Landsman et al. (1997) state that this YSs photometry may be the result of the evolution of a BS. Clearly, the picture painted for the YSs is a complicated one with no clear hypothesis that is capable of explaining the existence of all YSs. The discussions in the following sub-sections will address some of the issues that arise when considering potential explanations of YSs.

1.3.1 Contaminating Field Stars

One potential explanation for the anomalous photometry of YSs is that these stars are not true cluster members, but are simply contaminating field stars along the line of site of the cluster in question. If the YSs are not true cluster members, then they could exhibit photometry that does not agree with the photometry that is predicted for the true members of the cluster. However,

while field star contamination may be able to explain the existence of some of the YSs, Hesser et al. (1984) and Ferraro et al. (1991) determined that there are statistically significant populations of YSs in the globular clusters E3 and NGC 6171 respectively, that cannot be explained in this way. Furthermore, four of the ten YS candidates considered for the current study have proper motion membership probabilities $> 80\%$ according to Yadav et al. (2008) (see Table 2.1). In these studies where the membership of the YSs has been questioned, each determined that at least some of the stars that possess YS locations in the CMD are likely true cluster members.

1.3.2 Photometric Blends of "Normal" Stars

Another possible explanation for the photometry of YSs is that the observed photometry is the result of the combined photometry of two "normal" cluster members in either an optical blend or a binary system. In their work studying the giant branch of M67, Janes & Smith (1984) refer to two stars considered in the present study (YS 43 and YS 44, see Figure 1.4) as "red stragglers" and state that they are most easily explained as binaries. This study was based on the photometry of Eggen & Sandage (1964), Racine (1971) and the previously unpublished photometry of Janes. For each star, they used a near turnoff star as one component and derived that the second component must be located on the lower giant branch in order to achieve a composite magnitude and color that matches that of the observed YS in question. Janes & Smith (1984) were successful in achieving the observed photometry of both stars using this method and support this finding with the findings of Mathieu (1983), that both YS 43 and YS 44 exhibit variable radial velocities. The variations in the radial velocities of these stars suggest that they exist in binary systems.

The current study uses the newer photometry of Yadav et al. (2008) to consider the hypothesis of Janes & Smith (1984) for YS 43 and YS 44. The binary components were derived from the 3.6 Gyr isochrone (Bressan et al., 2012) that was fit to M67 in an attempt to recreate the observed Yadav et al. (2008) photometry of the YSs. It can be seen in Figure 1.4 that the observed photometry for YS 23 (upper-left panel), YS 24 (upper-right panel) and YS 43 (lower-left panel) is possible to mimic by combining the photometry of two cluster members in well understood evolutionary states. However, mimicking the observed photometry for YS 44 (lower-right panel) is more difficult. In this figure, the composite photometry, which should mimic the observed photometry, is indicated by an open circle. The CMD location of the composite photometry is the result of blending the B-V and V magnitudes of any two theoretical components (filled circles) found either near the TO, along the

SGB or along the RGB. The top two panels of Figure 1.4 show that the observed Yadav et al. (2008) photometry of the YSs 23 and 24 can be achieved by combining two near turnoff stars of similar color. It can be seen in the bottom left panel, that the Yadav et al. (2008) photometry can also be achieved for YS 43 by combining a near turnoff star and a RG, in a similar fashion to Janes & Smith (1984). However, in the case of YS 44, the bluest, near turnoff star has been chosen as one of the components, yet the composite photometry is still located redward of the observed photometry. Using the Yadav et al. (2008) photometry shows that a component bluer than the turnoff for the cluster would be necessary in order to achieve the observed photometry of YS 44.

1.3.3 Photometric Blends Between Normal and Blue Straggler Stars

In addition to YS 44, the remaining YSs that were not addressed in § 1.3.2 are also not satisfactorily explained as photometric blends of two normal stars with well understood and modeled evolutionary states (near TO, SG or RG states). To recreate the observed colors of these remaining YSs using normal cluster stars would require the use of two stars along the SGB of M67, however, combining the photometry of two stars with the same magnitude can only result in an increase of 0.75 mag, which is insufficient to account for the roughly 1.5 mag gap in visual magnitude between the SGB and the faintest of these YSs (YS 46) as can be seen in Figure 1.3.

It was previously mentioned that Ferraro et al. (1991) discovered a population of YSs in the globular cluster, NGC 6171, and concluded that this population could not be explained as a contamination of field stars. They state that the locations of the stars in the cluster CMD would be difficult to explain in the context of standard stellar evolution theory or via photometric errors. Instead, they propose that these stars could simply be optical binaries and claim that the fact that almost the entire population of YSs is contained in the central field of the cluster supports this hypothesis since crowding in the central regions is common. They note that the color-magnitude regime of the YSs requires a blend of either a SG or a RG star with something blue, like a BS. They show that forcing a deblending of the observed YSs, requiring one component to be either a SG or RG, leaves a "nice" BS sequence. A similar situation is observed for the globular cluster, NGC 1904, according to Ferraro et al. (1992). They find a situation where the YSs observed in NGC 1904 cannot be explained by cluster contamination, and by applying the same deblending procedure they find that the YSs in this cluster can also be explained by spurious blends of either SGs or RGs and BSs.

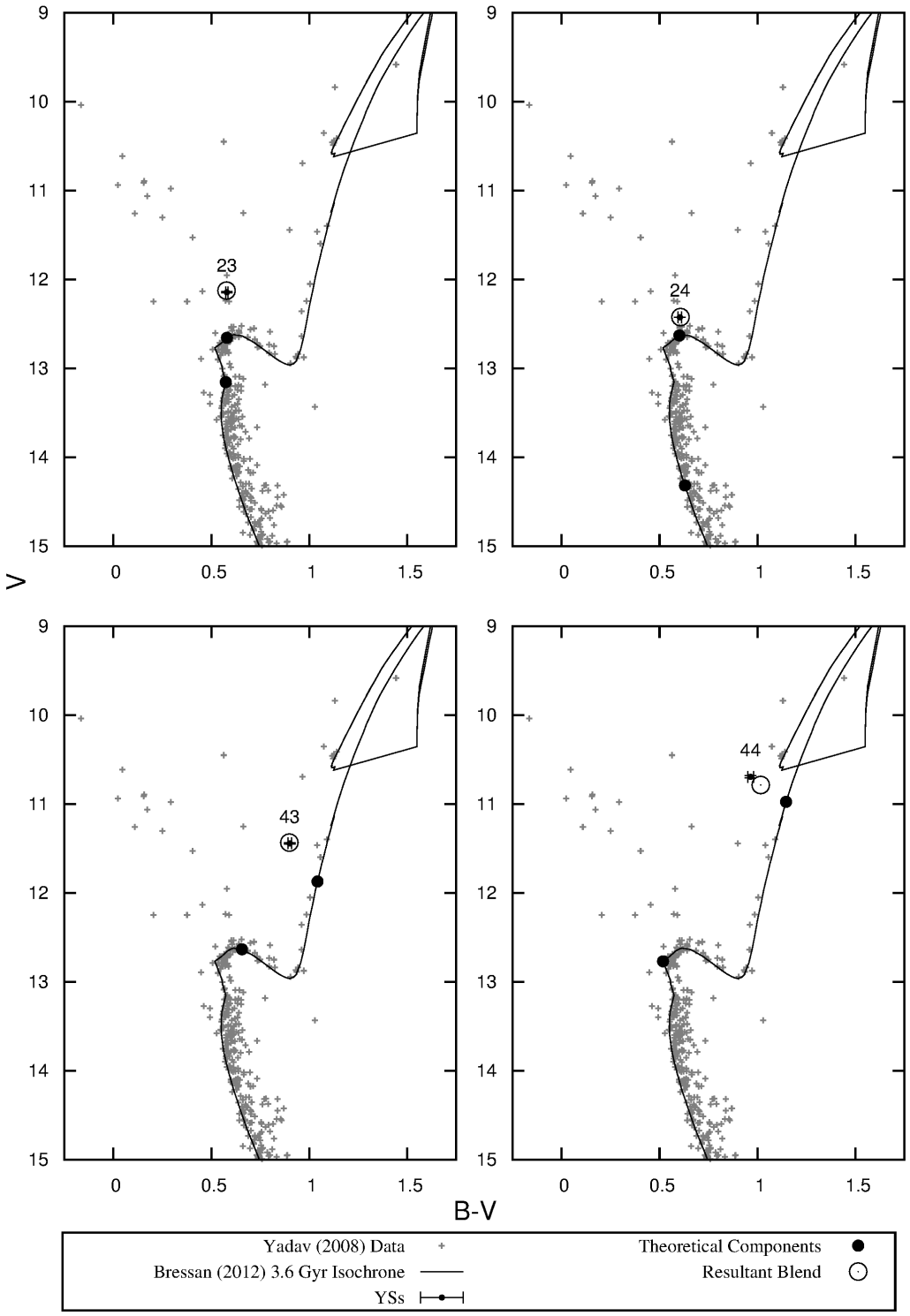

Figure 1.4: The composite photometry (open circles) from combining the photometry of two theoretical "normal" components (filled circles) derived from the 3.6 Gyr isochrone of Bressan et al. (2012). The YS in question is shown with associated uncertainty and labeled with its identification number from the current work.

Similarly, in order to achieve the observed photometry for the M67 YSs barring YS 23, YS 24 and YS 43 (see Figures 1.5 and 1.6) it is necessary for one of the components in the blend to be a BS (see Figure 1.3). In these plots, one component is chosen from the observed M67 BSs while the other component is an appropriate TO, SG or RG derived from the isochrone. In particular, it can be seen in the bottom left panel of Figure 1.5 that using a BS component slightly fainter than BS 3 would achieve the observed photometry of YS 44, whereas using two "normal" stars could not produce this observed photometry as was seen in Figure 1.4. Additionally, the theoretical composite photometry agrees with the observed photometry for the remaining YSs in these plots.

It should be noted however, that issues arise with this explanation as well. Mathieu & Latham (1986) pointed out that for YS 42, the photometry of a BS and a RG in a binary system are sufficient to mimic the observed V and B-V photometry of this star, however, the theoretical composite *uvby* photometry of this system does not agree with the observed *uvby* photometry reported by Nissen et al. (1987) for this star. Therefore, in at least some cases, the observed YS photometry cannot be explained as a photometric binary of a normal star and a BS.

1.3.4 Evolution of BSs

It was previously mentioned that the work of Landsman et al. (1997) reported on a white dwarf (WD) companion for YS 43. More specifically, they reported on an ultraviolet (UV) detection of YS 43 (Stecher et al., 1997), which is considered direct evidence of a WD companion. Landsman et al. (1997) followed up this UV detection with a UV spectroscopic study. The UV spectra were fit with WD models leading to a derived WD mass of $\sim 0.22\,\mathrm{M}_{\odot}$ and a WD temperature of $\sim 16,000\,\mathrm{K}$. Furthermore, this WD mass and the mass function derived by Mathieu et al. (1990) indicate a YS mass of roughly $1.5 M_{\odot}$. Landsman et al. (1997) determined that these masses in conjunction with an orbital period of 42.8 days (Mathieu et al., 1990) indicate that the binary system likely experienced an episode of what is sometimes referred to as Roche Lobe overflow (RLOF) mass transfer in its history. Landsman et al. (1997) also state that the WD should have cooled to its current temperature within 75 Myrs since expelling it envelope on the RGB. Thus, Landsman et al. (1997) ultimately conclude that the observed photometry of YS 43 is likely the result of the evolution of a BS formed by RLOF mass transfer. The current work will further investigate this specific hypothesis as a potential explanation for M67 YSs (see § 1.5 for details). Therefore, to outline a better understanding of this potential relationship between YSs and BSs, a review of the nature of the BSs will follow.

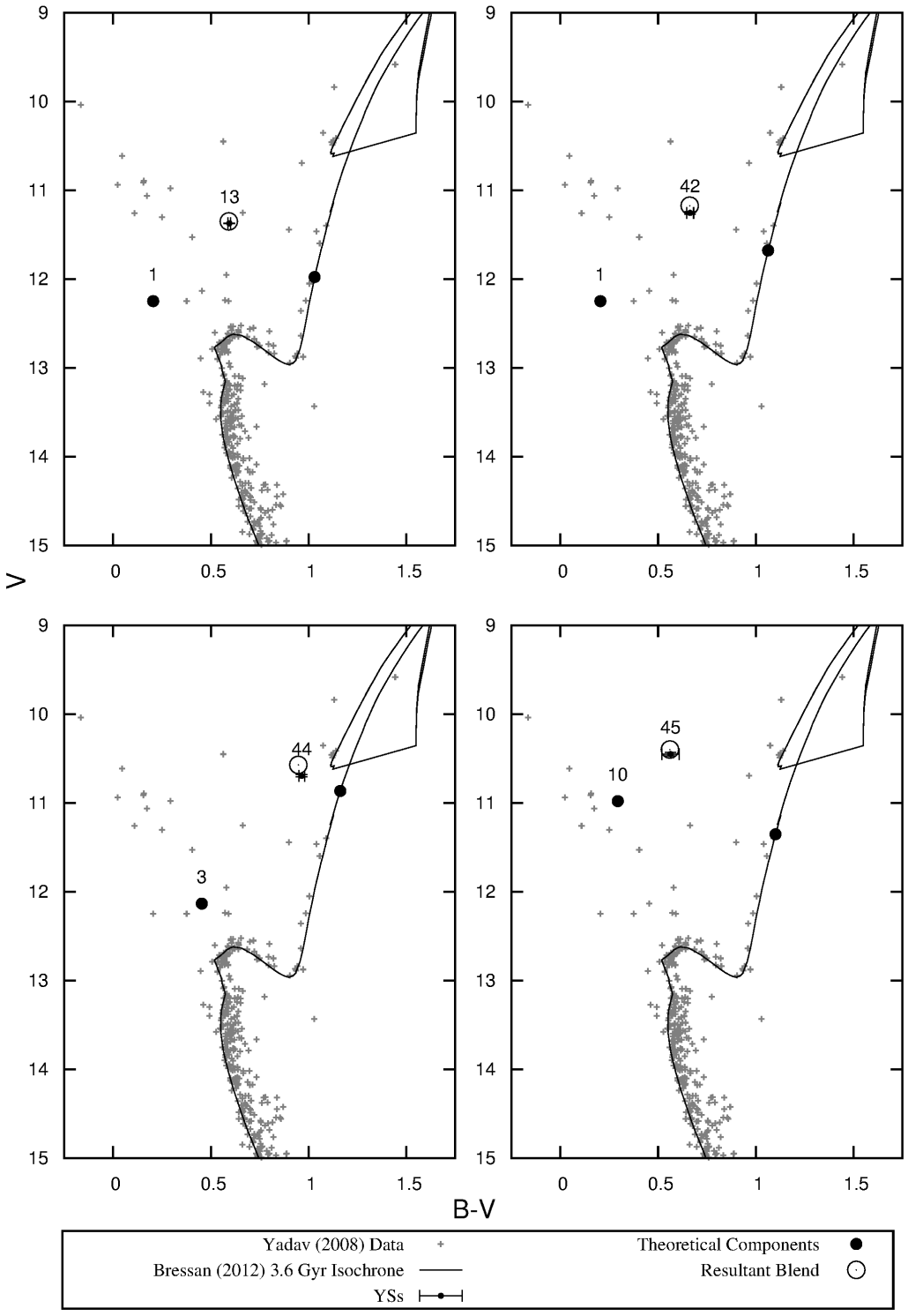

Figure 1.5: The composite photometry (open circles) from combining the photometry of two components (filled circles); one component is chosen from the observed BSs and the other is derived from the 3.6 Gyr isochrone of Bressan et al. (2012). The YS in question is shown with associated uncertainty and labeled with its identification number from the current work.

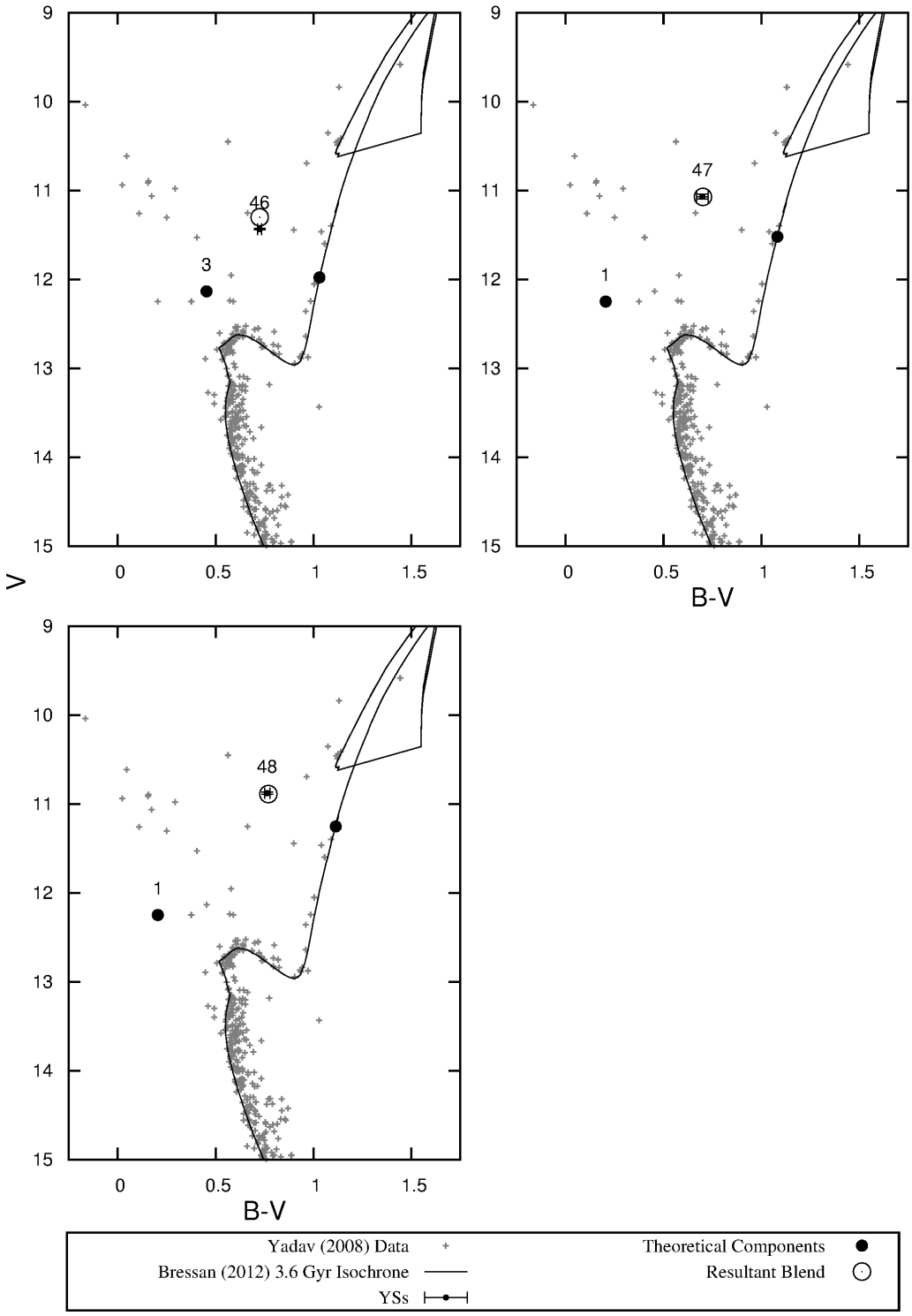

Figure 1.6: The composite photometry (open circles) from combining the photometry of two components (filled circles); one component is chosen from the observed BSs and the other is derived from the 3.6 Gyr isochrone of Bressan et al. (2012). The YS in question is shown with associated uncertainty and labeled with its identification number from the current work.

1.4 Review of the Blue Stragglers

The blue stragglers (BSs) were first identified by Sandage (1953) as the stars that were both brighter and bluer than the turnoff in a color magnitude diagram (CMD) of the globular cluster M3. The population of stars that constitute the BSs in M67 can be seen in Figure 1.1 encompassed by the larger gray box. If these stars are indeed cluster members and if they are hydrogen burning stars (as can be interpreted by their appearance as an extension of the MS of the cluster, see below for further discussion) it can been inferred that these stars are more massive than stars located at the turnoff. Assuming that these stars are a part of the coeval population of the cluster, they should have evolved away from the MS. It was from this reasoning about the peculiar CMD locations of these objects that the name "blue straggler" was derived; they appear to have colors that are bluer than any "normal" MS star in the cluster, and they appear to "straggle" behind other cluster members with similar masses in terms of stellar evolution. Since their discovery, BSs have been identified in the field, open clusters, additional globular clusters and in dwarf galaxies (Stryker, 1993), however, this discussion will focus mainly on the BSs found in open star clusters.

Typically, for a star cluster in which BSs are present, the CMD locations of the BSs are bound on the blue side by the cluster's zero age main sequence, or ZAMS, (see Figure 1.3) estimated by the 100 Myr isochrone that has been fit to M67 in the current work. As can be seen, the BSs tend to follow along the ZAMS with scatter that is roughly similar to that seen along the current MS. This has led to the general hypothesis that these stars experience elongated main sequence, or hydrogen burning, lifetimes due to some rejuvenation mechanism. Complications arise not only from the idea that a single mechanism is not likely responsible for all BSs in all populations, but also from the idea that a single mechanism is not likely responsible for all BSs in any given population. As previously mentioned, the focus of this discussion will be the BSs found in open clusters, which are themselves, thought to be form via multiple formation channels.

1.4.1 Potential Formation Channels

Currently, two formation channels are thought to be responsible for the majority of the BSs in open clusters, and both mechanisms involve interactions between stars that allow the mass of a main sequence (MS) star to be increased. As discussed in §1.2 increasing the mass of a MS star near the turnoff could allow that star to occupy a new position along an extension of the MS past the

turnoff point. The first formation channel relies on direct stellar collisions of main sequence (MS) stars (Hills & Day, 1976). Direct stellar collisions can involve interactions between two single stars, a single star and a primordial binary system, or two primordial binary systems. A single-single stellar collision can result in a fully merged single star with increased mass. A single-binary or binary-binary collision can result in the merger of the components of a primordial binary and can ultimately result in a binary system with an eccentric orbit. The second formation channel relies on what is often referred to as Roche Lobe overflow (RLOF) mass transfer in a close binary system (McCrea, 1964). In this scenario, the more massive primary component in the binary system evolves to a giant stage of evolution while the secondary component is still in a MS stage of evolution. If the primary fills its Roche Lobe, the primary's stellar material can flow through the inner Lagrange point and onto the secondary, thus increasing the mass of the secondary and polluting its atmosphere in the process. The mass of the MS secondary is thus increased allowing it to potentially occupy a BS position on the CMD. Eventually, the primary evolves to its final white dwarf (WD) stage of evolution, and the result is a BS-WD binary system with a circular orbit.

Much work has been dedicated to identifying different types of BSs and attempting to determine the formation channel for each type, however, complications still remain. Hurley et al. (2005) were able to reproduce the raw number of BSs found in M67 through extensive N-body simulations, incorporating both formation channels, but Geller et al. (2013) point out that Hurley's simulation produces too many short period BSs and that the orbital parameters and hard binary frequency of the simulated BSs did not match the observed populations of either M67 or another old, open cluster, NGC 188. The populations of BSs in M67 and NGC 188, however, are not entirely similar. The BS population of M67 is found to be spatially concentrated toward the center of the cluster (Mathieu & Latham, 1986) with no dominant formation mechanism (Leonard, 1996), whereas the BS population in NGC 188 exhibits a bimodal spatial distribution (Geller et al., 2008; Geller & Mathieu, 2012) and the individual BSs are thought to be produced predominantly by the RLOF mass transfer formation mechanism (Geller & Mathieu, 2011). Ferraro et al. (1997, 2004) and Mapelli et al. (2004) each suggest that the similar bimodal spatial distributions of BSs found in globular clusters are likely due to different formation mechanisms operating in different regions of the cluster, i.e., BSs that are spatially located closer to the cluster core where stellar densities are typically higher are more likely to be formed by collisions and mergers, and BSs located in the outer regions of the cluster are more likely to be formed by (RLOF) mass transfer. However, Geller & Mathieu

(2011) found that the majority of the BSs in NGC 188 have parameters that are consistent with the RLOF mass transfer scenario. Furthermore, Geller & Mathieu (2012) determined that there is no significant difference in the orbital parameters associated with the cluster core and halo populations of BSs in NGC 188, and conclude that there is no significant difference between these populations. Geller & Mathieu (2012) further conclude that the bimodal distribution is due to dynamical friction in the cluster which results in mass segregation.

Geller et al. (2013) report on their N-body simulations of NGC 188, stating that these simulations were successful at recreating the distributions of orbital periods, eccentricities, companion masses and mass ratios of the observed BSs. Additionally, they found that the majority of the BSs in the simulation formed via RLOF mass transfer, in agreement with the Geller & Mathieu (2011) finding that the majority of the BSs in NGC 188 likely formed through a mass transfer scenario. However, Geller et al. (2013) found that their N-body simulations of NGC 188 underproduced BSs and simultaneously overproduced MS-WD binary systems. The MS-WD binary systems can arise from common envelope evolution in a binary system. Geller et al. (2013) conclude that this discrepancy between the simulation populations and the observed population arises from incorrectly imposing mass transfer on the progenitors of the MS-WD binaries. Specifically, they suspect that the computation of the critical mass ratio, q_c, is determined incorrectly due to simplifying assumptions. The critical mass ratio determines whether or not a binary system undergoes common envelope evolution in the N-body simulations, and that ratio is determined for these models assuming completely conservative mass transfer, an unlikely scenario according to Woods et al. (2012), especially during the early stages of mass transfer when mass loss rates of the giant star are high. Geller et al. (2013) propose that more accurate determinations of this critical mass have the potential to adjust the number of BS-WD and MS-WD binaries that are produced and could possibly account for the observed discrepancy.

1.4.2 Mass Transfer and Stellar Evolution

It is clear from the previous discussion that there is still much work to be done to fully understand the complete story behind the BSs. However, what cannot be ignored from the previous discussion is that RLOF mass transfer is a plausibly dominant formation channel for BSs. Furthermore, in § 1.3.4 it was shown that at least one of the YSs in the current study is believed to be the

result of the evolution of such a mass transfer BS. Therefore, the current sub-section relies on the work of Tian et al. (2006) to consider mass transfer binary evolution.

To investigate how BSs might evolve, Tian et al. (2006) investigated the stellar evolution of mass transfer binary systems. To conduct this study they considered a close binary system subject to stable RLOF. First, evolution of the donor was carried out and mass transfer rates were computed for various ages of the star. These mass transfer rates were then used to adjust the mass of the accretor in such a way so that the evolution of both components in the binary was synchronized. To generate an evolutionary track for the binary system in a CMD, Tian et al. (2006) synthesized the total light of the binary system. Ultimately, it was determined that after mass transfer terminates, the binary system will evolve toward the BS region of the CMD and will spend enough time there ($\sim 1.2\,$Gyrs) to be observed as a BS, until the accretor evolves away from the MS. Sills et al. (2009) later noted that even though Tian et al. (2006) do not compare their stellar evolutionary track for a BS formed by RLOF to that of a normal star, the evolutionary track appears "quite normal after mass transfer ceases." Sills et al. (2009) remarked that both their work on collisional BSs and the work of Tian et al. (2006) on mass transfer BSs indicate that "post-main sequence evolution...is quite robust to disturbances early on the main sequence."

To consider the evolutionary tracks of single stars in M67, Figure 1.7 shows the BaSTI[2] stellar evolution tracks (Pietrinferni et al., 2004) plotted on top of the Yadav et al. (2008) photometry for the likely members of M67. McCrea (1964) determined that the upper limit for the mass of a BS formed via RLOF mass transfer would be roughly two times the mass of the turnoff for the cluster. In this study, the turnoff mass was determined from the 3.6 Gyr PARSEC[3] isochrone (Bressan et al., 2012) to be $\sim 1.3\,M_{\odot}$. Thus, evolutionary tracks for stars with masses from $1.3 - 2.6\,M_{\odot}$ were generated. If it is assumed that the YSs are the progeny of the BSs and that they were formed via RLOF mass transfer, information on their masses can be gleaned from such a diagram. Making this assumption, it can be seen in Figure 1.7 that the locations of the YSs do not disagree with the upper mass limit of the cluster's BSs ($\sim 2.6\,M_{\odot}$) according McCrea (1964). This finding that the YSs of M67 do not disagree with the M67 BS upper mass limit is encouraging when considering a mass transfer origin for YSs, however, it is far from evidence. The following section will describe the evidence that has been sought in this investigation of a mass transfer origin for YSs.

[2]http://albione.oa-teramo.inaf.it/
[3]http://stev.oapd.inaf.it/

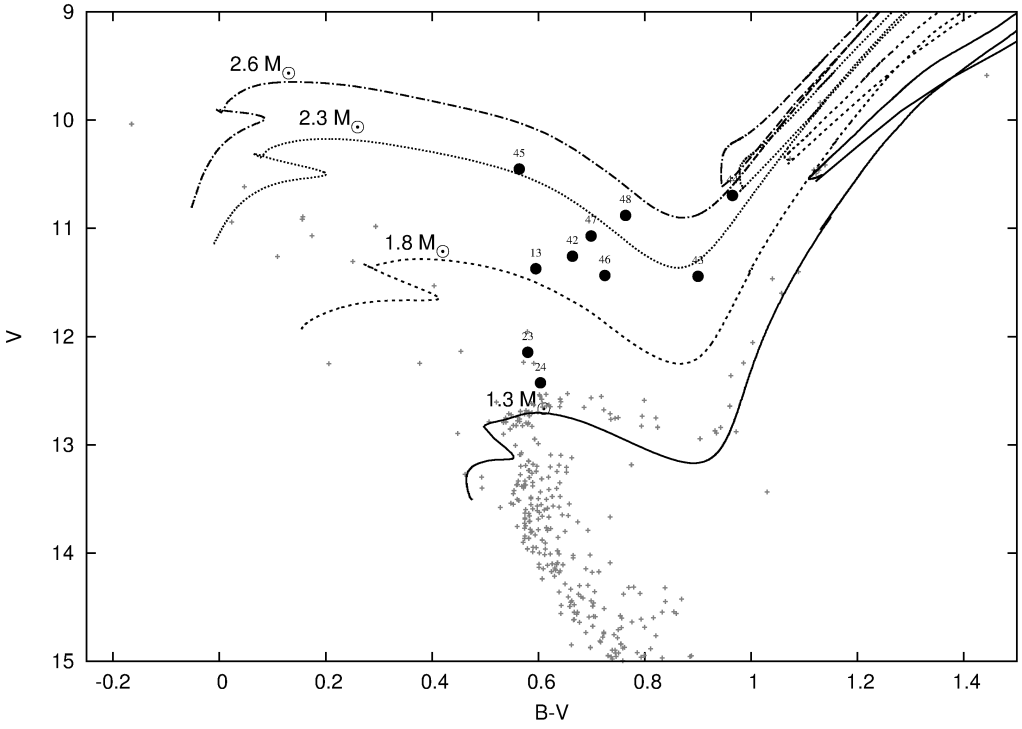

Figure 1.7: This plot shows the evolutionary tracks of stars more massive than the turnoff for M67. The turnoff mass of M67 was determined in this study to be $\sim 1.3\,M_{\odot}$. According to McCrea (1964), the upper limit of the mass of a BS is roughly twice the turnoff mass, therefore evolutionary tracks were produced for stars up to $2.6\,M_{\odot}$ for this plot. The observed YSs are marked with filled circles and their identification numbers from the current study.

1.5 The Current Study

In particular, the present work aims to investigate the hypothesis that the YSs in M67 could be the result of the evolution of RLOF mass transfer BSs by considering the radial velocities and the chemical abundances of the potential members of this previously described anomalous stellar population. The previous sections have established that one of the predominant formation mechanisms for BSs, and therefore, potentially YSs, is RLOF mass transfer; this process was briefly described but deserves a more detailed review here to justify the evidence that has been sought to investigate mass transfer as a formation mechanism for YSs in the current study.

RLOF mass transfer happens in a close binary system where one of the stars, the primary, or donor star, is more massive than the secondary, or accretor. The donor will evolve more quickly than the accretor due to its larger mass. It will likely go through its red giant stage and asymptotic giant stage while the accretor remains on the MS. If the donor star fills its Roche Lobe when it becomes a giant, the accretor can gain material from the donor through the binary system's inner Lagrange point and become "polluted" by donor material. Subsequently, the donor star will continue to evolve, eventually becoming a WD, leaving the accretor to be detected. The accretor in this scenario can be expected to exhibit two specific characteristics.

The first, perhaps obvious, characteristic is that the accretor will exhibit a variable radial velocity as long as the binary system possesses a non-zero inclination angle. The donor star remnant, now a WD companion, will likely be undetectable in the optical range of the electromagnetic spectrum due primarily to its size, however, such companions may be observed in the ultraviolet (UV) range like in the case of YS 43 (Landsman et al., 1997). These UV detections can be difficult to obtain, however, since they require the use of space based telescopes. Furthermore, Landsman et al. (1997) reported that the WD companion of YS 43 was the faintest WD detected. Therefore, the detection of variable radial velocities can provide a useful substitute for UV detections.

The second characteristic that can potentially be expected in mass transfer progeny, is an overabundance of slow neutron capture (s-process) elements in the spectrum of the accretor. Though there are likely additional cites for s-process nucleosynthesis, it is believed that asymptotic giant branch (AGB) stars are the primary site for s-processing (see review by Meyer (1994)). Therefore, if the accreting star has been polluted with material from an AGB companion, it may show such s-process element enhancements in its spectrum–a feat that theoretically cannot be accomplished by

a star that has not experienced mass transfer and has not yet reached its AGB phase of evolution. s-process element enhancements have been detected in the spectra of stars that are expected to have experienced RLOF mass transfer and are reported in the literature. For example, the enhancement of the s-process elements Sr and Ba are seen in the so-called Ba giants and Ba dwarfs (McClure, 1983; North & Lanz, 1991). These stars are found to be metal poor (North et al., 1994) and are expected to have formed via RLOF mass transfer. Gray et al. (2011) supports this hypothesis with reports on far ultraviolet excesses detected for Ba dwarfs, indicating that these stars do indeed possess WD companions. A second, potentially more closely related example, is that of the blue metal poor stars studied by Sneden et al. (2003) and Preston & Sneden (2004). Enhancements of the s-process elements Ba and Pb, in addition to C enhancements, were found in the BMPs that existed in binaries. These stars are also believed to have experienced an episode of RLOF mass transfer from an AGB donor and Sneden et al. (2003) conclude that the BMP binaries are in fact true field BSs.

The observations of the M67 targets span the course of about 200 days (see §3 for further details). The time frame of the observations makes it possible to determine whether or not the radial velocity of a target is variable, though the data obtained do not provide enough information to determine an orbital period or other orbital parameters. If a YS target exhibits a variable radial velocity, it suggests that the target exists in a binary system, even if the companion star is not detectable. The radial velocities therefore, could be useful in either debunking or supporting RLOF mass transfer as the formation mechanism responsible for individual members of the YS population in M67.

Additionally, the observations of the the M67 targets were taken at ten different wavelength ranges, allowing coverage of much of the electromagnetic spectrum between 4000 and 9000 Å. This amount of wavelength coverage enables abundance determinations of a variety of elements so that the overall chemical makeup of these stars can be considered in addition to determining s-process element abundances. The s-process element abundances of these anomalous stars could potentially provide additional support either in favor of, or against a RLOF mass transfer hypothesis on an star-by-star basis.

Finally, it is noted that previous work on BSs has shown that: 1) they tend to be found in binary systems and thus exhibit variable radial velocities and 2) they are subject to dynamical cluster interactions that result in mass segregation. These findings indicate that BSs can potentially

be subject to peculiar radial velocities or proper motions due to dynamical effects. Because it is possible that the the YSs may be the progeny of evolved mass transfer BSs, the YSs may also be subject to peculiar motions. Therefore, it is important to investigate all of the stars that reside in YS locations on the CMD of M67, regardless of previous radial velocity or proper motion membership determinations. Because the number of stars that reside in YS CMD positions in M67 is already small (~ 13), it is not a difficult task to study all possible YS candidates regardless of prior cluster membership and/or radial velocity determinations. The current work accomplishes exactly this task.

Chapter 2

Target Selection

To select targets of observation for this study, a color-magnitude diagram (CMD) was plotted for the stars in M67 using Montgomery et al. (1993) photometry. Targets were then selected according to their locations in the CMD. A variety of targets were selected for observation including those that reside in both "anomalous" and "normal" locations on the CMD, however, target selections were restricted to stars in M67 that are brighter than 13th magnitude due to the limitations of the observing instrumentation described in §3. A total of 57 targets were selected and classified into six groups: 1) targets that were located in the region of the turnoff for the cluster are termed turnoff stars (TOs) 2) targets located at positions slightly blueward of the turnoff are termed "anomalous turnoff stars" (ATOs) 3) targets that are both brighter and bluer than the turnoff, appearing to create an extension of the main sequence are termed blue stragglers (BSs) 4) targets located along the subgiant branch are termed subgiants (SGs) 5) targets located along the red giant branch are termed red giants (RGs) and 6) targets that are brighter than the turnoff with colors intermediate between that of the turnoff and the red giant branch are termed "yellow stragglers" (YSs).

It was noted in §1.5 that cluster membership studies are potentially uninformative in the cases of the BSs and the YSs, however, the membership probabilities of "normal" MS, TO, SG and RG stars are likely more reliable and can help to establish the true structure of the CMD of the cluster. The Montgomery et al. (1993) photometry, often used in the literature, has no accompanying cluster membership probability data. Therefore, to produce a CMD for M67 in which only likely cluster members are presented, an attempt was made to use an independent cluster membership probability study for M67 performed by Balaguer-Núñez et al. (2007). However, in order to cross

identify each of the nearly 2000 stars between the two studies requires cross identifying each star's right ascension (RA), declination (DEC) and magnitude values. This process is both time consuming and potentially prone to error due to 1) the fact that the that the RA and DEC values are not identical across studies since they are reported for a different epoch for each study and 2) the fact that the magnitudes are not identical across studies due to inherent photometric calibration uncertainties. In the end, a study completed by Yadav et al. (2008) as part of the WIYN Open Cluster Survey (WOCS) was employed instead. The Yadav et al. (2008) study simultaneously presented photometry and membership probabilities determined via proper motions for stars in the field of view of M67. A CMD was created from the Yadav et al. (2008) target list using only stars with membership probabilities $> 60\%$ (see Figure 1.2). The use of the Yadav et al. (2008) photometry created the much more manageable task of only having to cross identify 57 of the current study's targets of observation between the Yadav et al. (2008) and Montgomery et al. (1993) studies. The photometry for the 57 targets was fairly consistent between the two studies.

Each target of observation was selected solely by its Montgomery et al. (1993) photometry and thus location in the CMD. Therefore, some of the targets have low membership probabilities according to Yadav et al. (2008). The membership probabilities for each star and the photometry from both Montgomery et al. (1993) and Yadav et al. (2008) are summarized in Table 2.1. The columns included in this table contain the following in order from left to right: stellar identifications from the current study (McGahee); identification numbers from Sanders (1977) (S77); identification numbers, visual (V) photometry, mean errors in V, color index (B-V) photometry and mean errors in B-V from Montgomery et al. (1993) (MMJ); identification numbers, V photometry, RMS uncertainties in V, B photometry, RMS uncertainties in B, B-V photometry (calculated in the present work), propagated B-V uncertainties (calculated in the present work) and membership probabilities from Yadav et al. (2008) (Y08).

Figure 2.1 shows the CMD locations of each of the 57 targets of observation. The different classification groups are indicated by the symbols in the legend. Figures 1, 2 and 3 in Appendix A are zoomed in on different regions of the plot found in Figure 2.1 for further reference. Most of the targets are plotted according to their Yadav et al. (2008) photometry, however, in a few cases the target could not be cross identified between the Yadav et al. (2008) and Montgomery et al. (1993) studies. In such cases, the target has been plotted according to its Montgomery et al. (1993) photometry. In Figures 1, 2 and 3 each target has been plotted with its corresponding identification

number from the present study. The targets that have identification numbers enclosed in parentheses are targets that are plotted according to their Montgomery et al. (1993) photometry. These same targets lack the Yadav et al. (2008) membership probability data.

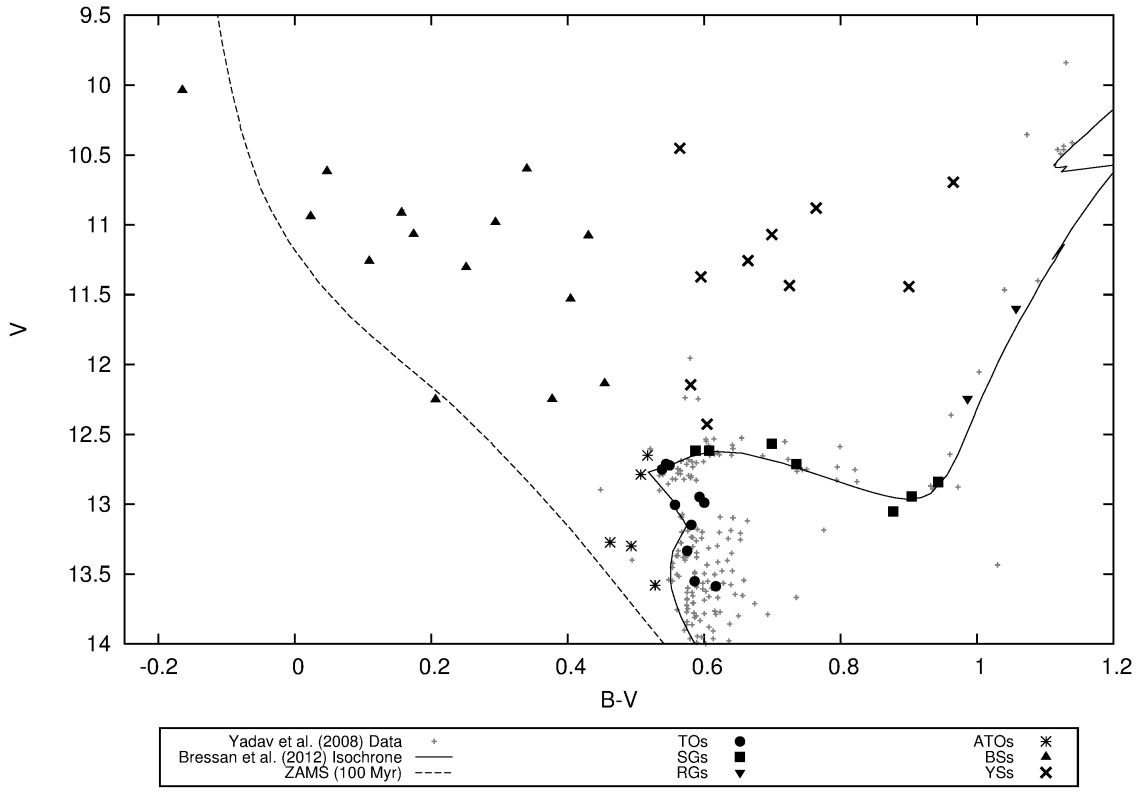

Figure 2.1: The CMD positions of all 57 targets of observation are shown in this plot. The six categories that the targets were grouped into are indicated in the legend. See Figures 1, 2 and 3 for more detail. The ZAMS and 3.6 Gyr isochrone from Figure 1.2 have been included here for reference.

Table 2.1: Photometry Data

McGahee	**S77**	**MMJ**					**Y08**							
Star	ID	ID	V (mag)	$e_{(V)}$ (mag)	B-V (mag)	$e_{(B-V)}$ (mag)	ID	V (mag)	$e_{(V)}$ (mag)	B (mag)	$e_{(B)}$ (mag)	B-V (mag)	$e_{(B-V)}$ (mag)	Membership Probability (%)
BS 1	1280	5940	12.257	0.016	0.260	0.024	1377	12.250	0.008	12.456	0.002	0.206	0.008	98
BS 2	977	6481	10.030		-0.073		813	10.037	0.013	9.872	0.011	-0.165	0.017	98
BS 3	997	5667	12.126	0.005	0.458	0.009	997	12.136	0.002	12.590	0.003	0.454	0.004	97
BS 4	968	6479	11.280		0.130		693	11.260	0.013	11.369	0.029	0.109	0.032	97
BS 5	1434	6510	10.700		0.110		714	10.617	0.018	10.664	0.005	0.047	0.019	97
BS 6		6006	12.278		0.385		148	12.248	0.029	12.625	0.000	0.377	0.029	96
BS 7	752	6476	11.320		0.295		779	11.305	0.013	11.556	0.006	0.251	0.014	96
BS 8	1066	6490	10.990		0.110		1430	10.940	0.016	10.963	0.025	0.023	0.030	96
BS 9	1263	6501	11.063		0.190		1191	11.067	0.007	11.241	0.011	0.174	0.013	96
BS 10	1082	6493	11.251		0.415		1528	10.982	0.054	11.276	0.046	0.294	0.071	84
BS 11	1284	6504	10.940		0.220		1390	10.915	0.009	11.071	0.010	0.156	0.013	76
BS 12	1013	6484	11.550		0.410		1099	11.531	0.007	11.935	0.007	0.404	0.010	75
BS 14	975	6480	11.078		0.430									
BS 15	1466	6511	10.600		0.340									
SG 16	794	5318	12.862	0.010	0.941	0.015	1456	12.841	0.008	13.784	0.010	0.943	0.013	100
SG 17	781	5362	12.725	0.018	0.739	0.026	1322	12.713	0.006	13.448	0.008	0.735	0.010	100
SG 18	1077	5451	12.595	0.003	0.637	0.005	1503	12.567	0.008	13.266	0.014	0.699	0.016	100
SG 20	1245	6114	12.934		0.919		973	12.944	0.003	13.848	0.002	0.904	0.004	99
SG 21		6169	12.906		0.970		1777	12.870	0.003	13.802	0.009	0.932	0.009	99
SG 25	1060	5651	13.051	0.018	0.877	0.025								
SG 26		6228	12.688		0.622									
SG 33	1234	5896	12.650	0.011	0.574	0.017	864	12.617	0.010	13.224	0.010	0.607	0.014	100
SG 36	1268	6177	12.647	0.030	0.581	0.045	1258	12.616	0.004	13.203	0.002	0.587	0.004	99
RG 22	1305	5997	12.230		0.993		1546	12.245	0.014	13.231	0.003	0.986	0.014	96
RG 41	1277	6502	11.630		1.050		1327	11.598	0.008	12.655	0.011	1.057	0.014	98
TO 19		6037	13.037		0.667		2045	12.948	0.006	13.541	0.002	0.593	0.006	100
TO 27		5061	13.025		0.574		1200	12.989	0.009	13.589	0.003	0.600	0.009	100
TO 28		5284	12.844	0.005	0.522	0.007	1752	12.751	0.006	13.289	0.002	0.538	0.006	100
TO 29	731	5335	13.065		0.534		336	13.004	0.009	13.561	0.004	0.557	0.010	100
TO 30	740	5354	13.482		0.551		535	13.451	0.011	14.004	0.001	0.553	0.011	100
TO 31	736	5389	13.374		0.554		426	13.333	0.006	13.908	0.004	0.575	0.007	100

Photometry Data 2.1 – Continued

McGahee	**S77**	**MMJ**					**Y08**							Membership
Star	ID	ID	V (mag)	$e_{(V)}$ (mag)	B-V (mag)	$e_{(B-V)}$ (mag)	ID	V (mag)	$e_{(V)}$ (mag)	B (mag)	$e_{(B)}$ (mag)	B-V (mag)	$e_{(B-V)}$ (mag)	Probability (%)
TO 32		5494	13.594		0.560		1931	13.551	0.004	14.137	0.009	0.586	0.010	100
TO 34	1441	6336	13.151	0.015	0.572	0.022	889	13.148	0.009	13.729	0.003	0.581	0.009	100
TO 35		5850	12.777		0.548		29	14.332	0.014				0.000	99
TO 37		5042	12.856	0.015	0.531	0.022	930	12.793	0.012	13.327	0.014	0.534	0.018	97
TO 0	1456	6224	12.705	0.011	0.575	0.016	1118	12.712	0.008	13.256	0.004	0.544	0.009	94
TO 39		5132	13.411		0.562		382	13.587	0.009	14.204	0.003	0.617	0.009	93
TO 40		5222	12.988		0.540									
TO 49		5191	12.700		0.482		1064	12.789	0.014	13.328	0.013	0.539	0.019	100
TO 50		5239	12.846	0.022	0.501	0.033	1783	12.722	0.018	13.271	0.005	0.549	0.019	100
TO 52	1036	5833	12.784	0.040	0.487	0.056	1252	12.787	0.015	13.294	0.002	0.507	0.015	100
TO 55	1225	6135	12.831		0.504		770	12.863	0.002	13.395	0.009	0.532	0.009	0
YS 13	1425	6509	11.721		0.510		413	11.373	0.003	11.968	0.006	0.595	0.007	0
YS 23		5848	12.253		0.623		2236	12.145	0.005	12.725	0.004	0.580	0.006	5
YS 24	1447	6293	12.429		0.618		980	12.427	0.000	13.031	0.009	0.604	0.009	1
YS 42	1072	6491	11.315		0.610		1476	11.257	0.014	11.921	0.011	0.664	0.018	98
YS 43	1040	6488	11.520		0.870		1289	11.443	0.007	12.343	0.005	0.900	0.009	97
YS 44	1237	6498	10.780		0.940		892	10.696	0.012	11.661	0.009	0.965	0.015	96
YS 45	1023	6487	10.544		0.570		1166	10.452	0.019	11.016	0.040	0.564	0.044	84
YS 46	838	6478	11.520		0.700		2047	11.435	0.008	12.160	0.007	0.725	0.011	0
YS 47	1190	6496	11.260		0.620		90	11.070	0.027	11.769	0.011	0.699	0.029	0
YS 48	1327	6507	11.103		0.850		1915	10.880	0.012	11.644	0.006	0.764	0.013	0
UK 51	1031	5741	13.260	0.008	0.464	0.012	1235	13.273	0.007	13.735	0.003	0.462	0.008	100
UK 53	2223	5871	13.329	0.009	0.495	0.013	1411	13.299	0.009	13.792	0.002	0.493	0.009	99
UK 54	946	5698	13.626		0.473		305	13.580	0.006	14.108	0.011	0.528	0.013	96
UK 56	1005	5571	12.651	0.011	0.517	0.016								
UK 57		6180	13.303	0.007	0.459	0.010								

Chapter 3

Observations

Observations of all target stars were performed with the WIYN 3.5 m telescope and HYDRA multiobject spectrograph at Kitt Peak National Observatory near Tuscon, AZ during four observing runs between October 2011 and May 2012. The 316 lines/mm echelle grating, the blue science fiber cable, the Bench Camera and the 2600x4000 Thinned STA1 CCD with 12 μm-pixels were employed for all observations yielding a dispersion of about 0.12 Å/pixel and a resolution of about 0.25 Å. Over the course of the observing runs, multiple observations were made at each of ten different wavelength settings resulting in 45 observations for most stars. These wavelength settings are listed in Table 3.1 with the corresponding date of the observation, the resolving power ($R = \lambda/\Delta\lambda$) for that wavelength setting, the number of observations made and the elemental lines of interest. Exposure times were varied to achieve a typical S/N $\sim$ 150. Standard reduction methods including overscan correction, bias removal, flat fielding and scattered light corrections were applied to all observed spectra via IRAF[1]. Wavelength calibrations for the observed spectra were obtained from Th-Ar comparison lamp spectra.

Observations of the solar spectrum were also obtained at each wavelength setting using the instrumental setup described above. To accomplish this task, observations of the sky were taken at either dawn or dusk to yield solar spectra in which radial velocity components due to the motions of the earth and sun are not present.

[1]IRAF is distributed by the National Optical Astronomy Observatories, which are operated by the Association of Universities for Research in Astronomy, Inc., under cooperative agreement with the National Science Foundation.

Table 3.1. Wavelength Regions

Date yr/mo/day	$\lambda\lambda$ (Å)	Resolving Power	Number of Observations	Lines of Interest
2011 Oct 28	5745-5985	23000	6	Fe, Ba, Ti
2011 Oct 30	6055-6300	25000	4	Fe, Ni, Si, Ca, Ti, Ba, Na
2011 Dec 21	4980-5235	20000	7	Cr, Y
2011 Dec 21	7640-7985	31000	5	Fe, O
2011 Dec 23	4070-4285	17000	3	Cr, Pb
2011 Dec 24	4070-4285	17000	3	Cr, Pb
2011 Dec 24	8240-8820	34000	5	C
2012 Feb 19	6430-6840	27000	2	Fe, Ni, Ca, Al, C, Li
2012 Feb 20	8060-8430	33000	3	N
2012 May 18	4580-4770	19000	2	Cr, Ti
2012 May 19	6165-6465	25000	4	Fe, Cr, Ni, Si, Ca, Ti, Ba, Na

Note. — This table details the observations that were made at each wavelength setting over the course of four observing runs. Note that the 4070-4285 Åsetting was observed on two nights, December 23 and December 24.

During both target and sky observations, 57 fibers of the science fiber cable were utilized to simultaneously image the selected target stars in M67 and sky respectively. As will be discussed in § 4, when a stellar spectrum is compared directly to a solar spectrum for the purposes of determining a radial velocity in the present work, the solar spectrum used in the comparison was obtained using the same fiber on which the star in question was observed.

In addition to the observations described above, a set of telluric absorption line spectra taken by J.R. King at McDonald Observatory will be referred to in § 4. These spectra were taken with the McDonald Observatory 2.7 m telescope and the 2D-coudé spectrograph yielding a resolving power of of R = $60,000$. Further details on this set of observing instrumentation can be found in King (1997).

Chapter 4

Radial Velocity Determinations

The radial velocity of a star is defined as the speed that the star moves either toward (negative values) or away from (positive values) an observer. This movement will result in a Doppler shift of the spectral features observed for a star according to:

$$\Delta\lambda = \frac{\lambda_{\rm rest} * {\rm v_r}}{\rm c} \tag{4.1}$$

where $\lambda_{\rm rest}$ is the rest wavelength of a particular feature, $\rm v_r$ is the radial velocity of the star and c is the speed of light. Ideally, one compares a stellar spectrum which is expected to exhibit this type of Doppler shift to a template spectrum which is expected to exhibit spectral features at their rest wavelengths. This comparison can be used to determine the amount by which the stellar spectrum has been Doppler shifted, and in turn, to determine a radial velocity for the star. Figure 4.1 shows an observed solar template spectrum that ideally exhibits spectral features at their rest wavelengths. It also shows an observed stellar spectrum for YS 47 which is Doppler shifted to longer wavelengths, or redder colors. A radial velocity can be computed for the YS using IRAF's FXCOR package which Fourier transforms of each spectrum and convolves the two transforms to compute a cross correlation function (CCF). The amount by which the stellar spectrum is shifted from the template spectrum is derived from the location of the peak of the CCF which can then be converted into an associated radial velocity. The uncertainty reported by FXCOR measures the goodness of fit of the CCF and is typically an underrepresentation of the uncertainty in the radial velocity determination for the object. In the case of a resolvable double lined spectroscopic binary (SB2) system the cross

correlation will generate a function with a double peak where each peak corresponds to an individual component of the binary system. FXCOR is capable of deblending a double peaked CCF so that one can determine the shift of each peak individually. Using this capability, radial velocities were computed for each component in the cases where the target was an SB2 system.

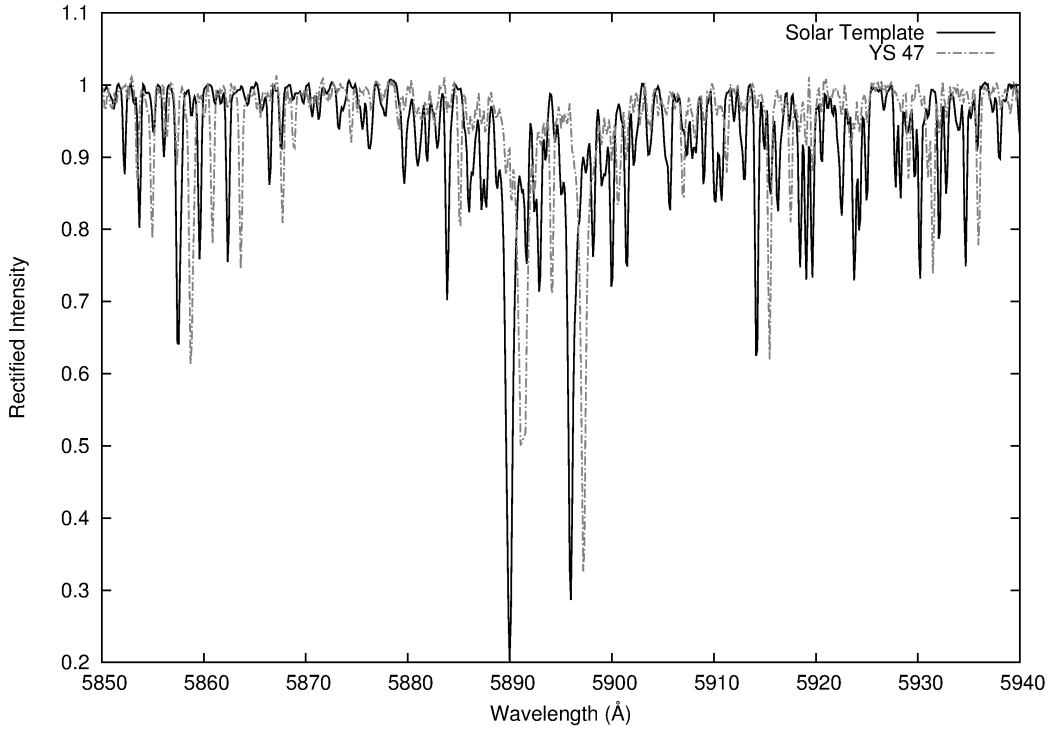

Figure 4.1: Example spectra are shown for the solar template spectrum (solid black line) and a stellar spectrum for YS 47 (dashed gray line).

Radial velocities were initially determined for the each TO target by cross correlating each of the 45 observed stellar spectra with a co-added solar template spectrum that was observed with the same optical fiber. However, this process revealed two sources of systematic shifting of the radial velocity data, both of which can be seen in Figure 4.2 for four of the TO stars. These types of shifts were present in the radial velocity data for all of the TO stars, but the problem can be illustrated using just these four stars. These shifts in the radial velocity data will be discussed presently, because in one case, the shifts prompted a different approach to computing the radial velocities of the stars. In the second case, it was determined that the radial velocity data should not be used in computing the statistics for the radial velocity data.

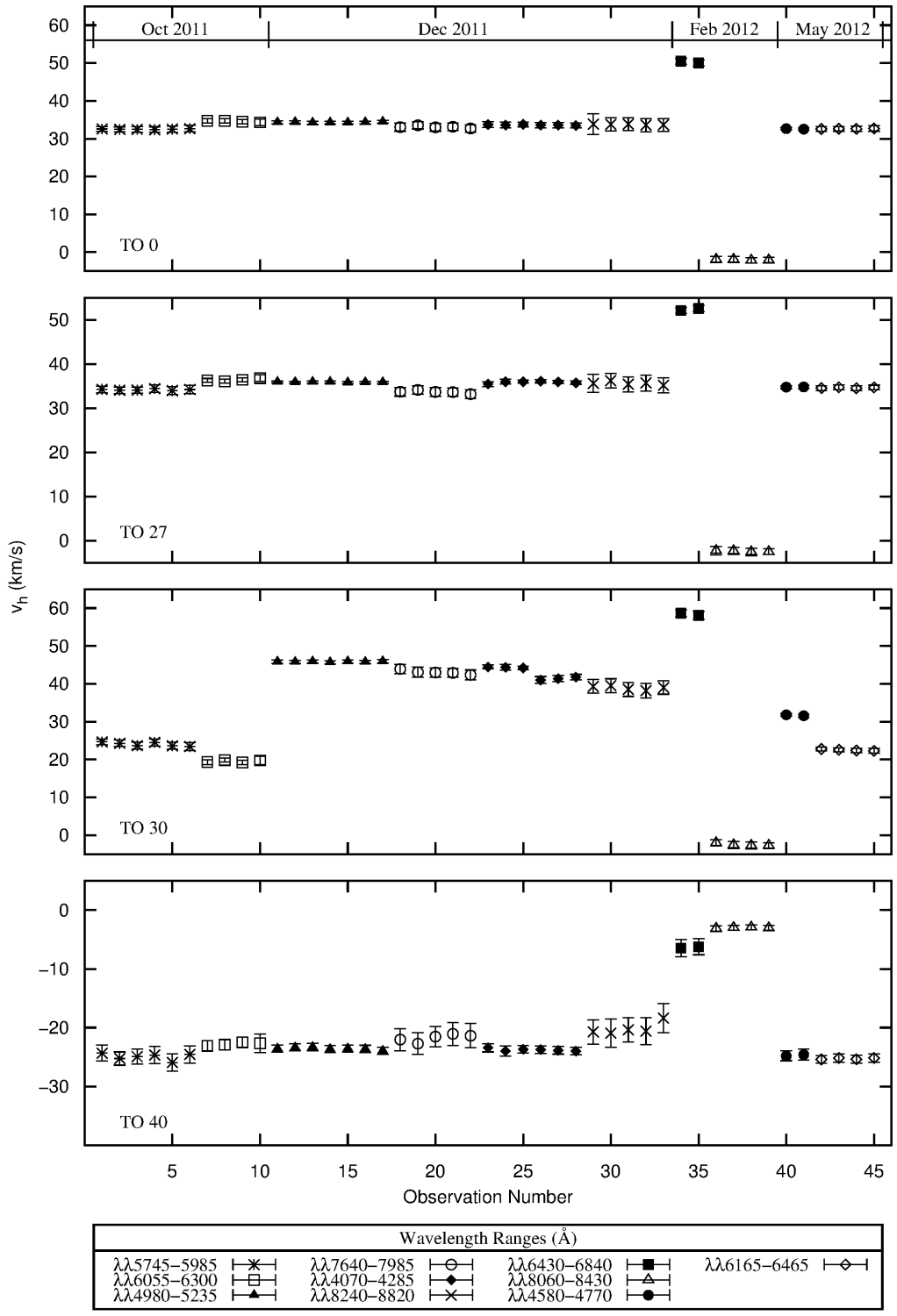

Figure 4.2: Radial Velocity Plots for TO0, TO27, TO35 and TO37 illustrating systematic shifts in the radial velocity data.

4.1 The $\lambda\lambda$6430-6840 Region

The shift in the $\lambda\lambda$6430-6840 region radial velocity data appears to be shifted roughly 15 km/s above the average radial velocity for the remaining wavelength regions. This shift is likely caused by an instrumental shift of both the solar and stellar spectra on the CCD. The velocity dispersion of the CCD is ~ 9.26 km/s/pixel, therefore, a shift of 15 km/s in the radial velocity data corresponds to a shift of the data on the CCD by ~ 1.5 pixels. A shift of this size could have been caused by reconfiguring the telescope and associated equipment multiple times between the time that the stellar observations for this region were made at the beginning of the night, and the time that the solar template spectra were taken at the end of the night.

To adjust for this instrumental shift, individual telluric absorption lines were utilized. Telluric absorption lines are lines that are present in the observed solar template and stellar spectra due to observing through earth's atmosphere. In ideal spectra, these lines are expected be located in identical positions on the CCD for both the solar template and stellar observations. If the telluric lines are located in different positions on the CCD, as was the case for the $\lambda\lambda$6430-6840 region, it indicates that the data have been shifted on the CCD, and does not correspond to a radial velocity shift of the spectral data. These telluric lines can be, and were, used to remove the instrumental shift before performing a cross correlation to determine a true heliocentric radial velocity for each TO star.

In most cases, five telluric lines were located and their positions were measured for each TO and its corresponding solar template. These locations were compared to the locations of the telluric lines in spectra observed by J. R. King at McDonald Observatory using the observing setup described in §3 to determine a corrective shift from each of the individual telluric lines. These individual corrective shifts were then averaged for each TO star. Computing the corrective shifts in this way, however, introduces an additional systematic uncertainty to the radial velocity data. The assumption that the shift in this region is instrumental in nature, indicates that the shift should be the same for each star. Therefore, the standard deviation of the mean shifts computed for all of the TOs indicated that radial velocities could be measured to no better than ± 1.0 km/s for this particular wavelength region.

Though it is most evident in the $\lambda\lambda$6430-6840 region, instrumental shifting is likely present in the radial velocity data for all of the wavelength regions. The correction technique discussed

above can be difficult to accomplish because, as was previously mentioned, it relies on the presence of telluric absorption lines in the spectra. In most wavelength regions the number of telluric lines is limited, so it is likely that correcting each wavelength region for instrumental shifts would introduce a typical additional systematic uncertainty of ±1.0 km/s to all of the radial velocity data. There is, however, a method to avoid introducing this amount of systematic uncertainty into the radial velocity data for each star. Recall that the instrumental shift imposed on the spectra is assumed to be the same for each exposure of the target stars. Therefore, using a chosen stellar spectrum from an exposure as the template spectrum can provide a radial velocity for each of the remaining stars in the exposure relative to the chosen stellar template and can eliminate the effects of any potential instrumental shift. This approach was used in the end to determine the radial velocities of the target stars in the current work, and will be described in more detail in §4.3.

4.2 The $\lambda\lambda$8060-8430 Region

It can be seen in Figure 4.2 that the radial velocity data for the $\lambda\lambda$8060-8430 region correspond to roughly -2 km/s for each of the TOs presented. The reason for this is that the spectrum in this region is heavily dominated by telluric absorption lines caused by observing through the earth's atmosphere. As previously mentioned, in ideal spectra, these telluric absorption lines will be located in identical positions on the CCD for both the solar template and stellar spectra. Therefore, a cross correlation between these solar template and stellar spectra that are dominated by telluric absorption lines will yield a corresponding "radial velocity" value of zero because the CCF will be dominated by those telluric lines as well. The fact that the radial velocity derived from this region is -2 km/s implies that there is also some instrumental shift imposed on this region that is smaller but similar to the instrumental shift seen in the $\lambda\lambda$6430-6840 region. The cross correlation of the telluric lines in this case simply measures the amount of instrumental shift.

In order to correct for this effect, the amount of instrumental shift in a given spectrum was first determined by cross correlating a region of the spectrum that is known to be populated by only telluric lines–$\lambda\lambda$8223-8236 with the same region in the McDonald telluric absorption spectra observed by J. R. King. This procedure was performed for both the stellar spectra and solar template spectra to determine the shift present in each spectrum and then each individual shift was removed from the corresponding spectrum. Then five non-telluric lines ($\sim \lambda$ 8085.2, λ 8183.2, λ 8248.5, λ 8327.1,

λ 8387.8) were located in both the stellar and solar template spectra to be used in a cross correlation to determine a heliocentric radial velocity for the star in question. This process was repeated for each of the four observations in this region.

In this case, each application of a correctional shift to a spectrum introduced an additional uncertainty. The uncertainty introduced was computed in the cross correlation to determine the amount of correctional shift to be applied. For a given star, the uncertainty introduced by shifting the co-added solar spectrum was added in quadrature to the uncertainty introduced by shifting the stellar spectrum. The total shift uncertainty was then added linearly to the uncertainty computed in the heliocentric radial velocity cross correlation.

4.3 A Final Approach to Determining Radial Velocities

Because a multiobject spectrograph was used for observations, all targets were imaged simultaneously for a given exposure, thus, the amount of instrumental shift is presumably the same for each fiber (or target) in a given exposure. Replacing the solar spectrum template, which is subject to a different amount of instrumental shift than the targets, with a stellar spectrum template that is subject to the same amount of instrumental shift as all of the other targets, eliminates the need to correct for the instrumental shift imposed on the stellar spectra. Performing a cross correlation between a given target and a stellar template yields a radial velocity for the target in question relative to the chosen stellar template and removes the effects of the instrumental shift.

In order to use a stellar spectrum as a template, it is first necessary to select a target with a constant radial velocity and then to determine a zero point heliocentric radial velocity for that template star. Both the TOs and the SGs were surveyed to select the template star since they would likely provide the most "normal" set of stars of in the target sample. Each of the 13 TOs and 11 SGs in the target list were cross correlated with their corresponding co-added solar spectra for each wavelength region, barring the discrepant $\lambda\lambda$6430-6840 and $\lambda\lambda$8060-8430 regions. The turnoff star, TO 0, showed the least amount of variation when its radial velocity values were computed in this way; the standard deviation of the radial velocity measurements for this star was 0.74 km/s.

To determine the heliocentric radial velocities for each observation of TO 0, three methods were employed: 1) for the $\lambda\lambda$6430-6840 region, the instrumental shifts were corrected before determining heliocentric radial velocity measurements using the method described in §4.1 2) for the

$\lambda\lambda$8060-8430 region, the instrumental shifts were corrected before determining heliocentric radial velocity measurements using the method described in §4.2 3) for the remaining wavelength regions, no corrections were made before cross correlations were performed between the stellar spectrum and the corresponding co-added solar spectrum for each observation to determine the remaining values for the heliocentric radial velocity of TO 0. A plot of the all of the heliocentric radial velocity measurements for TO 0, including the corrected $\lambda\lambda$6430-6840 and $\lambda\lambda$8060-8430 measurements, can be seen in the top panel of Figure 4.3. The 45 heliocentric radial velocity measurements were averaged to determine a mean "zero point" heliocentric radial velocity of $\overline{\mathrm{v}}_{\mathrm{h,o}} = 33.6 \pm 0.1\mathrm{km/s}$.

Heliocentric radial velocities were determined for the observations made in the $\lambda\lambda$8060-8430 region using the method prescribed in §4.2 for each star. In all remaining wavelength regions, radial velocities were computed using the following method. For a given target, a cross correlation was performed between each individual spectrum of the target and the corresponding template spectrum for TO 0 from the same observation. This yielded a radial velocity for the target relative to the template TO 0. The zero point heliocentric radial velocity for TO 0, $\overline{\mathrm{v}}_{\mathrm{h,o}}$, was then added to each relative radial velocity measurement of the target to determine a heliocentric radial velocity for each observation made at each wavelength region.

Once heliocentric radial velocities had been computed for all observations in all wavelength regions for a target, the null hypothesis that the target has a constant radial velocity was adopted and the following were computed excluding the $\lambda\lambda$8060-8430 region data (see §4.4 below for details): 1) a mean heliocentric radial velocity, $\overline{\mathrm{v}}_{\mathrm{h}}$ 2) a sample standard deviation given by:

$$\sigma_{\mathrm{v_h}} = \sqrt{\frac{1}{\mathrm{n}-1}\sum_{\mathrm{i}=1}^{\mathrm{n}}(\mathrm{v_{h,i}} - \overline{\mathrm{v}}_{\mathrm{h}})^2} \tag{4.2}$$

where $\mathrm{v_{h,i}}$ are the individual heliocentric radial velocity measurements, $\overline{\mathrm{v}}_{\mathrm{h}}$ is the mean heliocentric radial velocity and n is the number of heliocentric radial velocities that were measured for the target 3) an uncertainty in the mean, or standard error, given by:

$$\sigma_{\mu,\mathrm{v_h}} = \frac{\sigma_{\mathrm{v_h}}}{\sqrt{\mathrm{n}-1}} \tag{4.3}$$

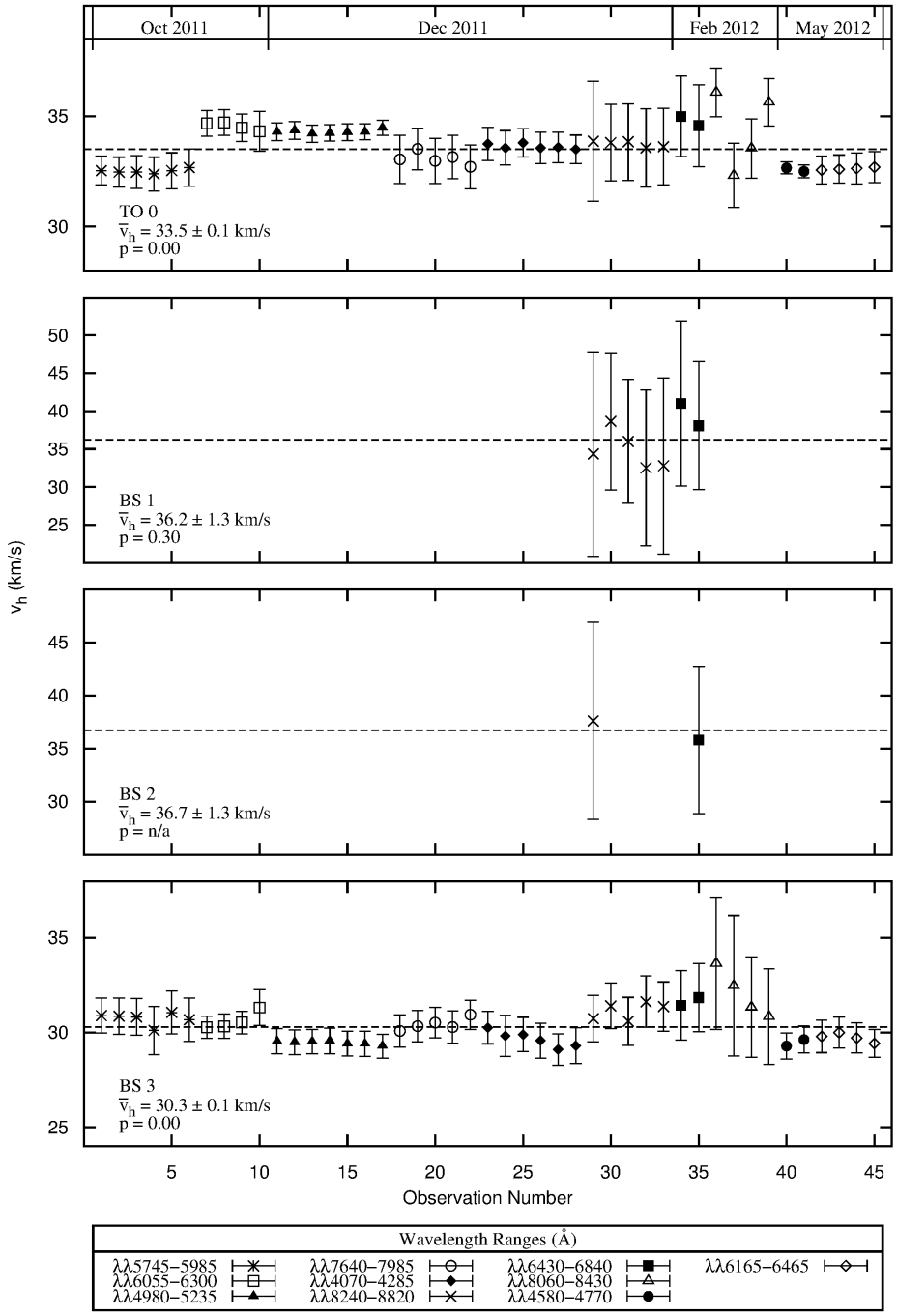

Figure 4.3: Radial Velocity Plots for TO0, BS1, BS2 and BS3. Note that for stars that exhibit variable radial velocity measurements, the mean value computed in the present work is not representative of a systemic radial velocity for the binary system. It is simply an average of the radial velocity measurements computed.

4) a reduced Chi-squared statistic given by:

$$\chi^2_\nu = \frac{\sum_{i=1}^{n} (v_{h,i} - \overline{v}_h)^2}{(n - 1 - dof)} \tag{4.4}$$

where all parameters are the same as in 2) and dof represents the degrees of freedom in the null hypothesis model, i.e. dof = 1 in this case and 5) a Chi-squared probability, p_χ; a value of $p_\chi = 0$ indicates that there is zero probability that a χ^2_ν statistic would be found, by chance, to be as large as the value calculated for that star. Given the null hypothesis that an object has a constant radial velocity, this means that the object associated with $p_\chi = 0$ is unlikely to have a constant radial velocity. Conversely, the higher the p_χ value, the more likely the object is to exhibit a constant radial velocity. The parameters described above are listed in Table 4.1 in addition to radial velocity data from Mathieu et al. (1986) and Yadav et al. (2008). The Mathieu et al. (1986) data include a mean heliocentric radial velocity value, $\overline{v}_h$, the standard deviation of the radial velocity measurements σ_{v_h}, pertinent notes about the nature of the object observed and the number of observations. The Yadav et al. (2008) data include a, presumably, single heliocentric radial velocity measurement, v_h, and the uncertainty they report is simply the output of their cross correlation pipeline σ_{p,v_h}. Yadav et al. (2008) remark that these formal fitting errors underestimate the true uncertainty of the radial velocity measurements, but that the reported values "retain the information on the goodness of fit of the cross correlation function." They also found a systematic uncertainty of up to ~ 0.6km/s and recommend that to find the true uncertainty of the radial velocities, one could add the systematic uncertainty and the formal fitting error in quadrature. These values have been computed in the present work and are found in the column marked σ_{μ,v_h} in the Yadav et al. (2008) columns of Table 4.1. A more detailed comparison of these three studies will be discussed in §6.

Table 4.1: Radial Velocity Data

	Y08			**M86**				**McGahee**						
Star	v_h (km/s)	σ_{p,v_h} (km/s)	σ_{μ,v_h} (km/s)	$\bar{v}_h$ (km/s)	σ_{v_h} (km/s)	notes	# of meas	$\bar{v}_h$ (km/s)	σ_{v_h} (km/s)	σ_{μ,v_h} (km/s)	notes	# of meas.	χ^2_ν	p_χ
TO0				31.3	0.3		5	33.5	0.8	0.1		41	2.25	0.00
BS1	-29.7	0.8	1.0					36.2	3.2	1.3		7	1.22	0.30
BS2	-28.3	0.3	0.7					36.7	1.3	1.3		2		
BS3				29.6	0.7		8	30.3	0.8	0.1		41	8.46	0.00
BS4								33.4	1.1	0.2		41	20.87	0.00
BS5								49.5	5.7	3.3		4	4.73	0.01
BS6								31.1	2.8	0.5		39	1.47	0.03
BS7	24.6	0.3	0.7					36.2	3.1	0.5		39	6.76	0.00
BS8	-51.4	0.8	1.0					37.3	5.0	1.2		18	2.10	0.01
BS9								33.0	1.1	0.2		41	14.00	0.00
BS10				33.3	2.0		26	34.5	1.8	0.3		41	90.02	0.00
BS11								34.7	9.5	1.7		32	6.55	0.00
BS12								29.3	0.7	0.1		41	3.16	0.00
BS14								30.5	1.7	0.3		41	2.91	0.00
BS15								27.8	2.4	0.4		41	0.84	0.75
SG16				33.7	0.3		2	33.9	0.4	0.1		41	0.25	1.00
SG17	32.8	0.0	0.6	33.0	0.4		2	32.1	0.4	0.1		41	0.47	1.00
SG18a						SB2	14	36.6	18.3	2.9	SB3	41	158.19	0.00
SG18b								61.0	20.0	4.3		23	58.11	0.00
SG18c								-21.6	19.9	6.6		10	8.25	0.00
SG20	33.0	0.0	0.6	32.8	0.7		4	32.8	0.8	0.1		41	0.74	0.88
SG21				34.7	0.7		2	33.9	0.7	0.1		41	0.51	1.00
SG25				33.7	1.5		3	33.7	0.4	0.1		41	0.43	1.00
SG26				32.5	1.0		8	32.4	0.5	0.1		41	0.80	0.81
SG33	28.1	0.1	0.6			SB2	32	35.1	6.7	1.1	SB2	41	97.70	0.00
SG36				33.4	0.5		6	32.4	0.3	0.1		41	0.53	0.99
RG22	34.0	0.0	0.6	33.7	0.5		16	34.1	0.5	0.1		41	0.28	1.00
RG41				34.0	0.5		21	33.9	0.5	0.1		41	0.26	1.00
TO19								31.1	0.6	0.1		41	0.66	0.95
TO27	35.6	0.1	0.6					35.5	0.4	0.1		41	0.45	1.00
TO28				34.4	1.9		10	32.8	0.3	0.1		12	0.90	0.53

Radial Velocity Data 4.1 – Continued

Star	**Y08** v_h (km/s)	σ_{p,v_h} (km/s)	σ_{μ,v_h} (km/s)	**M86** $\overline{v}_h$ (km/s)	σ_{v_h} (km/s)	notes	# of meas	**McGahee** $\overline{v}_h$ (km/s)	σ_{v_h} (km/s)	σ_{μ,v_h} (km/s)	notes	# of meas.	χ^2_ν	p_χ
TO29								33.0	0.6	0.1		41	1.17	0.21
TO30								35.1	10.0	1.6		41	324.61	0.00
TO31	32.4	0.1	0.6					31.4	5.5	0.9		41	137.67	0.00
TO32	41.2	0.2	0.6					38.7	4.5	0.7		41	92.04	0.00
TO34								34.4	0.8	0.1		41	2.51	0.00
TO35	34.1	0.1	0.6	34.4	0.5		5	34.1	0.5	0.1		41	0.78	0.83
TO37	33.5	0.1	0.6					32.9	0.5	0.1		41	0.79	0.83
TO39								33.1	0.5	0.1		41	0.96	0.54
TO40								-23.8	0.7	0.1		41	0.52	0.99
TO49	34.4	0.1	0.6	33.2	0.9		6	34.3	0.6	0.1		41	0.90	0.66
TO50								46.1	0.8	0.1		41	1.61	0.01
TO55								0.5	0.6	0.1		41	0.63	0.96
YS13	49.6	0.0	0.6					49.2	0.8	0.1		41	1.45	0.03
YS23								36.1	0.7	0.1		41	1.46	0.03
YS24	52.9	0.3	0.7					35.8	0.4	0.1		41	0.66	0.95
YS42	33.6	0.0	0.6	32.2	2.2	SB1	38	30.2	0.8	0.1		41	2.07	0.00
YS43				32.0	6.3	SB1	36	29.4	5.9	0.9		41	113.47	0.00
YS44				33.0	3.5	SB1	37	36.5	2.0	0.3		41	9.99	0.00
YS45	4.0	0.0	0.6	3.6	1.0		3	5.3	1.1	0.2		41	2.16	0.00
YS46A						SB2	2	49.3	8.0	1.3	SB2	41	46.46	0.00
YS46B								54.9	14.2	4.3		12	45.24	0.00
YS47								94.4	1.0	0.2		41	2.14	0.00
YS48				12.0	0.4		2	12.0	0.7	0.1		41	0.48	1.00
UK51								29.9	9.2	1.5		41	90.40	0.00
UK53								35.8	0.9	0.1		41	0.77	0.85
UK54								34.5	0.7	0.1		41	0.56	0.99
UK56				34.7	2.4		10	32.7	1.1	0.2		41	3.77	0.00
UK57								66.7	1.0	0.2		41	0.90	0.66

The final radial velocity plots for three of the BSs stars observed for the current study can be seen in the bottom three panels of Figure 4.3. The radial velocity plots of the remaining stars studied in the current work can be found in Appendix B in Figures: 4, 5, 6, 7, 8, 9, 10, 11, 12, and 13. Each plot is labeled with the star identification number, the mean heliocentric radial velocity with standard error and the Chi-squared probability all determined in the present work. Note that the abscissa in these plots simply indicates the observation number and is not a timeline for the observations. It is remarked here that in the case of a target that exhibits radial velocity variation, the mean radial velocity value computed is not the systemic radial velocity of the likely binary system. It is simply an average of the derived radial velocity measurements. Currently, there is not enough data to determine orbital periods for these objects, thus systemic radial velocities cannot be determined. Collection of additional data in the future will hopefully make orbital parameter determinations possible for targets that are likely in binary systems.

4.4 Exclusion of the $\lambda\lambda$8060-8430 Region

The purpose of monitoring the radial velocities of these stars over time is to determine if they exhibit variability; if they do, then the star likely exists in a binary system. Due to the fact that the radial velocities in the $\lambda\lambda$8060-8430 region were computed by cross correlating only five spectral features, there appears to be more scatter in the radial velocity data for this region that does not appear in the other wavelength regions. This is seen for many of the stars' radial velocity plots (see Figure 4.3 and Appendix B). This amount of scatter was not successful in altering the mean radial velocities computed for the TOs as can be seen in the left panel of Figure 4.4. However, the scatter present in this region causes a lower Chi-squared probability to be computed when the data are included as can be seen in the right panel of Figure 4.4. The explicit values computed both including the $\lambda\lambda$8060-8430 region data, and leaving it out, can be found in Table 4.2. It can be seen in both the figures and the table values, that when the $\lambda\lambda$8060-8430 region data are included in the Chi-squared probabilities in particular, it can lead one to determine that a star exhibits a variable radial velocity when, in reality, it is likely constant. This, in turn, can lead to an overestimation of the number of binaries in the population. Because of this effect, the $\lambda\lambda$8060-8430 region data was excluded from all computations described above in §4.3.

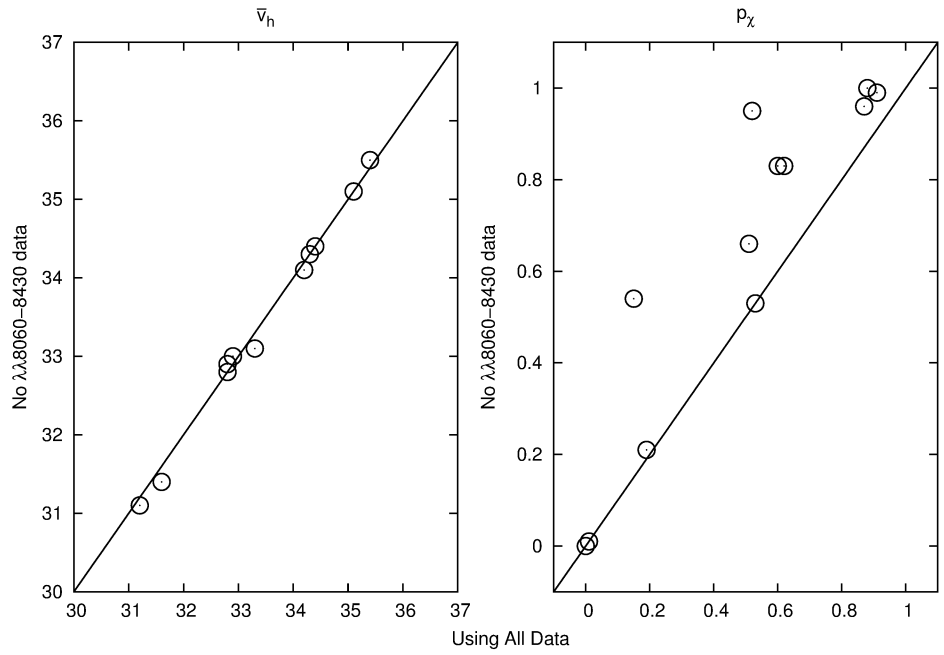

Figure 4.4: The left panel in this plot compares the mean radial velocities computed for TOs using all of the 45 radial velocity data points and the mean radial velocity determined when the $\lambda\lambda$8060-8430 region was excluded from the computation. The right panel compares the Chi-squared probability computed using all of the available radial velocity data for the TOs to the Chi-squared probabilities determined when the $\lambda\lambda$8060-8430 region was excluded from the computation. The solid line in both panels indicates a 1-to-1 line for reference.

Table 4.2: Mean radial velocities and Chi-squared probabilities for TOs computed using all data and computed excluding the $\lambda\lambda$8060-8430 region data.

	Using all RV data		**No $\lambda\lambda$8060-8430 data**	
Star	$\overline{v}_h$ (km/s)	p_χ	$\overline{v}_h$ (km/s)	p_χ
19	31.2	0.52	31.1	0.95
27	35.4	0.88	35.5	1.00
28	32.8	0.53	32.8	0.53
29	32.9	0.19	33.0	0.21
30	35.1	0.00	35.1	0.00
31	31.6	0.00	31.4	0.00
32	38.6	0.00	38.7	0.00
34	34.4	0.00	34.4	0.00
35	34.2	0.60	34.1	0.83
37	32.8	0.62	32.9	0.83
39	33.3	0.15	33.1	0.54
40	-23.7	0.91	-23.8	0.99
49	34.3	0.51	34.3	0.66
50	46.0	0.01	46.1	0.01
55	0.6	0.87	0.5	0.96

Chapter 5

Chemical Abundance Determinations

A detailed chemical abundance analysis was performed for a subset of the target list utilized in the radial velocity study. The purpose of this abundance analysis is to compare the abundance pattern of the YSs to "normal" cluster members. The subset of targets investigated in the abundance analysis, hereafter referred to as List B, is comprised of all of the YSs regardless of membership probabilities and/or radial velocity data, all of the SGs with the exception of the secondary (B) component of SG 46, both RGs and four TOs selected by their high membership probabilities, $\overline{v}_h$ values that agree with the cluster mean (33.5 ± 0.5 km/s) derived by Mathieu (1983) and high p_χ values.

Individual spectra were utilized in the radial velocity survey of §4 so that the maximum amount of information regarding the variability of the measurements was retained, however, for the purpose of conducting the abundance analysis, it is more beneficial to co-add the spectra for each wavelength region to increase the S/N ratio of the data. Any mention of stellar or solar spectra in this chapter, therefore, refers to a co-added spectrum. Note that to determine the solar abundances, the only solar spectra used were those taken with the same fiber used to image the radial velocity template star TO 0.

Before discussing the specific steps of a chemical abundance analysis, it is important to note that in this study, a differential chemical abundance analysis has been employed. This type

of analysis has been performed to eliminate one of the largest sources of uncertainty in a chemical abundance analysis. This uncertainty is introduced in determining an accurate gf value associated with a particular spectral line, or atomic transition. The gf value is really a combination of two individual values for g and f. In the context of a gf value, g is often referred to as the statistical weight of a transition and describes the number of ways in which a transition can take place. Care should be taken to not confuse this g with $\log(g)$ which describes the surface gravity of a star and will be discussed later. f is known as the oscillator strength and describes the probability that a specific transition will take place. It is standard practice to combine the g and f values for a particular spectral line to establish a single gf value for the line. Very few lines have gf values that can be determined analytically, but these values can be measured in the lab with some difficulty. Though accurate gf values have been pursued in the lab for some time, they still present a significant source of uncertainty in abundance measurements.

A differential chemical abundance analysis averts the inclusion of uncertainties due to inaccurate gf values by using the ratio of two equivalent width values of a specific spectral line. One of the equivalent width values is that measured in the target of interest, and the other is the equivalent width measured in some reference spectrum. In the present study, the reference spectrum will be that of the sun. The use of spectral line equivalent widths to determine an elemental abundance will be discussed in the following sections, but currently, it suffices to mention two things: 1) the number of absorbers associated with at particular spectral line can be computed from the equivalent width of that line and 2) the equivalent width of a spectral line is proportional to the gf value associated with that line. In this differential analysis, the *ratio* of the number of absorbers is sought and requires the *ratio* of the equivalent width of a spectral line measured in the star to the equivalent width of the same line measured in the sun. Therefore, the gf value associated with the line will cancel in the ratio of the equivalent widths and this ratio can then be used to calculate the ratio of the number of absorbers without imposing the uncertainty of the gf value on the calculation.

The total number of particles (atoms and ions) of a particular element can be determined using the Boltzmann and Saha equations (Equations 5.3 and 5.8 respectively) for a given number of atoms in a particular excitation or ionization state, i.e. a given number of absorbers for a particular spectral line. The number abundance of an element, defined by Gray (2005) to be $\mathrm{A_X} = \frac{\mathrm{N_X}}{\mathrm{N_H}}$ (where $\mathrm{N_H}$ is the total number of hydrogen particles per unit volume and likewise, $\mathrm{N_X}$ is the total number of element 'X' particles per unit volume) can be determined from the number of absorbers

for a particular spectral line if one knows the value of N_H. As previously mentione, the differential analysis that has been employed in this study, utilizes a ratio of the number abundance of an element in the star to the number abundance of the same element in the sun in order to eliminate the need for accurate gf values. Therefore, the abundances reported will be of the typical form "[X/H]" which indicates the logarithmic abundance of any element, 'X', with respect to hydrogen, H, relative to the solar abundance of the element 'X' with respect to hydrogen. These abundances can be determined from:

$$[X/H] = \log\frac{A_{X,star}}{A_{X,sun}} = \log(\frac{N_X}{N_H})_{star} - \log(\frac{N_X}{N_H})_{sun} \tag{5.1}$$

Also note, that in the cases for Fe and Ti, both neutral and singly ionized lines were measurable in most of the stellar spectra. The notation [Fe I/H] indicates a total Fe abundance computed using only the measurements of the neutral Fe I lines where as [Fe II/H] indicates a total Fe abundance computed using only the measurements of singly ionized Fe II lines. In theory, [Fe I/H] should equal [Fe II/H] for any given star.

5.1 Constructing Stellar Atmosphere Structures

The first step in conducting a chemical abundance analysis for a star is to determine the stellar atmosphere parameters effective temperature (T_{eff}), surface gravity ($\log(g)$), metallicity ([M/H]) and microturbulent velocity (ξ_t) from which the structure of the stellar atmosphere will be determined. In this study, a classical spectroscopic approach of Fe excitation-ionization balancing (Fe balance) was used to achieve this goal of determining the final stellar atmosphere parameters for each target. Before performing the Fe balance, however, a number of preliminary steps must be completed. Each of these steps will be described in detail, but an overview of the general steps involved can be helpful, so a summary is provided: 1) initial stellar atmosphere parameters are determined for the target 2) an initial stellar atmosphere structure is determined from stellar atmosphere models according to the initial stellar atmosphere parameters 3) equivalent widths of the Fe I and Fe II lines are measured in the target spectra 4) any correlation between the excitation potential (EP) and the reduced equivalent width (REW) is removed for the Fe I lines. Once these steps have been completed, an iterative Fe balance can be performed by first inferring an Fe abundance for each equivalent width measured for both the Fe I and Fe II lines and subsequently looking for correlations

between the inferred abundances and other spectral line parameters like EP and REW. The four initial steps and the iterative Fe balance are described in more detail in the following paragraphs.

Initial Stellar Atmosphere Parameters

Initial values for the various stellar atmosphere parameters were estimated in a variety of ways, depending on the parameter in question and the target in question. The initial values for [M/H] were taken to be zero for all targets since M67 has been shown to exhibit near solar metallicity (see §6.2.1). Initial values for T_{eff} and $\log(g)$ were derived for each target in List B by adopting the values of T_{eff} and $\log(g)$ that were generated for closest point in the isochrone (see Figure 1.2) that was fit to the M67 members. This task was simple for the SG, RG and TO stars because these stars lie along the isochrone. For each of these targets, the closest isochrone data point was located and the T_{eff} and $\log(g)$ values were adopted for the target in question. The YSs, however, do not lie along the isochrone, so an associated position along the subgiant branch (SGB) was extrapolated from each YS's B-V color index, and an associated position along the red giant branch (RGB) was extrapolated from each YS's V magnitude. The T_{eff} value for each YS was adopted from the extrapolated position along the SGB of the isochrone (associated with B-V) and the $\log(g)$ value for the YS was adopted from the extrapolated position along the RGB of the isochrone (associated with V mag). The initial values for ξ_t were calculated from the initial values of T_{eff} and $\log(g)$ using the following equation from Edvardsson et al. (1993):

$$\xi_t = 1.25 + (8 \times 10^{-4})(T_{eff} - 6000) - 1.3(\log(g) - 4.5)\ \mathrm{km/s} \tag{5.2}$$

derived for stars with $5550 < T_{eff} < 6800$, $3.8 < \log(g) < 4.5$, and $-1.1 < [M/H] < 0.3$.

Initial Stellar Atmosphere Structures

Interpolation between the lattice points in the Kurucz (1992) grid of stellar atmosphere models was the method used to establish a stellar atmosphere structure that corresponded to the initial stellar atmosphere parameters. The Kurucz models assume a 1-D plane parallel model atmosphere in both hydrostatic equilibrium and in local thermodynamic equilibrium (LTE) (Kurucz, 1970) and describe the structure of the stellar atmosphere for a given set of stellar atmosphere parameters. An initial stellar atmosphere structure was determined for each target using this interpolation technique. Additionally, a solar atmosphere structure was established by interpolating from the Kurucz (1992)

grid using the solar atmosphere parameter values $T_{eff} = 5777\,K$, $\log(g) = 4.44$, [M/H] = 0.00 and $\xi_t = 1.10\,km/s$

Fe I and Fe II Equivalent Widths

Each line in the Fe I and Fe II line lists of Bubar & King (2010) were located in both the stellar and solar spectra and in cases where the line appeared to be unaffected by cosmic rays or blending with neighboring lines, the line's equivalent width was measured using SPECTRE[1], a program designed to manipulate single order spectra (Sneden et al., 2012b). This program measures equivalent widths by fitting a Gaussian profile to each spectral line based on user inputs of the continuum level, the line depth and the line width. Note that in the following steps, problematic lines were removed from the line list of each target on a case-by-case basis so the line lists for individual targets are different. The final Fe I and Fe II line lists and their measured equivalent widths in each star and in the sun can be found in Appendix C in Tables 2, 3, 4 and 5.

Removing EP-REW Correlations

The Fe balance method relies on removing any correlation between the inferred Fe abundances and the EPs of measured Fe I lines and also on removing any correlation between the inferred Fe abundances and the REWs of those measured lines. Therefore, any correlations between EP and REW must first be removed (or at least reduced) to prevent the abundance-EP correlation and the abundance-REW correlation from being dependent on each another. To check for an EP-REW correlation for a given target, each Fe I line was plotted according to its associated excitation potential, as reported by Bubar & King (2010), and its reduced equivalent width, or simply, the equivalent width measured for the line divided by the central wavelength of the line measured. The plot generated for TO 35 can be seen in the top panel of Figure 5.1. A linear fit was generated for this plot, its slope indicating that there was, indeed, a slight negative correlation between log(REW) and EP for the Fe I lines that were measured in the TO 35 spectra. Fe I lines that enhanced this correlation were identified and removed from the line list to reduce this effect. The resulting plot can be seen in the bottom panel of Figure 5.1. The process outlined above was performed for the sun and for each target in List B. In each case, correlation enhancing Fe I lines were removed from the line list so that the slope of the linear fit was between -0.02 and 0.02. The resulting Fe I line list was utilized in the following steps.

[1] http://www.as.utexas.edu/ chris/spectre.html

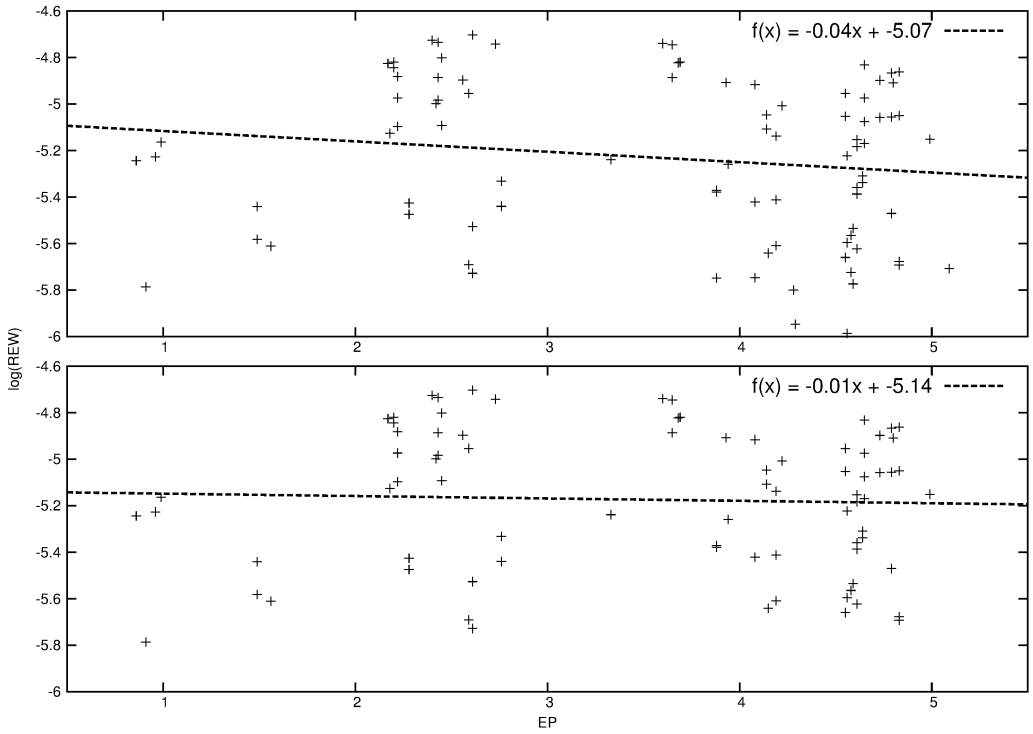

Figure 5.1: Reduced Equivalent Width plots for TO 35. The top panel is plotted including all measured Fe I lines. The bottom panel shows the resulting plot when problematic Fe I lines have been removed.

Fe Balance

Computing the Fe I and Fe II Abundances

Once the correlation between EP and log(REW) is reduced by removing problematic Fe I lines from the line list, an Fe abundance must be inferred for each remaining Fe I line in the list. This was accomplished by using the "abfind" driver of a line analysis and spectrum synthesis code, MOOG[2] (Sneden et al., 2012a). This driver utilizes a curve-of-growth technique to force-fit an abundance value to the supplied single-line Fe I equivalent width measurements. The curve-of-growth technique will be discussed in further detail in §5.1.2, but simply put, for a given spectral line, MOOG calculates the number of absorbers that would be required to generate a spectral line with the equivalent width supplied by the user. The abundance reported by MOOG is a logarithmic number abundance value, relative to hydrogen, where the logarithm of the number abundance of hydrogen relative to the total number of atoms and ions has been set to 12.

[2]http://www.as.utexas.edu/ chris/moog.html

Recall that in a differential analysis, the ratio of the number abundance in the star to the number abundance in the sun is required. Therefore, the Fe abundance must also be computed for each line of interest in the sun. These solar Fe abundances were computed using the same technique described in the previous paragraph. Because the abundances reported by MOOG are logarithmic, one simply needs to take the difference between the reported stellar and solar number abundances calculated for each line. This yields the logarithmic stellar abundance of Fe with respect to hydrogen relative to the logarithmic solar abundance of Fe with respect to hydrogen, i.e. [Fe/H].

Abundances of the Fe II lines were determined in a similar fashion, however, it is noted that the EP-REW correlation was not considered for these lines. There were only eight measurable Fe II lines across all of the spectral regions observed and determining accurate statistical properties like correlations becomes quite challenging with the use of only eight data points. Nevertheless, the determination of an Fe abundance using only the Fe II lines provides a crucial tool for determining an accurate value of $\log(g)$ as will be shown in §5.1.3.

Adjusting Stellar Atmosphere Parameters

On each pass of the iterative Fe balancing process, abundances were determined for each Fe I and Fe II line. From these individual line abundance values, a mean Fe abundance value was computed using only the Fe I values and a mean Fe abundance value was computed using only the Fe II values. Additionally, the standard deviations associated with those means were determined. If any line appeared to be deviant ($> 2\sigma$ from the mean), it was checked and either re-measured or removed from the line list, and then new Fe abundances were determined. Three relationships were considered regarding the Fe I and Fe II abundances: 1) the correlation between the Fe I abundances inferred from the lines and the EP of the lines (associated with the excitation balance) 2) the correlation between the Fe I abundances inferred from the lines and the REW of the lines (associated with the equivalent width balance) and 3) the difference between the calculated mean Fe I and Fe II abundances (associated with the abundance balance). To remove the correlations and to remove any difference between the mean abundances of Fe I and Fe II, the stellar atmosphere parameters must be adjusted and new abundances derived. Adjusting any particular parameter will have an effect on all three of the relationships listed above, however, each parameter tends to have one relationship that it affects the most. These effects will be covered in more detail in the following sections, however a summary is provided here. If there exists an Fe I-EP correlation, adjusting $T_{\rm eff}$ will have the greatest effect on that correlation. If an Fe I-REW correlation exists, adjusting the $\xi_{\rm t}$

will have the greatest effect. Lastly, if there exists a discrepancy between Fe I and Fe II, adjusting $\log(g)$ will have the greatest effect on removing that discrepancy. The plots used to determine the correlations are illustrated in Figure 5.2. The plots shown were generated for SG 17 after the final iteration of the process summarized above. At the stage illustrated in the plot, both of the correlations and the Fe I–Fe II discrepancy from the stellar atmosphere model had been minimized and a final set of stellar atmosphere parameters has been determined for the star.

The following sections will describe in detail the significance of the three main components of balancing the Fe abundances: the excitation balance, the equivalent width balance, and the abundance balance.

5.1.1 Excitation Balance

In an emission line spectrum generated in the lab, each line corresponds to a specific atomic transition in an atom of a particular element. The same is true of absorption lines in stellar spectra, though the picture is complicated by the presence of a multitude of chemical species, broadening effects, and the blending of neighboring lines. In most cases, however, a specific absorption line corresponds to a specific atomic transition that is associated with a particular amount of energy required for the excitation of an electron or emitted in the de-excitation of an electron. For a particular element, say Fe, there are many atomic transitions available to the electrons in the atoms, thus, there are many absorption lines associate with Fe.

If a star is in thermodynamic equilibrium, the atoms of Fe should obey a Maxwell-Boltzmann distribution, i.e., the number of Fe atoms in an excited state is given by the Boltzmann formula:

$$\frac{\mathrm{N_n}}{\mathrm{N_o}} = \frac{\mathrm{g_n}}{\mathrm{g_o}} \mathrm{e}^{-\chi_\mathrm{n}/\mathrm{kT}} \tag{5.3}$$

where $\mathrm{N_n}$ is the number of Fe atoms in the nth excited state, $\mathrm{N_o}$ is the number of Fe atoms in the ground state, $\mathrm{g_n}$ and $\mathrm{g_o}$ are the degeneracies of the nth and ground states respectively, χ_n is the difference in the excitation potential of the nth excited state and the ground state, k is the Boltzmann constant and T is the temperature of the atmosphere. Consider a "true" value of $\mathrm{N_1}$, the number of Fe atoms in the first excited state. According to the Boltzmann formula above, for a given temperature T, the value of $\mathrm{N_1}$ would require a specific value of $\mathrm{N_o}$. If the value of T in a model is lower than the true T, then the model value of $\mathrm{N_o}$ would have to be larger in order to

achieve the true value for N_1. Thus, the total abundance of Fe ($N_o + N_1$) would be overestimated by the model. The larger the value of the excitation potential associated with an excited state, the more pronounced this effect becomes. Therefore, for a model temperature that is lower than the true value, a positive correlation between the EP and and the Fe I abundance, [Fe I/H], will be seen. Conversely, if the temperature for the model is higher than the true value, there will be a negative correlation between the EP and the Fe I abundance. Therefore, the true temperature can theoretically be found by adjusting the model value of T_{eff} until the the correlation between the EP and [Fe I/H] has been eliminated. The top panel of Figure 5.2 shows the final plot for [Fe I/H] vs. EP for the star SG 17 where the majority of the correlation has been removed.

5.1.2 Equivalent Width Balance

Böhm-Vitense (1989) gives an in-depth description of the procedure for performing a curve-of-growth analysis in her book: *Introduction to Stellar Astrophysics Vol 2.* Sections of that procedure will be drawn upon for the purposes of explaining parts of the Fe balance technique, but keep in mind that Böhm-Vitense (1989) can be referenced for further details on the classical procedure of curve-of-growth analysis. In a general sense, a theoretical curve-of-growth yields information about how the equivalent width of a spectral line changes with the change in the number of absorbers associated with that particular line, i.e. the abundance of a particular element. The curve-of-growth is typically plotted according to the ordinate $\frac{EW_{\lambda_o}}{R_c \Delta\lambda_D}$ where EW_{λ_o} is the measured equivalent width of a spectral line at a measured central wavelength, λ_o, R_c is the limiting central line depth of the strongest lines of that element and $\Delta\lambda_D$ is the Doppler broadening associated with the spectral line. By determining a value for the ordinate and fitting that value to a point on the theoretical curve-of-growth, one can determine the abscissa value associated with the same point and in turn determine the number of absorbers associated with the ordinate value because the abscissa is a function of the number of absorbers, N_α.

Note that the Doppler broadening term actually contains three components: a thermal broadening component, a macroturbulent velocity component and a microturbulent velocity component. What is important here, as Böhm-Vitense (1989) explains, is that broadening due to macroturbulence (turbulent motions on scales larger than the mean free path of the photons) is not dependent on the number of absorbers in the atmosphere of a star, whereas the microturbulence (turbulent motions on scales smaller than the mean free path of the photons) is. This dependence

of the microturbulence, or microturbulent velocity (ξ_t), on the number of absorbers in the stellar material leads to a dependence of ξ_t on the equivalent width, and thus the reduced equivalent width (REW), of a spectral line.

To explain the potential correlation between the REW and the ξ_t, first re-consider the curve-of-growth in terms of the Doppler broadening term. The Doppler broadening term for a spectral line is given by:

$$\Delta\lambda_D = \lambda_o \frac{\xi_o}{c} \tag{5.4}$$

where λ_o is the rest wavelength of the spectral line, c is the speed of light and ξ_o is a reference velocity given by

$$\xi_o^2 = \xi_{th}^2 + \xi_{turb}^2 \tag{5.5}$$

In equation 5.5, ξ_{th} is the reference velocity component due to the thermal motions and ξ_{turb} is the reference velocity component due to the turbulent motions (both macro- and microturbulent). However, because the macroturbulent velocity component of $\Delta\lambda_D$ is not dependent on the number of absorbers, whereas the microturbulent component is, only the microturbulence will be considered when referring to ξ_{turb} for the remainder of this discussion.

Recall that the ordinate for the curve-of-growth analysis is defined by $\frac{EW_{\lambda_o}}{R_c \Delta\lambda_D}$. It can now be seen that the ordinate is inversely proportional to the ξ_t through $\Delta\lambda_D$ (equations 5.6 and 5.5). In this case, consider a true value for the number of absorbers, N_α, associated with a particular spectral line. If the model value of ξ_t is underestimated in the curve-of-growth analysis, then the ordinate computed for the spectral line will be overestimated. The point corresponding to this ordinate on the curve-of-growth will then lead one to determine an abscissa value, and thus N_α, that is too large, because the curve-of-growth is a monotonically increasing function. Thus, an underestimation of the model's ξ_t, will lead to an overestimation of N_α. The amount by which N_α is overestimated is dependent on the true number of absorbers that are present in the atmosphere. This is because as the number of absorbers increases to the point where a spectral line is no longer strictly optically thin, the curve-of-growth flattens out. If the spectral line being measured resides in the flat part of the curve-of-growth and the microturbulence is underestimated, then the point on the curve-of-growth that matches the computed ordinate will likely be found all the way up on the damping section of the curve-of-growth. Therefore, the more absorbers that are truly present in the atmosphere, the larger the overestimation of N_α will be.

The connection to the reduced equivalent width can be made by first writing the ordinate in terms of the rest wavelength of the line and the reference velocity ξ_o:

$$\frac{\mathrm{EW}_{\lambda_o}}{\mathrm{R_c}\Delta\lambda_\mathrm{D}} = \frac{\mathrm{EW}_{\lambda_o}}{\mathrm{R_c}\lambda_o\frac{\xi_o}{c}} \tag{5.6}$$

and then re-writing this equation as:

$$\frac{\mathrm{EW}_{\lambda_o}}{\mathrm{R_c}\Delta\lambda_\mathrm{D}} = \frac{\mathrm{EW}_{\lambda_o}}{\lambda_o}\frac{c}{\mathrm{R_c}\,\xi_o} \tag{5.7}$$

where $\frac{\mathrm{EW}_{\lambda_o}}{\lambda_o}$ is the definition of the reduced equivalent width (REW).

The potential correlation between the ξ_t and the REW can now be understood through the following explanation. Consider a single model value of ξ_t that is an underestimation of the true value of ξ_t. It has already been explained how this underestimation will cause an overestimation in the computation of the ordinate, and thus the abundance, for a specific spectral line. It can now be seen from equation 5.7, that for a given underestimation of ξ_t, the larger the REW is for the spectral line in question, the larger the overestimation of the ordinate, and thus abundance, will be for that line. Thus, for a underestimation of the model ξ_t, a positive correlation between the REWs and the Fe abundances will be seen. Conversely, if the model ξ_t is overestimated, there will be a negative correlation between REWs and the Fe abundances that are computed. This relationship can be exploited in much the same way that the T_{eff}-EP relationship was exploited in the previous section. The true microturbulence can theoretically be found by adjusting the model value of ξ_t until the the correlation between the REW and [Fe I/H] has been eliminated. The bottom panel of Figure 5.2 shows the final plot for [Fe I/H] vs. REW for the star SG 17 where the majority of the correlation has been removed.

5.1.3 Ionization Balance

MOOG reports an abundance value that accounts for every atom of a particular element, regardless of each individual atom's excitation, ionization, etc. Ideally, the abundance that MOOG calculates for Fe should be the same regardless of whether MOOG uses lines of neutral Fe or lines of singly ionized Fe in its calculations. This presents one with the opportunity to determine an accurate value of the surface gravity, $\log(g)$, for a stellar atmosphere model. This is possible because

singly ionized Fe is more sensitive to surface gravity than neutral Fe particularly for stars in the temperature range of the stars studied in the current work. Thus, an accurate value for $\log(g)$ can be determined by matching the Fe abundance calculated via Fe II lines to the Fe abundance calculated via Fe I lines.

To fully understand why this technique works, one has to understand why Fe II is more sensitive to the surface gravity than Fe I. The key is that in cool (F, G and K spectral type) stars, like those studied in the present abundance analysis, the continuous absorption coefficient is due mostly to the presence of H^- and the majority of Fe in these stars is in the form of Fe II according to the Saha equation (5.8) which tells us about the ionization state for a collision-dominated gas (Gray, 2005). This equation is given by:

$$\frac{N_I}{N}P_e = \frac{(2\pi m_e)^{3/2}(kT)^{5/2}}{h^3}\frac{2u_I(T)}{u(T)}e^{-\chi_I/kT} \tag{5.8}$$

where N_I is the number of singly ionized atoms, N is the number of neutral atoms, P_e is the electron pressure, m_e is the mass of an electron, k is the Boltzmann constant, T is the temperature, u_I is the partition function for the ionized atoms, u is the partition function for the neutral atoms and χ_I is the energy required to ionize a neutral atom. This equation can be altered to represent the ratio between any two adjacent ionization states, for example one could consider the ratio of Fe IV to Fe III, by letting χ_I represent the energy it would take to remove an electron from an atom of Fe III.

The Saha equation also indicates that if the surface gravity is increased, and thus the electron density and pressure, the number of H^- ions which have an additional electron, will increase relative to the number of neutral hydrogen atoms (Böhm-Vitense, 1989). Because the continuous absorption in these stars is due mainly to the presence of H^-, if the surface gravities are low, like in the case of the giant stars, the ratio of H^- to H is low and thus the continuous absorption is weak. This may cause the absorption lines to appear stronger in a giant star than they would appear in a dwarf star. Note, however, that the difference in the observed line strength, or equivalent width, would be due to differences in surface gravity, not differences in the abundance of the element in question.

The stars involved in the present study are relatively cool, as previously mentioned and solar-like in chemical composition. Thus, the majority of the Fe in these stars is in the form of Fe II. Consider a star with a given value of $\log(g)$. If that value is now decreased, the ratio of H^- to H is

also decreased, which in turn decreases the continuous opacity of the atmosphere. This effectively increases the geometrical depth of the photosphere and, in turn, the amount of Fe (mostly in the form of Fe II) above the photosphere. This means the amount of absorption that is observed due to Fe II compared to the continuous absorption will increase. Consider a stellar model that has been generated to synthesize an Fe II line to be compared to an observed Fe II line in a star. If the value of $\log(g)$ has been underestimated, the model line will require an Fe abundance smaller than the true Fe abundance of the star to generate an Fe II line with the same strength of the observed Fe II line. This is because the model with a low value of $\log(g)$ will generate stronger lines for lower abundances.

In the ionization balance, for a set of stellar atmosphere parameters, a mean Fe abundance is inferred using only the Fe I lines and then is inferred again using only the Fe II lines. If the Fe abundance inferred from Fe I does not match that inferred from Fe II, the value of $\log(g)$ is adjusted until the Fe abundances computed in both ways match. In particular, if the Fe II abundance value is lower than the Fe I abundance value, $\log(g)$ must be increased so that the strength of the Fe II lines generated by the model are smaller and require a larger Fe abundance to match the Fe II lines observed.

5.1.4 Final Stellar Atmosphere Parameters

It should be reiterated that any change of a single stellar atmosphere parameter value, in practice, affects *all* of the balances described above, however, the most prominent effects were discussed in each section. The stellar atmosphere parameters were, therefore, adjusted individually in an iterative manner to converge on a unique set of stellar atmosphere parameters for each star. In other words, on each pass, one stellar atmosphere parameter would be adjusted, new abundances would be determined, the balances would be checked, the next appropriate stellar atmosphere parameter adjustement would be estimated and the process would be repeated. A unique solution to this iterative process was accepted when, for a given star, the correlation coefficient of a least squares fit was < 0.01 in both the [Fe I/H]–EP data and the [Fe I/H]–REW data, and when the difference between the [Fe I/H] and the [Fe II/H] values was < 0.01 dex. The stellar parameters extracted in this way for each target are listed with uncertainties in Table 5.1. The computation of the uncertainties for each parameter will be discussed in §5.1.4.1.

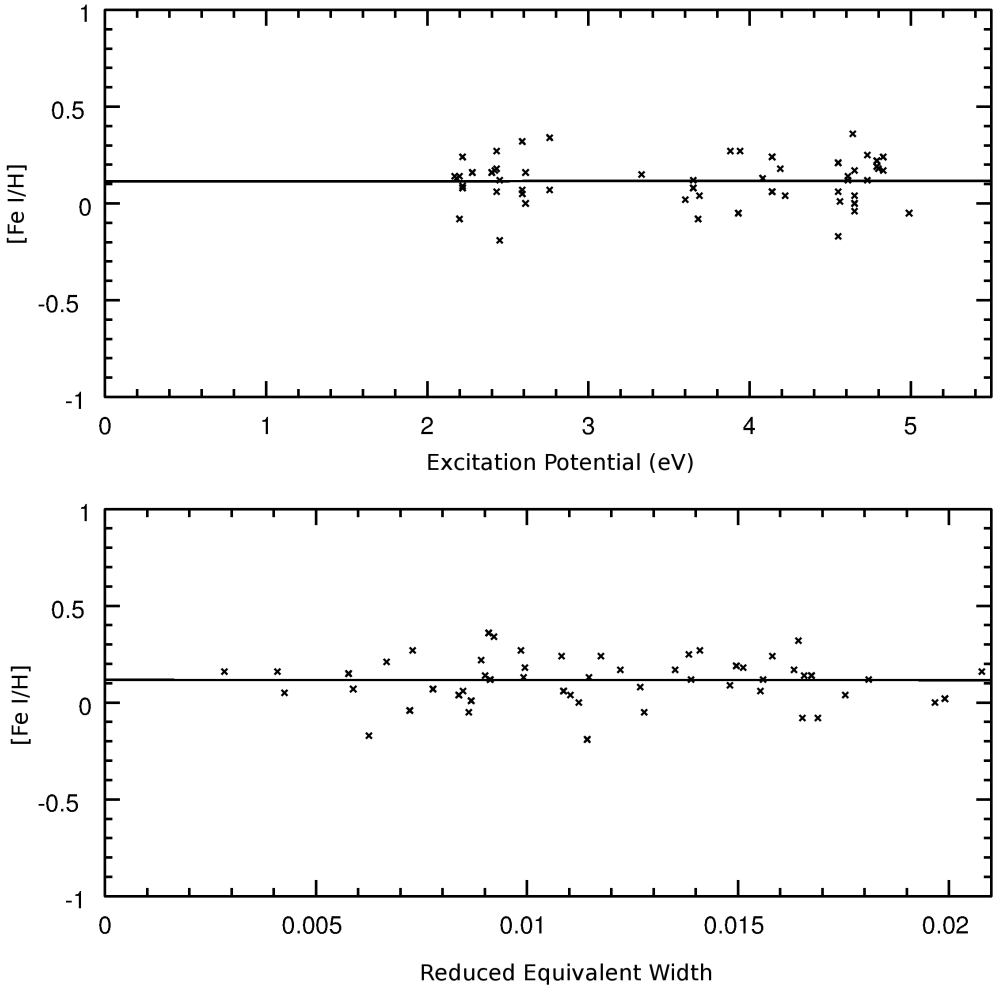

Figure 5.2: Fe Balance Plots for SG17.

Table 5.1. Final Stellar Atmosphere Model Parameters

Star	$T_{\rm eff}$ (K)	$\log(g)$	[Fe I/H]	$\xi_{\rm t}$ (km/s)
SG 16	5210 ± 106	$3.79\ ^{+0.48}_{-0.66}$	$0.13\ ^{+0.10}_{-0.10}$	1.68 ± 0.21
SG 17	5755 ± 90	$3.88\ ^{+0.32}_{-0.82}$	$0.12\ ^{+0.09}_{-0.09}$	1.45 ± 0.11
SG 20	5245 ± 79	$3.82\ ^{+0.46}_{-0.85}$	$0.12\ ^{+0.08}_{-0.07}$	1.41 ± 0.17
SG 21	5220 ± 104	$3.74\ ^{+0.45}_{-1.06}$	$0.14\ ^{+0.11}_{-0.11}$	1.54 ± 0.23
SG 25	5430 ± 83	$3.79\ ^{+0.38}_{-0.59}$	$0.22\ ^{+0.09}_{-0.08}$	1.52 ± 0.16
SG 26	5945 ± 92	$3.68\ ^{+0.37}_{-0.69}$	$0.07\ ^{+0.08}_{-0.09}$	1.39 ± 0.10
SG 33	6170 ± 137	$4.20\ ^{+0.42}_{-1.05}$	$0.17\ ^{+0.11}_{-0.13}$	1.63 ± 0.16
SG 36	6025 ± 98	$3.90\ ^{+0.31}_{-0.87}$	$0.18\ ^{+0.09}_{-0.10}$	1.40 ± 0.11
RG 22	5150 ± 92	$3.52\ ^{+0.57}_{-1.11}$	$0.15\ ^{+0.10}_{-0.09}$	1.66 ± 0.16
RG 41	4850 ± 85	$2.60\ ^{+0.69}_{-1.20}$	$-0.13\ ^{+0.10}_{-0.12}$	2.10 ± 0.12
TO 35	6270 ± 100	$4.15\ ^{+0.41}_{-0.65}$	$0.18\ ^{+0.08}_{-0.09}$	1.68 ± 0.11
TO 37	6145 ± 105	$4.04\ ^{+0.31}_{-0.73}$	$0.11\ ^{+0.08}_{-0.10}$	1.56 ± 0.12
TO 0	6155 ± 102	$4.00\ ^{+0.25}_{-0.67}$	$0.13\ ^{+0.08}_{-0.09}$	1.52 ± 0.10
TO 49	6210 ± 107	$3.89\ ^{+0.37}_{-0.66}$	$0.03\ ^{+0.09}_{-0.09}$	1.74 ± 0.13
YS 13	5950 ± 86	$4.17\ ^{+0.33}_{-0.93}$	$-0.28\ ^{+0.07}_{-0.09}$	1.47 ± 0.13
YS 23	6110 ± 75	$4.71\ ^{+0.28}_{-0.66}$	$0.12\ ^{+0.06}_{-0.08}$	1.57 ± 0.12
YS 24	5965 ± 101	$4.09\ ^{+0.33}_{-0.92}$	$-0.22\ ^{+0.08}_{-0.09}$	1.47 ± 0.14
YS 42	5790 ± 84	$3.41\ ^{+0.35}_{-0.90}$	$-0.14\ ^{+0.07}_{-0.08}$	2.28 ± 0.15
YS 43	5265 ± 79	$3.42\ ^{+0.34}_{-0.87}$	$-0.08\ ^{+0.08}_{-0.08}$	2.03 ± 0.14
YS 44	5050 ± 88	$2.81\ ^{+0.50}_{-0.79}$	$-0.22\ ^{+0.09}_{-0.09}$	2.33 ± 0.18
YS 45	5945 ± 77	$4.14\ ^{+0.24}_{-0.53}$	$-0.11\ ^{+0.06}_{-0.07}$	1.30 ± 0.12
YS 46	5615 ± 147	$4.24\ ^{+0.58}_{-1.22}$	$-0.27\ ^{+0.11}_{-0.12}$	2.48 ± 0.42
YS 47	5610 ± 98	$4.02\ ^{+0.32}_{-0.88}$	$-0.05\ ^{+0.08}_{-0.09}$	1.57 ± 0.18
YS 48	5415 ± 88	$4.48\ ^{+0.25}_{-0.90}$	$-0.02\ ^{+0.08}_{-0.07}$	1.86 ± 0.23

Note that in the case of YS 46, there were two resolvable components in the spectra. The Fe balance was attempted for the fainter component of this SB2, however the parameters would not converge on a unique solution. This is not surprising because the values measured for the equivalent widths of the Fe I and Fe II are likely overestimates due to contamination from the primary companion's spectrum. In fact, it is likely that many of the equivalent width measurements of the primary companion are overestimates. Nevertheless, the results have been included in the current abundance analysis.

5.1.4.1 Uncertainties in Stellar Atmosphere Parameters

Due to the differing nature of the stellar atmosphere parameters, the uncertainties associated with the various parameters were calculated in different ways. The following paragraphs summarize the techniques used to determine the uncertainty for each stellar atmosphere parameter. The notation to denote uncertainties will be of the form σ_{X} where X represents the stellar atmosphere parameter in question.

$\mathbf{T_{eff}}$ and $\xi_{\mathbf{t}}$

Initial upper and lower bounds of the uncertainties for T_{eff} and ξ_{t} were calculated individually for each star, but each calculations follow the same procedure. Recall that the final value for T_{eff} was determined by removing the correlation between EP and [Fe I/H] and the value for ξ_{t} was determined by removing the correlation between REW and [Fe I/H]. Thus, for a set of parameters, e.g. EP and [Fe I/H], the limits of a (small) range of values can be determined for for the associated stellar atmosphere parameter, in this case T_{eff}, for which the correlation between EP and [Fe I/H] is statistically insignificant. By determining the point at which the correlation computed between EP and [Fe I/H] becomes statistically significant, we determine the uncertainty associated with T_{eff}. To illustrate the process used to determine the upper and lower bounds on the uncertainties, the determination of the upper bound on $\sigma_{\mathrm{up},T_{\mathrm{eff}}}$ for one star will be discussed.

Once the stellar model atmosphere parameters had been determined using a process that rendered no correlation between EP and [Fe/H], the value of T_{eff} was increased incrementally in an iterative process until a statistically significant correlation developed. On each pass, T_{eff} was increased, a new stellar atmosphere model was generated and a new [Fe I/H] abundance was determined for each Fe I line. A Pearson correlation coefficient was determined to interpret the correlation

between [Fe I/H] and EP for the Fe I lines according to Equation 5.9.

$$r = \frac{\sum ep_i \cdot fe_i - \frac{\sum ep_i \cdot \sum fe_i}{n}}{\sqrt{(\sum ep_i^2 - \frac{(\sum ep_i)^2}{n})(\sum fe_i^2 - \frac{(\sum fe_i)^2}{n})}} \tag{5.9}$$

Each sum above runs from i to n, the number of Fe I lines measured, ep_i represents the excitation potentials of the lines, and fe_i represents the abundances calculated for the lines.

To investigate the statistical significance of of the correlation coefficient, a t-test statistic was computed. The choice of a t-test statistic is appropriate because for sample sizes with $n > 30$, the probability distribution associated with the correlation coefficient, r, can be approximated by a Student's t distribution. The t-test statistic, or t-value associated with the correlation coefficient, r, was calculated following Equation 5.10.

$$t = r \cdot \sqrt{\frac{n-2}{1-r^2}} \tag{5.10}$$

The null hypothesis for this scenario is that there is no correlation ($r = 0$) between EP and [Fe I/H], but upon each iteration, T_{eff} is purposefully increased, causing r, and thus t, to be driven further and further from zero. For each iteration, the error function was used to calculate a p-value corresponding to the t-test statistic calculated; for a given t-value, the p-value estimated the likelihood that determining a t-value at least as extreme as the current value is due to chance, i.e. it represents the probability that there is no correlation between EP and [Fe I/H]. This process was repeated until a p-value < 0.33 was attained, indicative of a 1σ statistically significant correlation between EP and [Fe I/H]. The value for T_{eff} on the last iteration of the process described is considered the upper limit of the uncertainty for the star in question. A lower bound for T_{eff} was determined by decreasing the value of T_{eff} until a statistically significant correlation between EP and [Fe I/H] developed. The final uncertainty reported for T_{eff} in Table 5.1, denoted by $\sigma_{T_{eff}}$ was determined by using:

$$\sigma_{T_{eff}} = \frac{\sigma_{up,T_{eff}} - \sigma_{low,T_{eff}}}{2} \tag{5.11}$$

A final uncertainty was similarly computed for ξ_t, denoted by σ_{ξ_t}, by determining upper and lower bounds via the procedure detailed above and executing Equation 5.11. However, the correlation being exploited to determine this uncertainty was the one between ξ_t and REW.

[Fe I/H] and [Fe II/H]

The Fe abundance is determined by using the measurements of the equivalent widths of either Fe I (or Fe II lines) and stellar atmosphere structures extracted from the Kurucz (1992) grid using the three stellar parameters $T_{\rm eff}$, $\xi_{\rm t}$ and $\log(g)$. Therefore, the uncertainty associated with the Fe abundance inferred using Fe I lines, $\sigma_{\rm FeI}$, is dependent not only on the uncertainty in the measurement of the equivalent widths of the Fe I lines, $\sigma_{\rm meas,FeI}$, but also on the uncertainties associated with the stellar atmosphere parameters: $\sigma_{\rm T_{eff}}$, $\sigma_{\xi_{\rm t}}$ and $\sigma_{\log(g)}$. In particular, $\sigma_{\rm FeI}$ is co-dependent with $\sigma_{\log}(g)$, thus they have to be computed in an iterative process. The first step of this process is an initial computation of both $\sigma_{\rm FeI}$ and of $\sigma_{\rm FeII}$. This initial computation will be outlined for Fe I below, but note that the initial computation of $\sigma_{\rm FeII}$ is performed in an identical manner.

The initial total uncertainty in [Fe I/H] is calculated using Equation 5.12:

$$\sigma_{\rm FeI} = \sqrt{(\frac{\partial[\text{Fe I/H}]}{\partial \rm T_{eff}} \cdot \sigma_{\rm T_{eff}})^2 + (\frac{\partial[\text{Fe I/H}]}{\partial \log(g)} \cdot \sigma_{\log(g)})^2 + (\frac{\partial[\text{Fe I/H}]}{\partial \xi_{\rm t}} \cdot \sigma_{\xi_{\rm t}})^2 + (\sigma_{\mu,\rm FeI})^2} \tag{5.12}$$

In this equation, each $\frac{\partial \text{Fe I}}{\partial \text{X}}$ term represents what will be referred to as a "sensitivity." These sensitivities indicate the rate of change in the abundance value of Fe with a stellar atmosphere parameter indicated by 'X.' Iron sensitivities were computed for each stellar atmosphere parameter for each star. For a given star and sensitivity, this was accomplished by starting with the derived stellar atmosphere parameters found in Table 5.1, altering only the stellar atmosphere parameter in question, generating a new stellar atmosphere model and computing the new Fe abundance for that model. The sensitivity of Fe to the parameter in question was then computed by dividing the amount of change in the Fe abundance, ∂Fe I, by the amount of change in the parameter X, ∂X. The sensitivities computed for each stellar atmosphere parameter for each star can be found in Table 1 in Appendix C.

The uncertainties $\sigma_{\rm T_{eff}}$ and $\sigma_{\xi_{\rm t}}$ were calculated as described in "**$T_{\rm eff}$ and $\xi_{\rm t}$**" and $\sigma_{\mu,\rm FeI}$, the uncertainty, or standard error associated with the equivalent width measurements, was determined in the same way that the standard error was computed for the radial velocity measurements in §4.3. The standard error is given by the following equation:

$$\sigma_{\mu,\rm FeI} = \frac{\sigma_{\rm meas,FeI}}{\sqrt{\rm n-1}} \tag{5.13}$$

where $\sigma_{\mathrm{meas,FeI}}$ is the sample standard deviation given by:

$$\sigma_{\mathrm{meas,FeI}} = \sqrt{\frac{1}{\mathrm{n}-1}\sum_{\mathrm{i}=1}^{\mathrm{n}}(\mathrm{FeI_i} - \overline{\mathrm{FeI}})^2} \tag{5.14}$$

Again, n is the number of Fe I lines measured, $\mathrm{FeI_i}$ is the Fe I abundance computed for each individual line and $\overline{\mathrm{FeI}}$ is the mean value of those individual Fe I abundances. In the initial computation of the uncertainty in Fe I, σ_{FeI}, the value of the uncertainty in $\log(g)$ was taken to be zero. The initial uncertainty in Fe II, σ_{FeII}, was also computed using the process described above.

log(g)

Recall that a value of $\log(g)$ was accepted for a stellar atmosphere model when the Fe abundance calculated using Fe I lines was balanced with the Fe abundance calculated using Fe II lines, i.e., when [Fe I/H] = [Fe II/H] to within 0.01 dex. Note that the uncertainty in the difference between [Fe II/H] and [Fe I/H] is given by:

$$\sigma_{\mathrm{II-I}} = \sqrt{\sigma^2_{\mathrm{FeII}} + \sigma^2_{\mathrm{FeI}}} \tag{5.15}$$

Thus, the uncertainty in $\log(g)$, $\sigma_{\log(g)}$, can be computed by altering the value of $\log(g)$ for a stellar atmosphere model enough so that the difference between the values computed for [Fe I/H] and [Fe II/H] is equal to the sum of the Fe I and Fe II uncertainties in quadrature, i.e. σ_{II-I}. This can be accomplished by either increasing or decreasing the value of $\log(g)$, but the results are not necessarily the same for both cases.

It can now be seen that the uncertainties associated with [Fe I/H] and [Fe II/H] are dependent on the uncertainty associated with $\log(g)$ as shown in Equation 5.12, and the uncertainty in $\log(g)$ is dependent on the uncertainties in [Fe I/H] and [Fe II/H]. Therefore, these uncertainties were computed in an iterative process.

As previously mentioned, on the first iteration, $\sigma_{\log(g)}$ was taken to be zero, and σ_{FeI} and σ_{FeII} were computed. These values were used to compute $\sigma_{\mathrm{II-I}}$, which was then used to determine a value for $\sigma_{\log(g)}$ as described above. The new value of $\sigma_{\log(g)}$ was then incorporated into new σ_{FeI} and σ_{FeII} values from which a new $\sigma_{\mathrm{II-I}}$ was computed. The new value was then compared with the old value. This process was repeated three times for each star, after which, 85% of the sample stars possessed a new $\sigma_{\mathrm{II-I}}$ that was different than the old value by $\leq$ 0.03dex. This process was

performed for two instances–one where the value of $\log(g)$ was increased and one where the value of $\log(g)$ was decreased to determine respective upper and lower bounds on $\log(g)$ for which $\sigma_{\mathrm{II-I}}$ converged.

5.2 Other Elements of Interest

The elements of interest in this study included the Fe peak elements (Fe, Ni, Cr), α-capture elements (Ti, Ca, Si, O), n-capture elements (Ba, Y) and others (Al). Attempts were made to determine abundances for additional elements such as Zr, Sr, Pb and Eu, however the limits of the spectral resolution of the observations prevented this task from being accomplished. Line lists were comprised for each element from various studies including Bubar & King (2010), Preston & Sneden (2000), King et al. (1998) and Sneden et al. (2003). The equivalent widths of each measurable line in the line lists are reported in Tables 2, 3, 4 and 5 in Appendix C for all of the targets involved in the abundance analysis.

An abundance was inferred for each of the elemental lines in the line list of each star in the same way that the Fe abundance was inferred. A mean abundance was then computed from those lines for each element. For a given star, the stellar atmosphere structure was established by interpolating from the Kurucz (1992) grid for the final values of the stellar atmosphere parameters and the measured equivalent widths of lines of each element of interest served as inputs in MOOG for a curve-of-growth analysis to determine the abundance value for each element. The mean abundance values and corresponding uncertainties for each element are reported for all of the targets in Tables 6, 7, 8 and 9 in the Appendix C.

The uncertainties for each element were computed for each star using Equation 5.12 substituting the element in question for Fe. For a given star, the uncertainties for the stellar atmosphere parameters $\sigma_{\mathrm{T_{eff}}}$, $\sigma_{\log}(g)$ and $\sigma_{\xi_{\mathrm{t}}}$ were determined in the procedure described in §5.1.4.1. However the uncertainty in the measurements of the equivalent widths of the lines and the sensitivities to the different stellar parameters will be different for each element.

For each element, the uncertainty in the measurements of the equivalent widths of the lines was computed using Equations 5.14 and 5.13, replacing Fe with the element in question. In the case where there was only one line to measure, the standard error was taken to be the sample standard deviation calculated for the Fe I lines for that star since the sample standard deviation tells the user

that if another EW measurement is made, there is an associated 1σ confidence that the measurement will be within $\pm\sigma_{\mathrm{meas,X}}$ of the mean value of the EWs for the element X. In other words, it informs the user of the precision of the measurement of a single line.

The sensitivities for each element were computed for five stars chosen primarily by their locations on the CMD, but also by the secondary requirement that they are not likely binary stars as indicated by their radial velocity p-values. These sensitivities were computed by both increasing and decreasing the parameter in question to determine how the elemental abundance changed with the change in the parameter. The sensitivities of each element to the three stellar parameters $\mathrm{T_{eff}}$, $\log(g)$ and ξ_{t} are listed in Table 1 in the Appendix C for the turnoff star, TO 37, a subgiant from the center of the SG branch, SG 17, a subgiant from the region at the base of the red giant branch, SG 16, the red giant star, RG 41 and a yellow straggler, YS 42. The sensitivities for these five "standard sensitivity" stars were then used as approximations for the other stars. The sensitivities assigned to a particular star were adopted from the standard sensitivity star that was located closest to it in the CMD.

Chapter 6

Discussion

6.1 Radial Velocities

The primary finding of the current radial velocity survey is that only two of the YSs targets exhibit constant radial velocities (see Table 4.1) suggesting that they either single stars, or that if they do exist in binary systems, the system is seen face-on from earth. Specifically, YS 24 exhibits a radial velocity that is constant to 2σ and YS 48 exhibits a radial velocity that is constant to 3σ. The finding that the majority of the YSs exhibit variable radial velocities is encouraging when one considers a mass transfer hypothesis for YSs because it reveals a high binary frequency among the YS population. However, other factors need to be considered. Primarily, the specific radial velocity values exhibited by the YSs need to be examined with regard to the bulk motion of the cluster. Mathieu (1983) determined a mean radial velocity of 33.5 ± 0.5 km/s for M67. Half of the YSs studied presently exhibit mean radial velocity values that are significantly different than the mean cluster radial velocity value derived by Mathieu (1983). However, a radial velocity distribution for M67 can be used to further investigate the YS radial velocities.

To this end, smoothed histograms were created to consider the extent to which radial velocity data vary for likely cluster members in both the Mathieu et al. (1986) and Yadav et al. (2008) works. Figure 6.1 shows the smoothed histogram for the Mathieu et al. (1986) radial velocity data (solid line) and the smoothed histogram for the Yadav et al. (2008) data (dotted line). These histograms were computed by assuming a Gaussian distribution of the radial velocity values for each star in each study and summing those distributions for a range of heliocentric radial velocity values with a

specified bin size. It is important to note that because Mathieu et al. (1986) reported the standard deviation of the multiple radial velocity measurements made for each star, those values were used in computing the Gaussian distribution for each star. Yadav et al. (2008), however, reported formal fitting errors produced from their cross correlation pipeline, so upon their suggestion, the fitting errors were added in quadrature to their reported upper systematic uncertainty ($\sim$ 0.6km/s) to estimate true radial velocity uncertainties (see Table 4.1 for explicit values). These uncertainty estimates were then used for the purpose of producing a Gaussian distribution for the radial velocity value for each star in the Yadav et al. (2008) study. Stars that were reported by Mathieu et al. (1986) to be spectroscopic binaries were removed from the Mathieu et al. (1986) sample to compute the histogram, as were stars that possessed membership probabilities $< 50\%$ (Sanders, 1977). Similarly, stars that were reported by Yadav et al. (2008) to have membership probabilities $< 50\%$ were removed from the Yadav et al. (2008) sample to compute the histogram. Unfortunately, Yadav et al. (2008) made no report on suspected spectroscopic binaries, so those stars could not be removed from the sample.

In addition to the smoothed histograms, the radial velocities of the individual stars considered in the current abundance analysis have been plotted according to their mean heliocentric radial velocity values. These radial velocity data have been plotted with a vertical offset so that they can all be seen. The "normal" SG and TO stars (barring SG 33 because it was determined that this star was a spectroscopic binary) have been plotted without error bars because their uncertainties were typically smaller than the size of the data point on the plot. The YSs have been plotted with error bars and labels. The circled YSs, 24 and 48, are the two YSs for which the radial velocities were found to be constant at 2σ and 3σ levels respectively. It is plain to see in this figure that the normal stars' radial velocity determinations fall cleanly within the main distribution peak of both histograms indicating that the radial velocities of these normal stars agree with the overall motion of the cluster. The picture for the YSs, however, is more complicated.

The discrepancies seen between the overall cluster motion and the radial velocities exhibited by the YSs could be used to argue that the YSs are simply contaminating field stars, however, there are a few issues with assuming this explanation for all YSs. First, it should be recalled that for the stars that exhibit variable radial velocities, the values reported presently are simply a calculated mean of the radial velocities observed and will vary over time; they are not systemic radial velocities of the binary system. Second, the radial velocities for YSs 23, 24, 42, 43 and 44 are not entirely

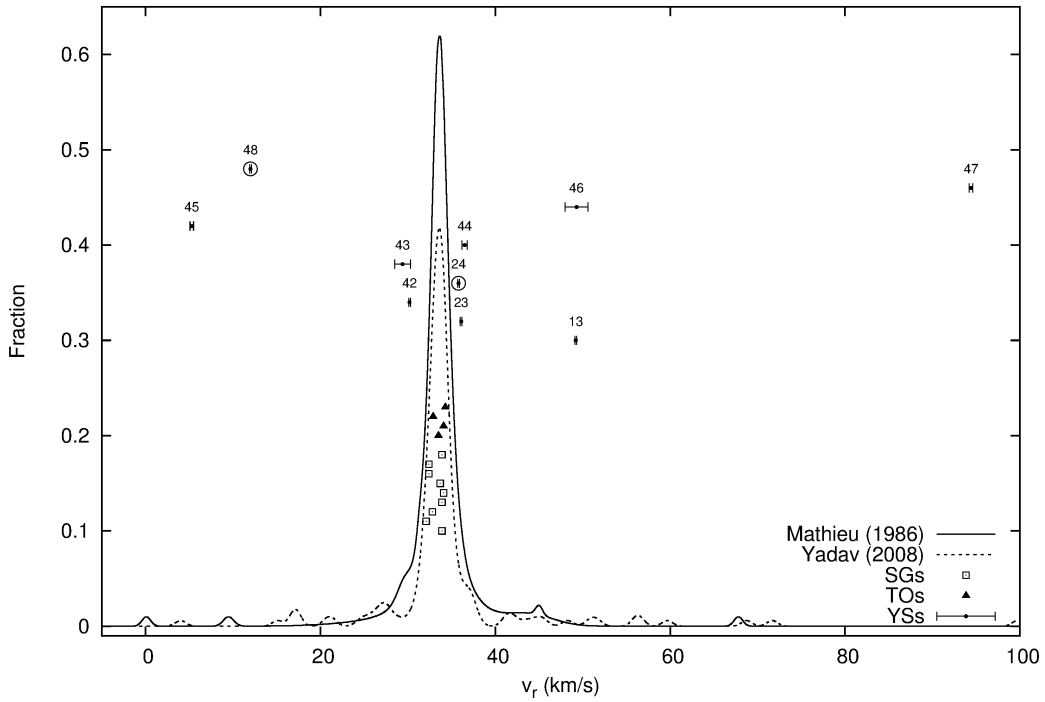

Figure 6.1: Radial velocity histograms for Mathieu et al. (1986) (solid line) and Yadav et al. (2008) (dotted line). The stars observed in the current abundance analysis are plotted here according to their mean radial velocity values with vertical offsets. The uncertainties associated with the SG and TO radial velocity values are smaller than the size of the points on the plot and have therefore been left off. Uncertainties are reported, however, for the YSs which are labeled with their associated identification numbers from the current study. The two stars whose radial velocity points are circled mark the two YSs whose radial velocity values are constant at the 2σ and 3σ levels.

inconsistent with the cluster motion when the base of the main distribution peak is considered. Third, likely single star, M67 members exist in both the Mathieu et al. (1986) and Yadav et al. (2008) studies that exhibit radial velocities similar to YSs 13, 45, 46 and 48. Furthermore, if the YSs are considered as a single population of contaminating field stars, it requires that the field stars that just happen to fall within the YS region in the CMD of M67 also happen to have a particularly high binary frequency. It should also be noted that the work of others, as discussed in §1, has shown that the existence of BSs is likely due to some interaction between multiple stars and can result in binary systems. It has also been shown that binary systems can exhibit effects that are due to dynamical interactions, like mass segregation. This dissertation proposes that it is possible that at least some of the YSs may be related to the BSs in the sense that they may be evolved BSs. If this is the case, then YSs should also be subject to these types of dynamical interactions. If a BS or YS has suffered some sort of dynamical "kick" from the cluster, it could potentially exhibit a proper motion and/or radial velocity that disagrees with the cluster mean. In light of the current discussion, the radial velocity data alone is insufficient to rule a non-membership status for the YSs as a population and it is appropriate that all of the objects that could potentially be true YSs (as indicated by their locations in the CMD of M67) be studied as a population, temporarily disregarding their membership probabilities determined in proper motion studies. Then multiple factors like chemical abundances and stellar atmosphere parameters can be taken into account in addition to proper motions membership probabilities and radial velocities when making conclusions about each individual potential YS. Because multiple parameters need to be considered for each YS, the YSs are discussed in this way, on an individual basis in Appendix D.

6.1.1 A Note on Specific Radial Velocity Discrepancies with Yadav et al. (2008)

The results for the radial velocities of the stars studied in the current work exhibit substantial overlap with other studies and therefore provide an opportunity for radial velocity measurement comparisons. The results of two predominant radial velocity studies (Mathieu et al., 1986; Yadav et al., 2008) will be discussed here. Each of these studies contained radial velocity data for some of the objects observed in this work. Those data were presented in the Table 4.1. The radial velocity determinations in the present work agree with the Mathieu et al. (1986) study for all stars for which

Mathieu et al. (1986) data are available. However, discrepancies arise in comparisons with the Yadav et al. (2008) study. In particular, the radial velocities determined by Yadav et al. (2008) for BS 1, BS 2, BS 7, BS 8 and YS 24 are grossly discrepant with the values determined in the current study. It should be noted that the number of radial velocity measurements available for BS 1, BS 2 and BS 8 in the present study were limited and unfortunately, no Mathieu et al. (1986) data exists for these stars for further comparison. In the case of BS 7, the radial velocity data from the present study indicate that this star does not exhibit a constant radial velocity. Thus, it could be possible that this star is capable of exhibiting the Yadav et al. (2008) radial velocity value, but further observation would be necessary to establish whether or not this would be possible. The case of YS 24 is the most perplexing. The Yadav et al. (2008) radial velocity value is significantly different from the mean value determined in the current work. Furthermore, the 41 radial velocity measurements available for this star in the current study indicate that it exhibits a constant radial velocity at a 2σ level. It is noted that the primary purpose of the Mathieu et al. (1986) study of M67 was to determine radial velocities of M67 stars and that the radial velocities of the stars studied by Mathieu et al. (1986) were measured multiple times. Therefore, even though no Mathieu et al. (1986) data are available for YS 24 for further comparison, it is plausible that the radial velocities measured presently for YS 24 are accurate, when one considers the degree of agreement between the current work and the Mathieu et al. (1986) study for other stars.

6.2 Abundances

For stars of near solar metallicity, [Fe/H] is often used to approximate the "metallicity" of a star, or the overall "heavy" metal content. In astronomy terms, "heavy" means any element heavier than He. The metallicities, or [Fe/H] values, derived in this work indicate that the population of YSs are derived from a different parent population than the "normal" population of SG and TO stars, excluding SG 33. Figure 6.2 shows a smoothed histogram of the Fe I abundances calculated for both the YS and the normal star populations. These smoothed histograms were computed by assuming a Gaussian distribution of the [Fe I/H] values that were computed for each Fe I line for each star and summing those distributions for specified bins of [Fe I/H]. It can be seen in Figure 6.2 that there is a clear distinction between the peaks corresponding to each population, however there is some overlap in the distributions when the uncertainties are taken into account.

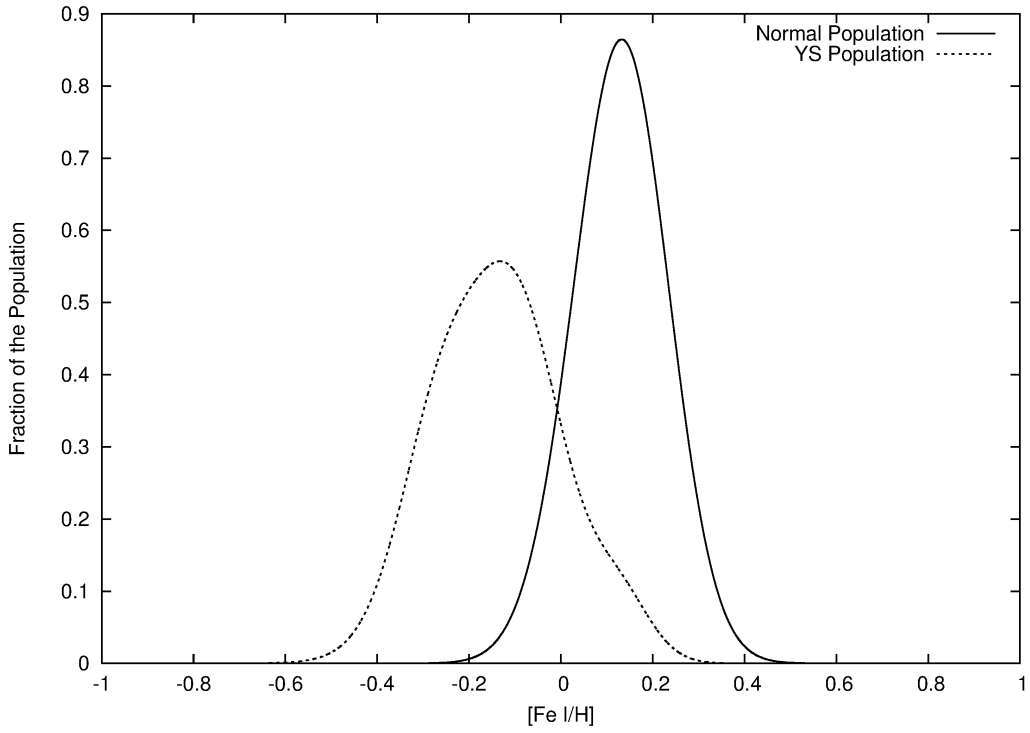

Figure 6.2: This plot shows smoothed histograms of the YS population and a "normal" star population that consists of the SGs and TOs, barring SG33 due to its radial velocity variation and likely binary nature. The two RGs were not used in the calculation of either smoothed histogram. The dashed line indicates the smoothed histogram computed for the YS population. The solid line corresponds to the normal star population.

The distinction between the two populations can also be seen in Figure 6.3, but here, the specific mean Fe I abundances for each star can be seen. In this figure, each star has been plotted according to its mean Fe I abundance and associated uncertainty, as computed using the previously described Fe balance approach. Because of this apparent distinction between the two populations, mean Fe I abundance values and their associated uncertainties were computed both for the normal star population (indicated by the solid line) and the YS population (indicated by the dashed line). The gray boxes depict the standard error associated with each population mean. These standard errors were computed using the general form of Equations 5.14 and 5.13. It can be seen that the mean Fe I abundance values of the two populations are distinct; the mean value for the normal population is $\overline{[\text{Fe I/H}]}_{\text{norm}} = 0.12 \pm 0.02$ while the mean value for the YS population is $\overline{[\text{Fe I/H}]}_{\text{YS}} = -0.13 \pm 0.04$. Note that the Fe I abundance value for SG 33 was not used in the calculation of the mean for the normal star population because it shows significant radial velocity variation and is likely a binary system.

Furthermore, a two-sample Kolmogorov-Smirnov (K-S) test of the metallicities of these two populations of stars also supports the conclusion that they are drawn from different parent populations. The results of the Fe I abundance K-S test can be seen in Figure 6.4. The [Fe I/H] K-S statistic and its p-value were computed to be 2.05 and 0.00 respectively. The p-value is computed under the null hypothesis that the two populations are drawn from the same parent population. Thus, the [Fe I/H] K-S test indicates that the normal and YS populations are derived from parent populations with differing distributions. Note, however, that the K-S test is limited by the number of stars in each population.

The fact that the YS population appears to be distinct from the normal stars in M67 in terms of metallicity is problematic if the YSs are true cluster members. This is because it is assumed that the stars in a cluster are derived from the same molecular cloud and are expected to have similar chemical compositions. One is, again, encouraged to consider the possibility that the YSs are simply contaminating field stars. However, in light of the fact that some of the YSs have high proper motion membership probabilitiies and radial velocities that are consistent with the cluster mean, three other possible explanations will be considered presently.

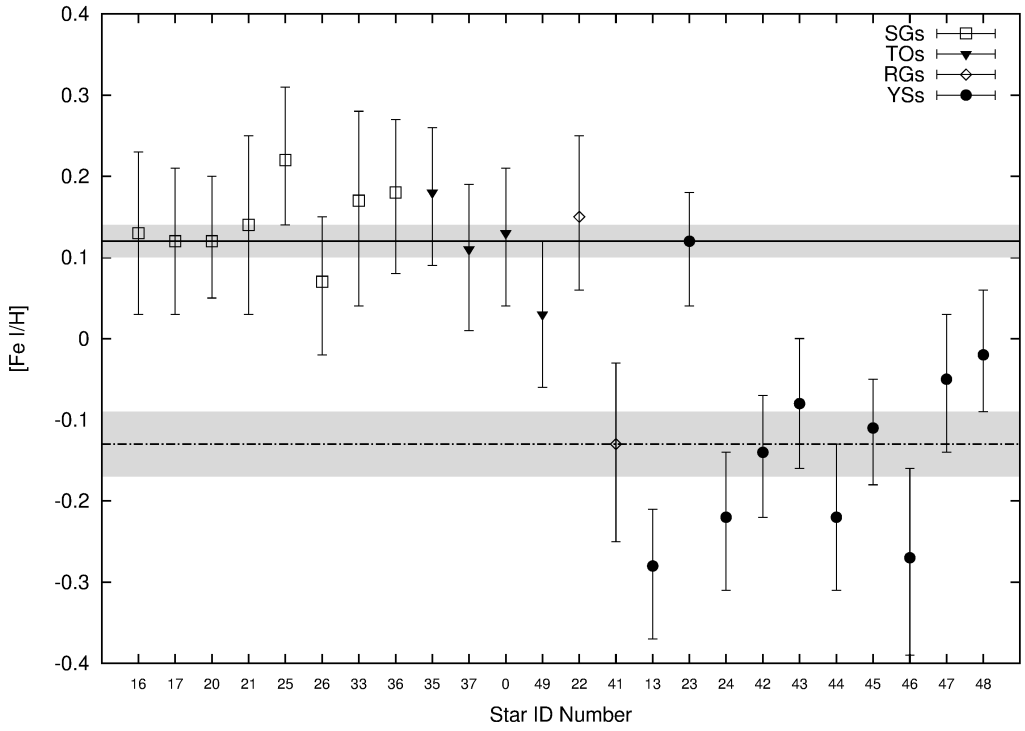

Figure 6.3: [Fe I/H] with associated uncertainties for various star types. Note that the abscissa values indicate each star's identification number in this work. The solid line indicates the mean metallicity computed for the "normal" SG and TO stars, excluding SG33 due to it's radial velocity variations and likely binary nature. The dashed line indicates the mean metallicity computed for the YS population. The two RGs were not used in the calculation of either mean value. The gray boxes indicate the standard error (as defined in Equation 5.13) associated with the mean metallicity value of each population.

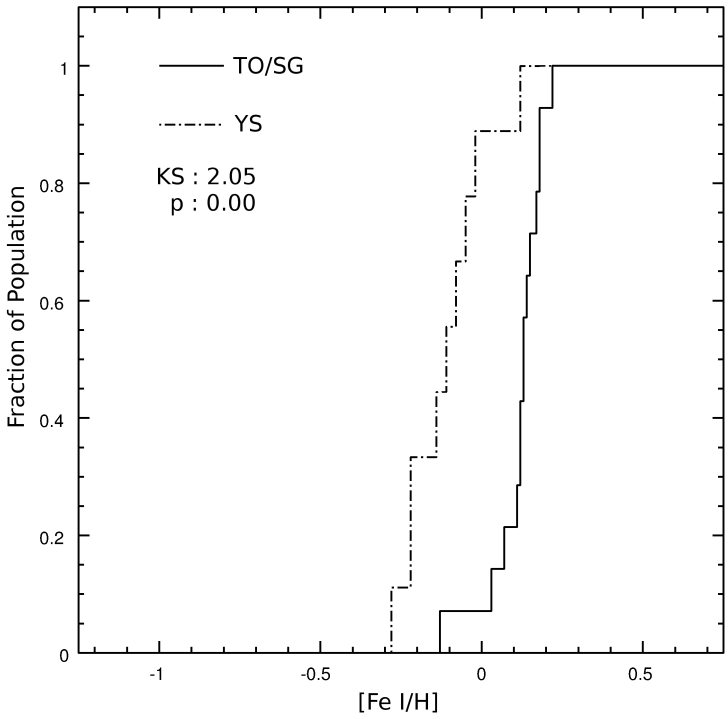

Figure 6.4: KS test for [Fe I/H].

6.2.1 1–Inaccurate Metallicity Determinations

It is acknowledged here that the mean [Fe I/H] value for the normal star population is notably higher than the values reported by others, which range from -0.09 to 0.04 (Nissen et al., 1987; Garcia Lopez et al., 1988; Hobbs & Thorburn, 1991; Friel & Boesgaard, 1992; Friel & Janes, 1993; Tautvaisiene et al., 2000; Taylor, 2007). Therefore, the possibility that the metallicities derived in the current work are inaccurate will be considered in this section via comparisons with other works.

6.2.1.1 Comparisons with Önehag et al. (2014)

A recent study by Önehag et al. (2014), aimed at exploring the understanding of the physics and evolution of solar type stars, reports elemental abundances for the star SG 36 of the current study. Additionally, Önehag et al. (2014) report stellar atmosphere parameters, a line list of the elemental lines used in their study, the equivalent widths of those lines as measured in a solar atlas and the abundances computed for each spectral line in the star. Önehag et al. (2014) do not report, however, the equivalent widths measured for each of the spectral lines in SG 36. Though they do

Table 6.1. Comparison of SG 36 Chemical Abundance Values.

Element	Wavelength	**Önehag et al. (2014)** [X/H]	**McGahee** [X/H]
Na I:	6154.230	0.02	0.03
	6160.750	-0.05	0.00
Al I:	6698.670	-0.02	0.01
Ca I:	6166.439	-0.06	0.08
Ti I:	6126.216	-0.01	0.12
	6258.102	0.03	0.00
Fe I:	6151.617	-0.04	0.10
	6498.945	0.06	0.40
Al I:	5087.420	-0.11	0.15

not present stellar equivalent widths, the rest of the data presented by Önehag et al. (2014) will be compared to the results from the current work.

Table 6.1 contains the specific abundance values listed for each element that is present in both this study and that of Önehag et al. (2014). A comparison plot of these elemental abundances for SG 36 can be seen in Figure 6.5. It is clear, in this plot, that there is disagreement between the abundance values computed for each line in the present study and those values computed by Önehag et al. (2014). In particular, there is strong disagreement between the Fe abundances computed in both studies. The following paragraphs discuss potential reasons for these discrepancies.

The stellar atmosphere parameters derived by Önehag et al. (2014) and in this study are presented in Table 6.2. Önehag et al. (2014) derived T_{eff} by taking the mean of two values: one computed from the photometric color indices $(V - K_s)$ and $(V - I_c)$ and one computed by matching the Hα wings to a synthetic spectrum. They derived $\log(g)$ by estimating each star's mass from the star's de-reddened V magnitude and an isochrone fit to M67. Their solar models were computed using these estimates of T_{eff} and $\log(g)$ and assuming solar abundances of all elements. Abundances were computed for each Fe I spectral line, and ξ_t was then determined by adjusting its value until the abundances computed for all of the Fe I lines were as "equal as possible." The derived sensitivities of the Fe I abundance to each of these parameters from both the current study from Önehag et al. (2014) are listed in Table 6.3. Note that in the present work, sensitivities were, in some cases, found to vary depending on whether the parameter in question was being increased or decreased. Also note that the Fe II sensitivities were typically different than the Fe I sensitivities. Önehag

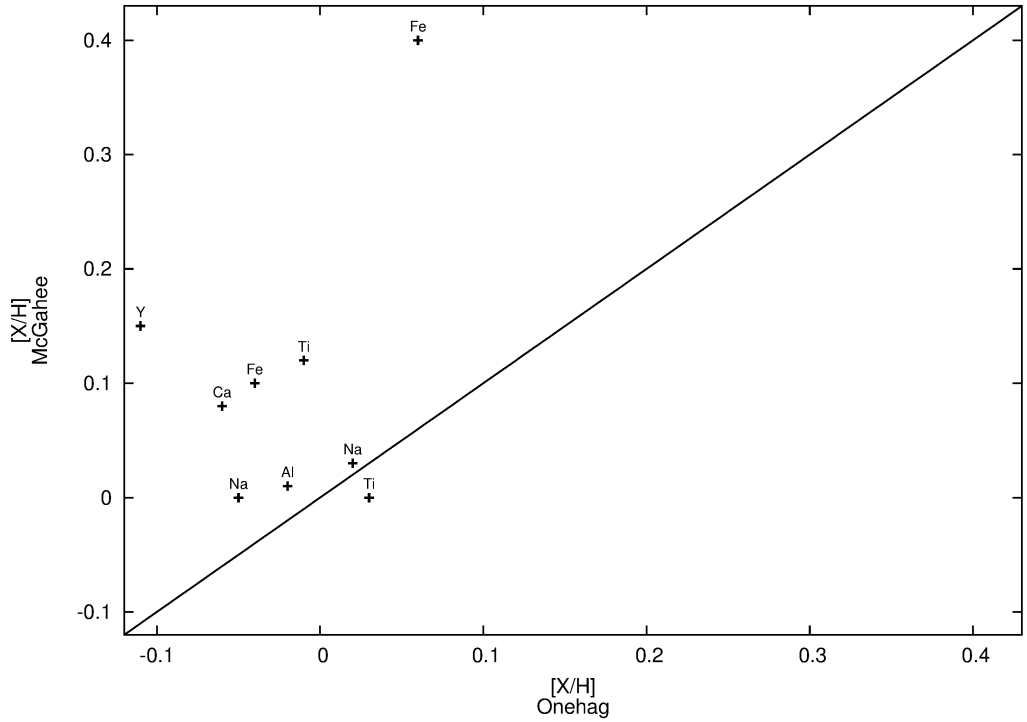

Figure 6.5: The abundance values computed for individual spectral lines are compared between this study and that of Önehag et al. (2014). The solid line indicates a 1-to-1 relation for reference.

et al. (2014) present only one value for the Fe sensitivity (presumably the Fe I sensitivity) to what are, also presumably, increases in the value of each parameter. The sensitivities reported from the current work, are the sensitivities of the Fe abundance due to increases in the parameter in question in Table 6.3.

A comparison of the solar equivalent widths measured in both studies reveals a notable discrepancy between the equivalent widths measured for the two Fe I lines that are in common between the studies: λ6151 and λ6498 (see Table 6.4). The discrepancies between the studies for each of the Fe lines is roughly 60%. Upon this discovery, the equivalent widths of those lines were

Table 6.2. Stellar Atmosphere Parameters for SG 36.

Study	$T_e$ff (K)	log(g) (dex)	[Fe I/H] (dex)	ξ_t (km/s)
Önehag et al. (2014):	6061	3.82	-0.03	1.6
McGahee:	6025	3.90	0.18	1.40

Table 6.3. Fe I Sensitivities for SG 36.

Study	$T_e$ff	log(g)	ξ_t
Önehag et al. (2014):	0.0006	0.00	-0.10
McGahee:	0.0008	-0.10	-0.30

Note. — This table contains the Fe I abundance sensitivities derived in the present work by increasing the value of the parameter in question. The Önehag et al. (2014) sensitivities were simply indicated for Fe. The T_{eff} values are per Kelvin, the log(g) values are per dex and the ξ_t values are per (km/s).

Table 6.4. Comparison of Solar Equivalent Widths.

	Önehag et al. (2014)	**McGahee**
Wavelength	EW (mÅ)	EW (mÅ)
6154.230	40.6	41.0
6160.750	62.2	63.0
6698.670	22.4	30.2
6166.439	73.8	66.8
6126.216	24.1	24.1
6258.102	52.9	56.0
6151.617	125.4	48.9
6498.945	108.6	47.3
5087.420	50.6	49.4

checked and subsequent measurements agreed with the values determined previously in the current study. Additionally, both Bubar & King (2010) and King et al. (1998) find equivalent widths for these lines in the sun in that are in agreement with the values determined in the current work. Note, however, that when the Fe I lines are disregarded, the equivalent widths measured differ, on average, by only $\sim 4\%$. The equivalent width measurements for the lines in common between both studies are listed in Table 6.4.

A visual comparison of the solar equivalent widths can be seen in Figure 6.6. Again, it is clear that the solar equivalent widths are in agreement between the two studies with the exception of the two Fe lines. In a differential analysis, an overestimation of an equivalent width and thus

an elemental abundance would drive down the stellar abundance. Thus the overestimation of the equivalent widths of the Fe lines in Önehag et al. (2014) could be a contributing factor in the lower Fe abundance reported by them. Considering the consistency between the stellar atmosphere parameters and sensitivities determined in both studies, it is likely that this difference in the derived metallicity for SG 36 is closely related to the discrepancies in the equivalent widths measured for these Fe I lines. Because Önehag et al. (2014) provide no additional equivalent width information for the Fe I lines in SG 36, no further investigation can be conducted. It cannot, however, be concluded that the metallicity determined in the current study is unreliable.

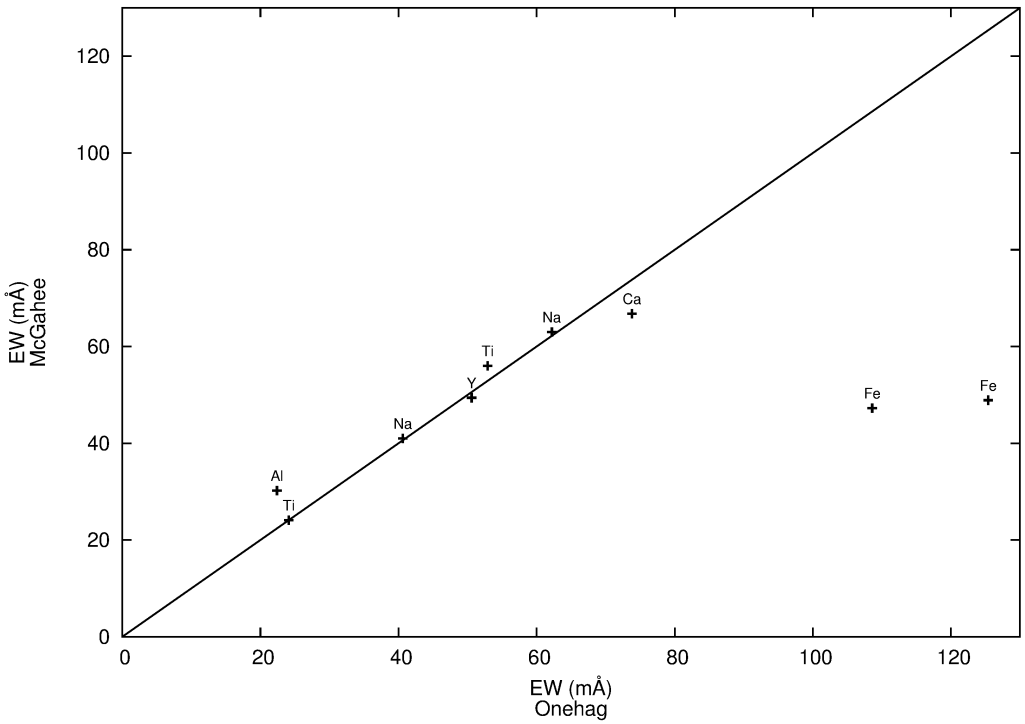

Figure 6.6: The equivalent widths of solar lines are compared between the current study and that of Önehag et al. (2014). The solid line indicates a 1-to-1 relation for reference.

6.2.1.2 Comparisons with Jacobson et al. (2011)

A study by Jacobson et al. (2011) aims to determine chemical abundances of open clusters. In the process, they reported chemical abundances for the stars RG 41, YS 43 and YS 44 of the current study. Figure 6.8 depicts a comparison between the mean abundance values computed in the present study and those computed by Jacobson et al. (2011). The mean chemical abundance

Table 6.5. Comparison of RG 41, YS 43 and YS 44 Mean Abundance Values.

	Jacobson et al. (2011)			**McGahee**		
Element	RG 41 [X/H]	YS 43 [X/H]	YS 44 [X/H]	RG 41 [X/H]	YS 43 [X/H]	YS 44 [X/H]
Fe I	-0.07	-0.11	-0.09	-0.13	-0.08	-0.22
Ni I	-0.03	-0.14	-0.08	-0.27	-0.16	-0.29
Cr I	0.38	-0.01	-0.06	-0.45	-0.20	-0.45
Na I	-0.09	0.01	0.01	0.01	0.02	0.04
Ti I	0.00	-0.15	-0.09	-0.22	-0.15	-0.28
Ca I	-0.25	-0.18	-0.14	-0.13	-0.04	-0.22
Si I	0.14	0.09	0.10	-0.11	-0.08	-0.13
O I	-0.10	-0.35	-0.20	-0.09	0.16	0.03
Al I	0.48	0.18	0.30	0.15	0.00	0.10

values for RG 41, YS 43 and YS 44 are listed in Table 6.5. The abundances computed in the current study differ from those computed by Jacobson et al. (2011) by only 10% on average. Furthermore, considering only the Fe abundances, Figure 6.7 shows that two of the three stars in common in both studies have mean Fe abundances that agree to within the uncertainties determined in the current study. On average the Fe abundances differ by only 5% between the two studies.

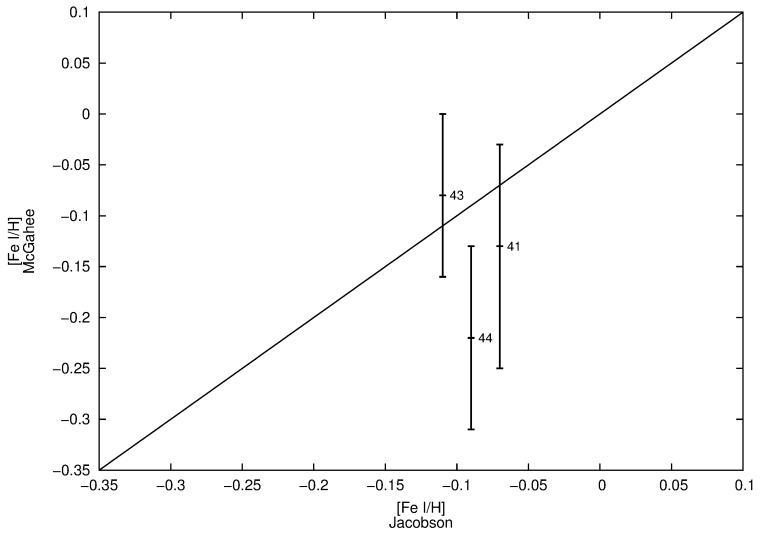

Figure 6.7: The mean [Fe I/H] values computed in this study and in Jacobson et al. (2011) are compared for RG 41, YS 43 and YS 44. The solid line indicates a 1-to-1 relation for reference.

Jacobson et al. (2011) state that they chose to not use the Fe ionization and excitation balance that was employed in the current study because they felt they had too few Fe lines to ensure

Table 6.6. Stellar Atmosphere Parameters for RG 41, YS 43 and YS 44.

Study	$T_{e}ff$ (K)	log(g) (dex)	[Fe I/H] (dex)	ξ_{t} (km/s)
Jacobson et al. (2011):				
RG 41	4800	2.9	-0.07	1.5
YS 43	5100	3.0	-0.11	1.5
YS 44	5000	2.7	-0.09	1.5
McGahee:				
RG 41	4850	2.60	-0.13	2.10
YS 43	5265	3.42	-0.08	2.03
YS 44	5050	2.81	-0.22	2.33

that the results of the process would be reliable. Instead, they determine T_{eff} using extinction-corrected magnitudes and colors and taking the average of the (B-V), (V-K) and (J-K) temperatures. They also state that they determine log(g) from the relation:

$$\log(g) = \log(m/m_{\odot}) - 0.4(M_{bol,\odot} - M_{bol,*}) + 4\log(T/T_{\odot}) + \log(g_{\odot}) \tag{6.1}$$

Lastly, they adopted a microturbulent velocity (ξ_{t}) of 1.5 km/s for all stars and after investigation, claim that "no major systematics are introduced into [their] results as a result of [their] treatment of the microturbulence." The stellar atmosphere parameters for RG 41, YS 43 and YS 44 from both studies are listed in Table 6.6 for comparison.

A visual comparison of the equivalent widths of various spectral lines can be seen in Figure 6.9. On average, the equivalent widths measured in this study agree with those of Jacobson et al. (2011) to within $\sim 5\%$. The equivalent width measurements from both studies are listed explicitly in Table 6.7.

Table 6.7. Comparison of RG 41, YS 43 and YS 44 Equivalent Widths.

		Jacobson et al. (2011)			**McGahee**		
Element	Wavelength (Å)	RG 41 EW (mÅ)	YS 43 EW (mÅ)	YS 44 EW (mÅ)	RG 41 EW (mÅ)	YS 43 EW (mÅ)	YS 44 EW (mÅ)
Fe I:	6151.617	82	71	85	97.5	74.3	87.5
	6157.728	112	92	97	119.5	94.1	102.3
	6165.360	64	61	64	82.9	70.3	73.3
	6173.336	110	88	102	138.2	104.7	114.0
	6232.641	126	116	117	129.1	119.6	137.5
	6322.685	129	114	120	138.3	119.8	99.9
	6336.820	142	133	130	148.3	141.4	30.1
	6344.148	117	112	107	155.8	122.2	81.1
	6469.193	104	73	91	83.0	80.9	77.5
	6646.932	50	33	41	53.9	27.0	70.4
	6703.567	96	69	77	94.1	64.1	62.6
	6705.101	79	66	71	88.0	68.4	68.1
Fe II:	6149.249	46	56	59	44.6	55.4	60.4
	6247.557	61	73	71	57.1	72.4	73.3
	6369.462	28	39	54	50.4	35.4	42.5
	6416.919	41	65	65	56.8	49.1	54.1
	6456.380	71	86	87	89.5	93.9	98.2
Na I:	6154.230	79	70	76	84.0	60.9	77.8
	6160.750	93	85	85	109.4	92.8	105.8
Si I:	6142.480	52	48	51	48.0	49.5	52.7
	6145.010	51	50	50	54.2	50.5	52.7

Table 6.7 (cont'd)

		Jacobson et al. (2011)			**McGahee**		
Element	Wavelength (Å)	RG 41 EW (mÅ)	YS 43 EW (mÅ)	YS 44 EW (mÅ)	RG 41 EW (mÅ)	YS 43 EW (mÅ)	YS 44 EW (mÅ)
	6155.130	81	91	88	95.9	92.6	98.4
Ca I:	6166.439	95	87	95	112.7	95.8	98.0
Ni I:	6175.370	63	63	69	82.3	69.3	74.4
	6204.605	54	39	45	50.1	41.5	48.7
	6772.320	82	68	82	86.0	67.6	78.5

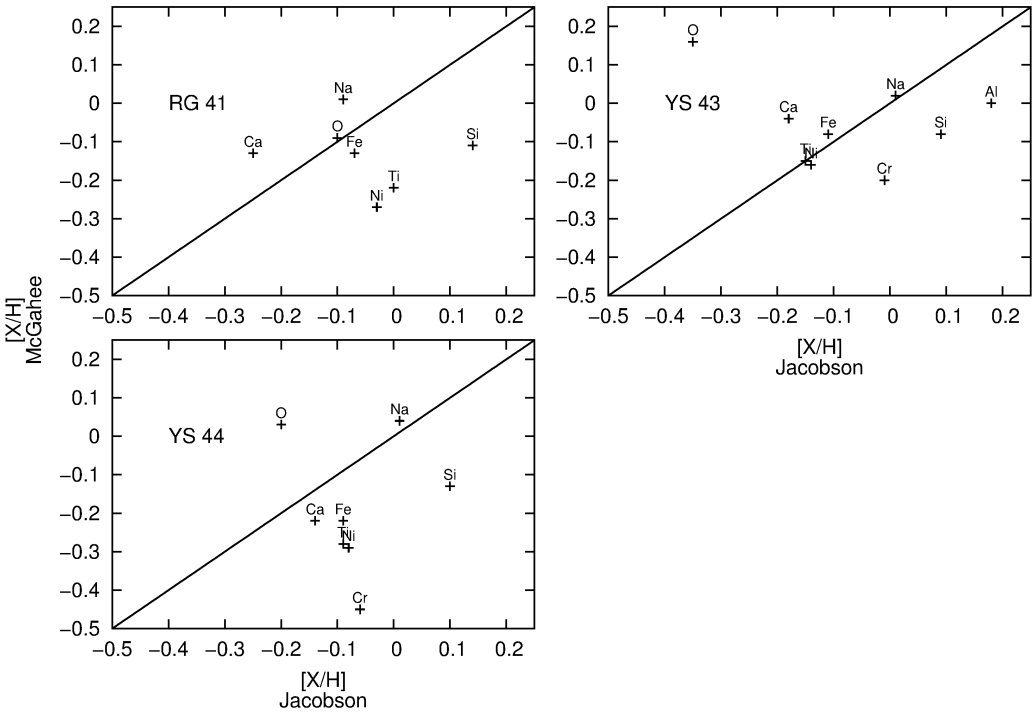

Figure 6.8: The mean abundance values computed in the current study and in Jacobson et al. (2011) are compared for RG 41 (top left panel) YS 43 (top right panel) and YS 44 (bottom panel). The solid line indicates a 1-to-1 relation for reference in all panels.

In comparing the results of this study with those of Jacobson et al. (2011), it appears as though the equivalent width measurements are not responsible for the discrepancy in various chemical abundance values between the two studies. It is possible that the difference in the treatment of the stellar atmosphere parameters between the two studies could be responsible for the discrepancies that are seen for particular elements. However, it has been shown that there is no substantial disagreement

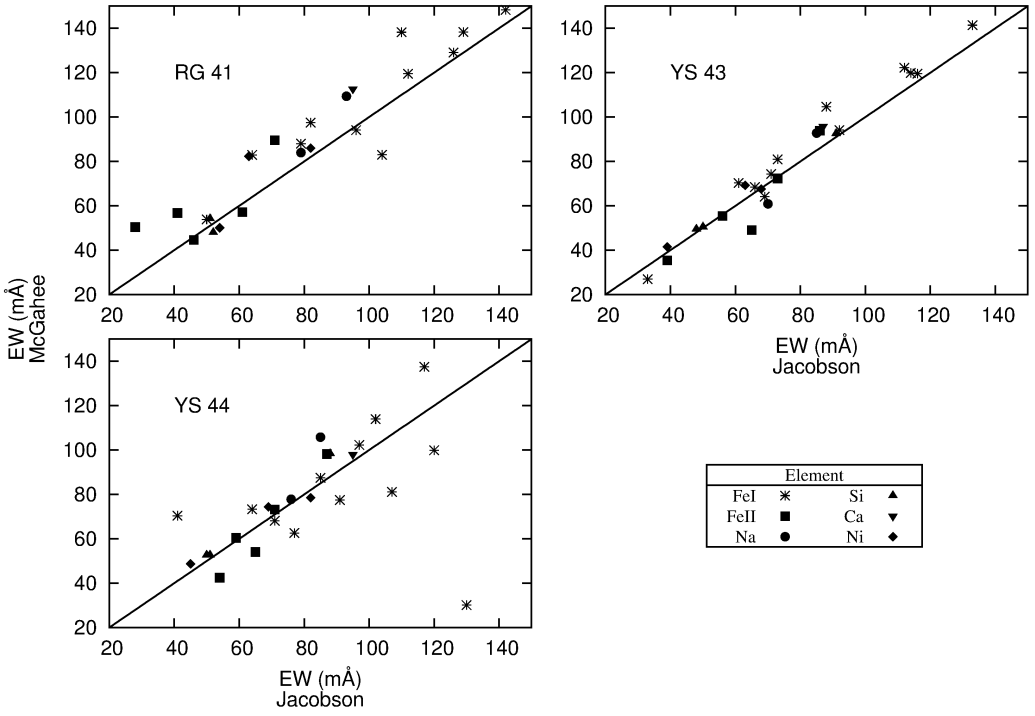

Figure 6.9: The equivalent widths for various spectral lines measured in the current study and in Jacobson et al. (2011) are compared for RG 41 (top left panel), YS 43 (top right panel) and YS 44 (bottom panel). The solid line indicates a 1-to-1 relation for reference in all panels.

between the metallicities ([Fe I/H] values) derived by Jacobson et al. (2011) and those derived in the current work for RG 41, YS 43 and YS 44. Therefore, it is concluded that the metallicities derived in the current study are, in fact, reliable and the difference in the metallicities between the YSs and the normal stars in the current study cannot be explained as inaccurate metallicity determinations for the stars.

6.2.2 2–A Speculation About a Metallicity Enhancing Period in the History of M67

In this section, an explanation of the metallicity discrepancy between the YSs and the normal stars of M67 is attempted by speculating about a potential metal-enriching period in the history of M67. In order to explain the discrepancy, this metal-enriching scenario requires several assumptions: 1) in the history of M67, the massive stars returned metal enriched material to the cluster through supernova explosions, successfully polluting the still MS burning stars 2) the amount

of pollution was sufficient enough so that these MS stars began to exhibit enhanced metallicities and 3) that some undetermined mechanism operates in the YSs allowing them to exhibit their original metallicities. This is quite an exotic scenario, however, if it were responsible for the metallicity discrepancies, one could expect that as the MS stars evolve away from the MS and begin to cool, that their convective zones will deepen and effectively erase the enhanced metallicities exhibited by the polluted MS stars. To investigate this possibility, one can look for a negative correlation between [Fe I/H] and the color index (B-V) of the stars in the current work. It can be seen in the top panel of Figure 6.10, that no such correlation exists for the M67 TOs, SGs and RGs that were investigated in the current work. Furthermore, there is no such correlation seen for the YSs (see the bottom panel of Figure 6.10) either. This is a good indication that a scenario similar to the one described here is not responsible for the metallicity discrepancy seen between the YSs and the normal stars of M67.

6.2.3 3–Revisiting a Hypothesis of Field Star Contamination

Lastly, the hypothesis that the YSs are simply contaminating field stars in the field of view of M67 is revisited. This hypothesis again seems plausible given the metallicity discrepancies between the YSs and the normal stars in M67. To further investigate this hypothesis, the overall chemical abundance patterns of both the normal stars and the YSs will be considered. In particular, the abundances for Ni, Cr, Ba, Y, Na, Ti I, Ti II, Ca, S, C, O and Al are examined. Abundance plots, similar to Figure 6.3, have been generated for each element and can be found in Appendix C in Figures 18, 19 and 20. Additionally, a K-S test was performed for each element, the results of which, are illustrated in Appendix C in Figures 21, 22 and 23. It is noted that the only case where there is greater than 1σ confidence that the two populations are drawn from the same parent population is found in the K-S test for oxygen–the bottom right panel of Figure 23. The resulting overall abundance pattern of the YSs again indicates that the YSs are derived from a different parent population than the normal stars considered in the present work and suggests that these stars could be contaminating field stars.

Bensby et al. (2004) presented chemical abundances for field stars of various metallicities. The results of this work have been used to compare the abundance patterns of the YSs to those of field stars with similar metallicities. Visual comparisons can be seen in Figures 6.11, 6.12 and 6.13. In these plots the field stars are indicated with small gray filled circles. It can be seen that the abundance pattern of the YSs tends to disagree with those seen for the field stars, perhaps more

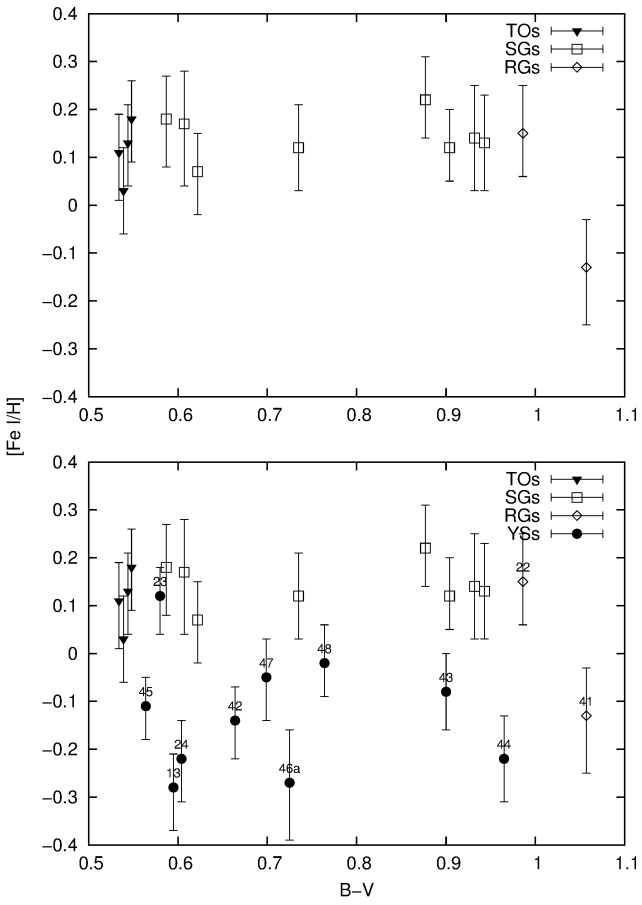

Figure 6.10: The top panel shows no correlation between the [Fe I/H] values and the B-V indices for the TOs, SGs and RGs. The YSs have been added to the plot in the bottom panel, labeled with the identification numbers assigned in the current work for reference. Again, no correlation is seen.

so than the majority of the normal cluster stars considered in the current study. This finding casts considerable doubt on the hypothesis that the YSs can be explained as a population of contaminating field stars, however, it does appear that some individual YS abundance patterns may agree with those seen for the field stars.

6.3 Considering the s-process Elements

One of the primary purposes of the current work was to investigate the s-process element abundances of the YSs to see if these elements are enhanced. An enhancement of the s-process elements would support a hypothesis in which RLOF mass transfer occurred in the stars' histories.

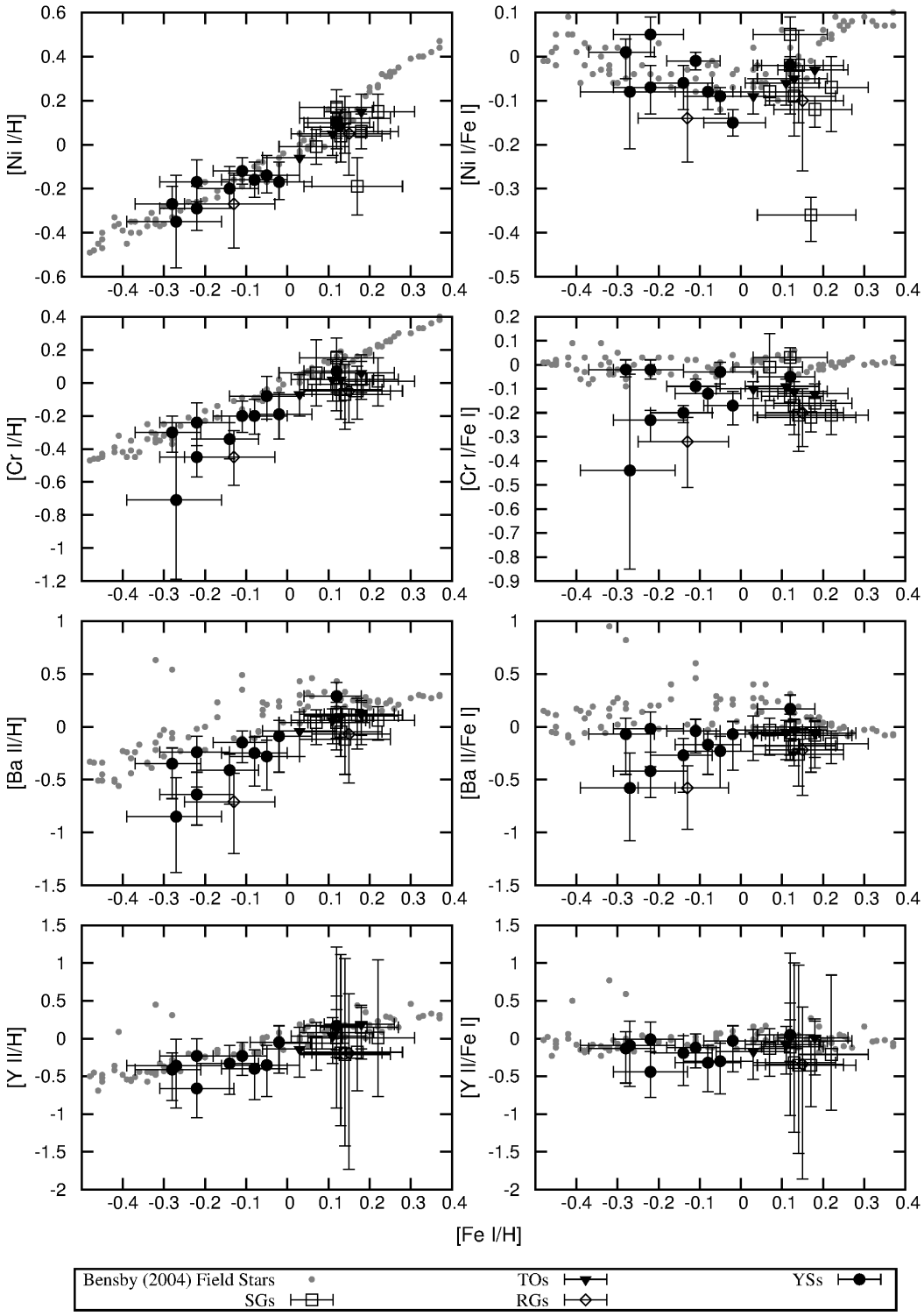

Figure 6.11: Abundances derived in the current study compared to those derived by Bensby et al. (2004) for field stars with similar metallicities.

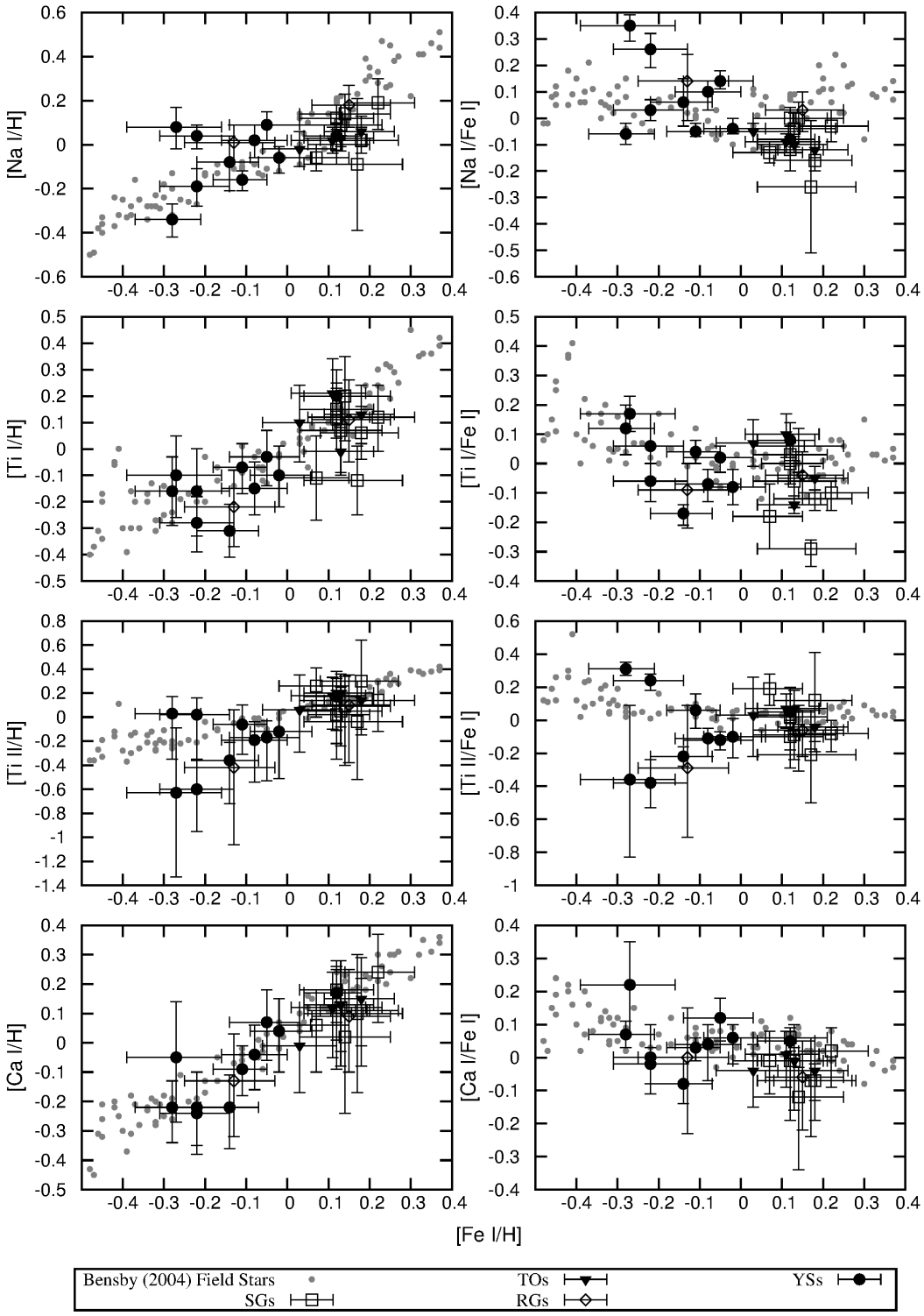

Figure 6.12: Abundances derived in the current study compared to those derived by Bensby et al. (2004) for field stars with similar metallicities.

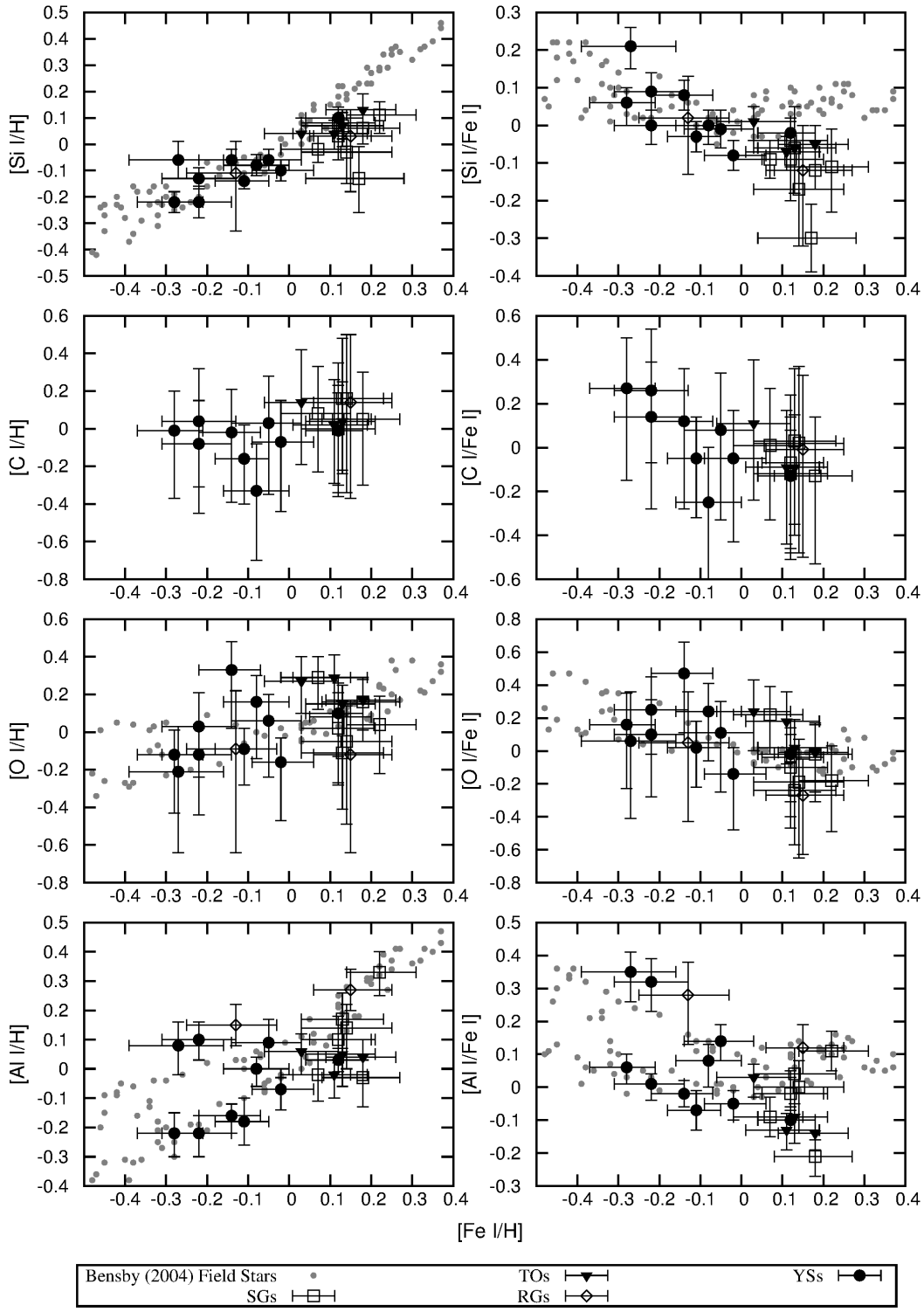

Figure 6.13: Abundances derived in the current study compared to those derived by Bensby et al. (2004) for field stars with similar metallicities.

Attempts were made to determine abundances for the s-process elements Ba, Y, Sr, Zr and Pb. Equivalent widths were measured for Ba and Y and abundances were successfully inferred, however, the resolution of the spectra obtained for the current study was insufficient for measuring the equivalent widths of lines of Sr, Zr and Pb. The abundance plots for Y and Ba from Figure 6.11 have been enlarged and identification numbers have been added for the YSs for examination. Clearly, no enhancement of Y or Ba are seen for any YS. Therefore, a past episode of RLOF mass transfer cannot be confirmed for these stars. This is perplexing however, when YS 43 is considered. It was discussed in §1.3.4 that an independent study by Landsman et al. (1997) determined that this star likely experienced a prior episode of RLOF mass transfer, however the current study finds an underabundance of both Y and Ba. This issue will be addressed further in §7.

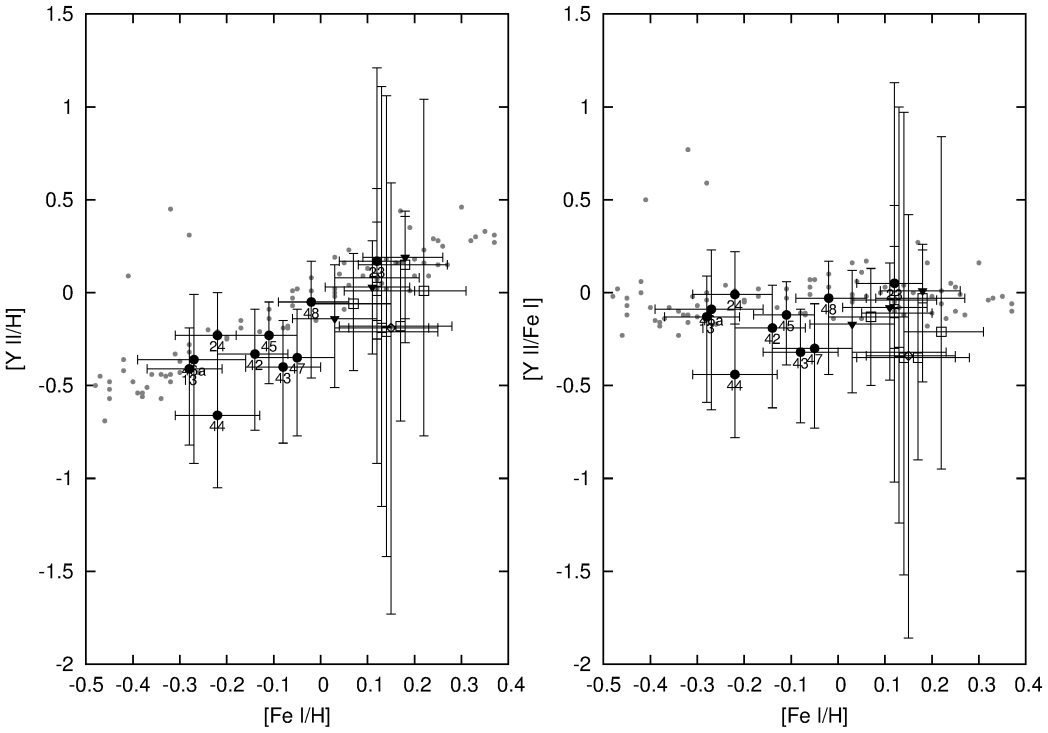

Figure 6.14: The yttrium abundances for all stars involved in the current study compared to the values derived by Bensby et al. (2004) for field stars of various metallicities. The YSs have been labeled with the identification numbers assigned in the current study.

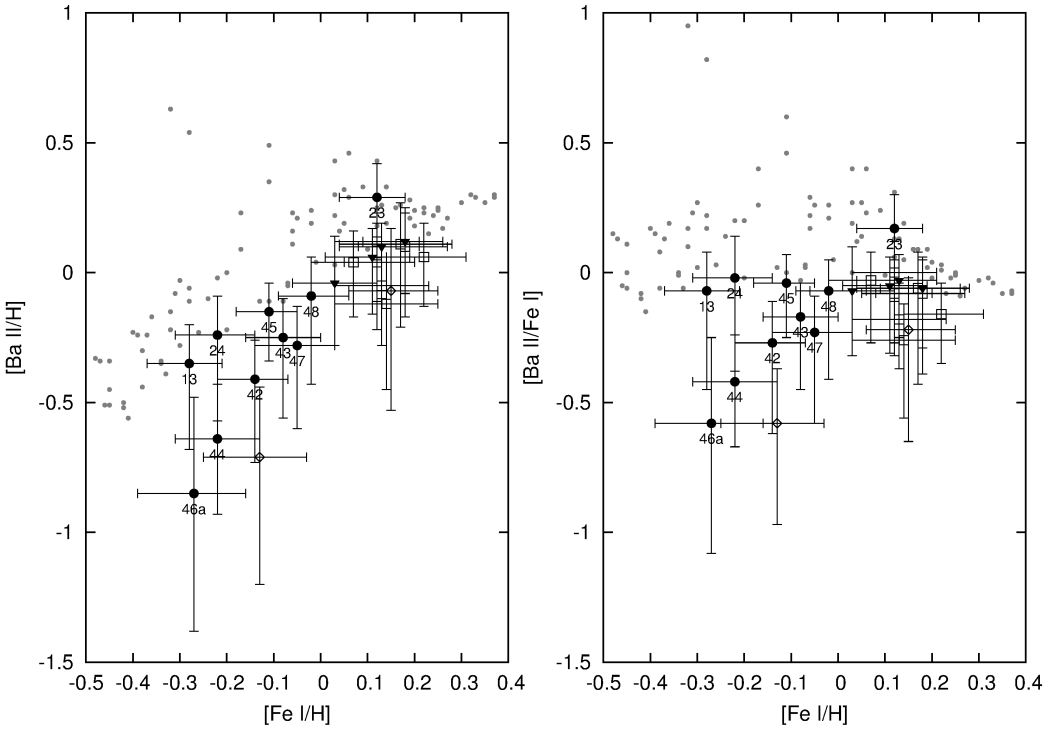

Figure 6.15: The barium abundances for all stars involved in the current study compared to the values derived by Bensby et al. (2004) for field stars of various metallicities. The YSs have been labeled with the identification numbers assigned in the current study.

Chapter 7

Conclusions

The results of the current study have shown that the YS population exhibits a high binary frequency, however, none of the YSs exhibit s-process element enhancements. *Therefore, a previous episode of RLOF mass transfer cannot be confirmed for the yellow straggler stars.* However, a few final points should be addressed.

Are the metallicities derived in the current work reliable?

The mean metallicity, or [Fe I/H] value derived for the normal stars involved in the current abundance analysis is significantly different than the mean metallicity derived for M67 by numerous others. This is likely not due to the resolution of the spectra; comparisons of the equivalents widths of the the Fe I lines measured in the current work with the equivalent widths from Jacobson et al. (2011) indicate similar measurements. Furthermore, the Fe I abundance values inferred in the current work agree with the abundance values inferred by Jacobson et al. (2011). Therefore, there is no obvious reason that the [Fe I/H] values determined in the current work should not be reliable. It is noted, however, that the discrepancy of the metallicities between the YSs and the normal stars could not be explained by any of the three hypotheses considered in §6.2. It is interesting that the metallicity of RG 22 mimicked that of the normal stars while the metallicity of RG 41 mimicked that of the YSs. A follow-up study on the RGs in M67 may provide clues as to why this discrepancy between the YSs and the normal stars exists.

Are the YSs a population of contaminating field stars?

It has been shown that both the radial velocity data and the abundance data for the YSs can be used to argue that the YSs are simply a population of contaminating field stars. However, it has

also been pointed out that it is unlikely that all YSs are field stars given: 1) the high membership probabilities of some YSs 2) the fact that likely members in both the Mathieu et al. (1986) and Yadav et al. (2008) studies exhibit radial velocities similar to those seen for the majority of the YSs 3) the binary frequency that would be required of a population of field stars that happens to reside in the YS region of the CMD of M67 and 4) the fact that the abundance patterns of the YSs tend to disagree with the abundance patterns of field stars with similar metallicities. The contaminating field star hypothesis is not a sufficient explanation all YSs, however, it is again reiterated that this explanation is likely sufficient for some of the YSs. To address this, individual YSs are discussed in Appendix D. In the discussion found there, membership probabilities, radial velocities and abundances are considered simultaneously. In some cases, however, the nature of the YS in question is still not clear. A follow-up study to obtain further radial velocity data in order to establish orbital parameters for the YS binaries may help illuminate the situation for individual YSs. Comparison of the orbital parameters of a specific YS to the parameters that are typical for field stars binaries could help indicate whether the YS in question is likely a field star.

Does the fact that s-process elements are not enhanced in YSs mean that these stars have not experienced an episode of RLOF mass transfer?

If s-process elements had been detected for the YSs, it would have been a "smoking gun" for a prior episode of RLOF mass transfer. However, the fact that these enhancements are not seen does not rule out a history of mass transfer for the YSs. Preston & Sneden (2004) did find enhancements of s-process elements in the blue metal poor stars (BMPs), however, these enhancements were typically seen in only the most metal poor stars in their sample. So there seemed to be a correlation between the overall metallicity of the BMPs and whether or not they showed the s-process element enhancements. This leads one to consider that there could be a dilution effect for the YSs; if these stars have have in fact been polluted by previous AGB companions but their overall metallicities are relatively high, they may not be capable of exhibiting their s-process element enhancements. If this is the case, then it may be that these types of enhancements simply can't be seen. This could be a possible explanation for why no enhancements are seen in YS 43 which is believed to have experienced this type of mass transfer. However, a better understanding of the amount of material accreted in the mass transfer process, the ratio of the s-process material to the total amount of material accreted and the convection zone depths of the YSs could all help to better predict whether or not these s-process element enhancements can be expected for the M67 yellow straggler stars.

Appendices

Appendix A Stellar Targets of Observation

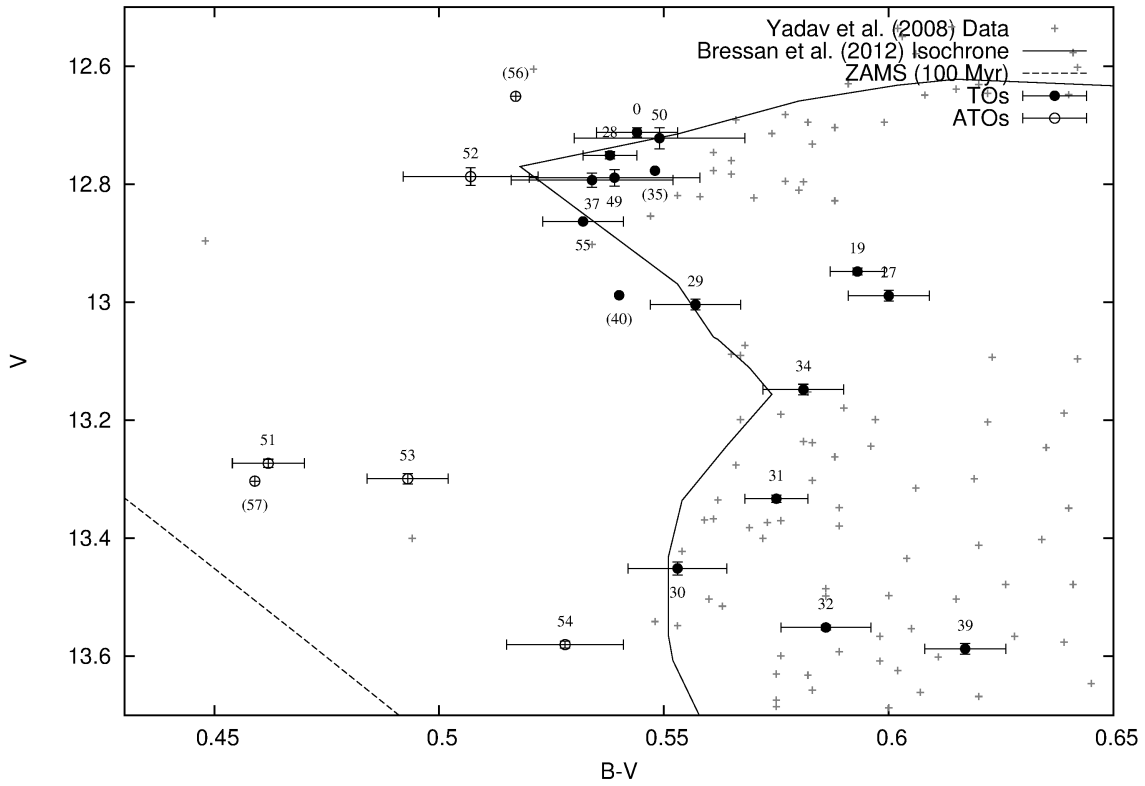

Figure 1: Turnoff stars (TOs) and anomalous turnoff stars (ATOs) plotted according to their Yadav et al. (2008) photometry. Each star has been labeled with the identification number assigned in the current study. Identification numbers enclosed in parentheses indicate the stars for which no Yadav et al. (2008) photometry was available. In these cases, the star has been plotted according to its Montgomery et al. (1993) photometry.

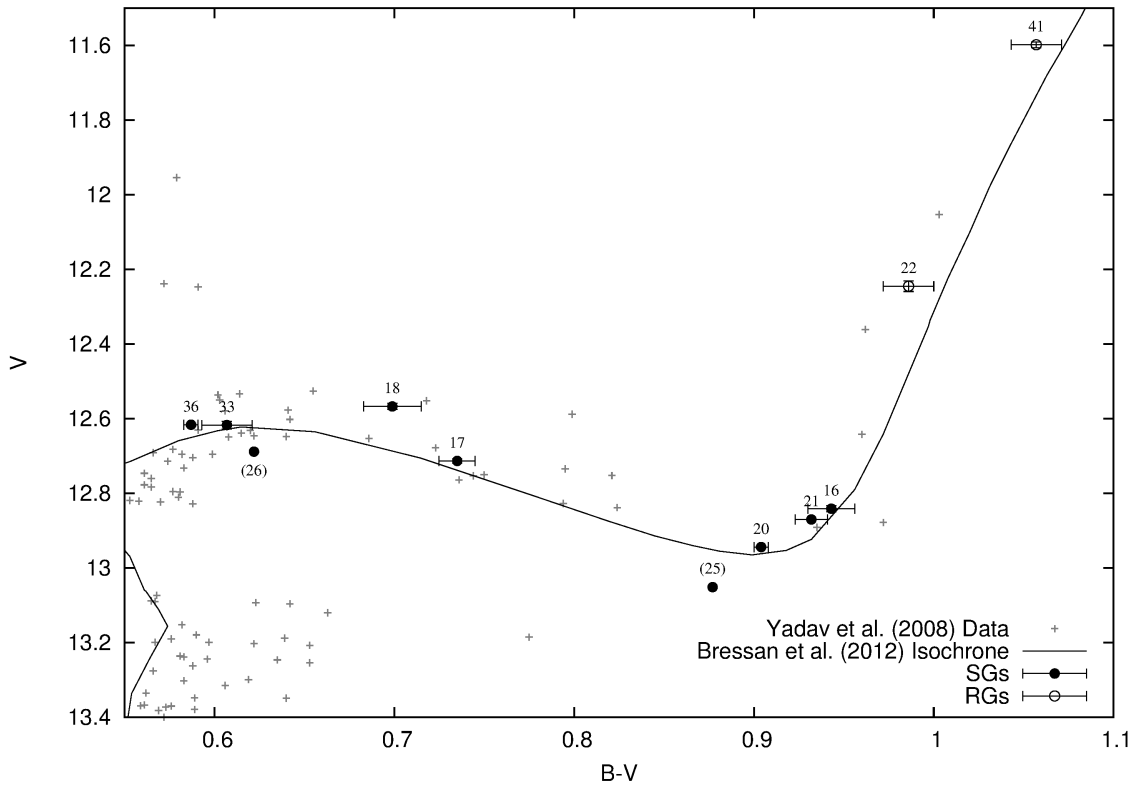

Figure 2: Subgiant stars (SGs) and red giant stars (RGs) plotted according to their Yadav et al. (2008) photometry. Each star has been labeled with the identification number assigned in the current study. Identification numbers enclosed in parentheses indicate the stars for which no Yadav et al. (2008) photometry was available. In these cases, the star has been plotted according to its Montgomery et al. (1993) photometry.

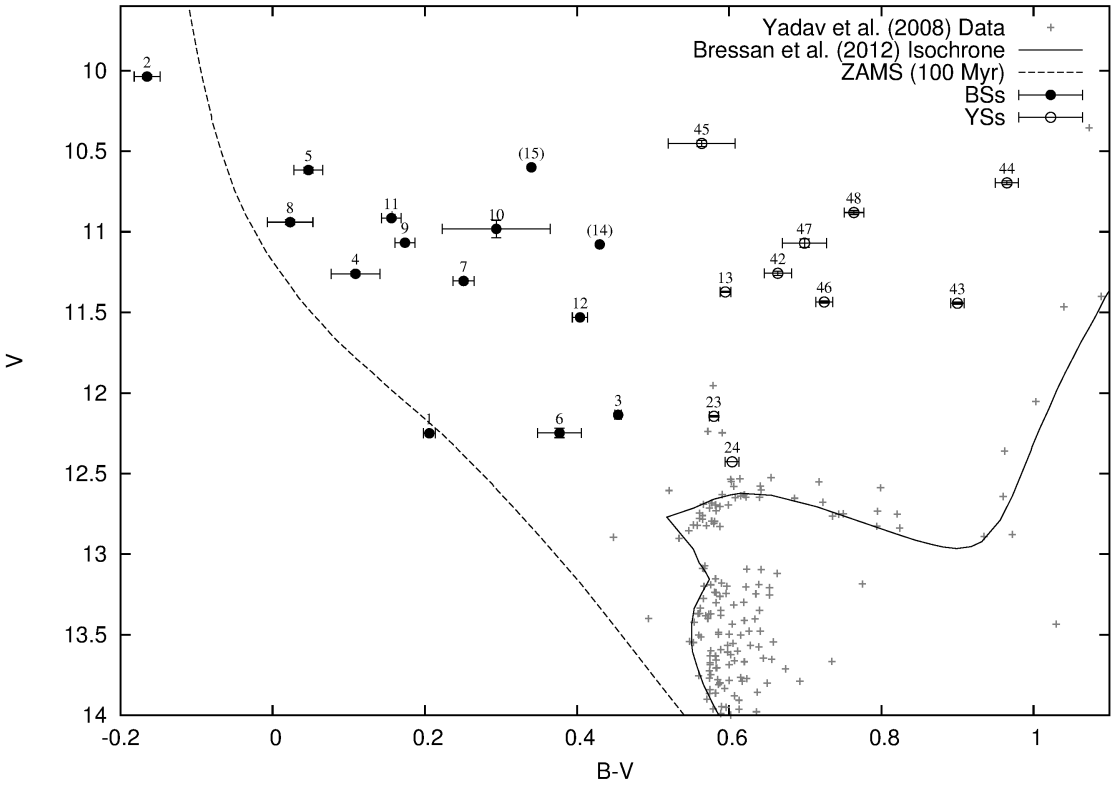

Figure 3: Blue straggler stars (BSs) and yellow straggler stars (YSs) plotted according to their Yadav et al. (2008) photometry. Each star has been labeled with the identification number assigned in the current study. Identification numbers enclosed in parentheses indicate the stars for which no Yadav et al. (2008) photometry was available. In these cases, the star has been plotted according to its Montgomery et al. (1993) photometry.

Appendix B Radial Velocity Survey Data

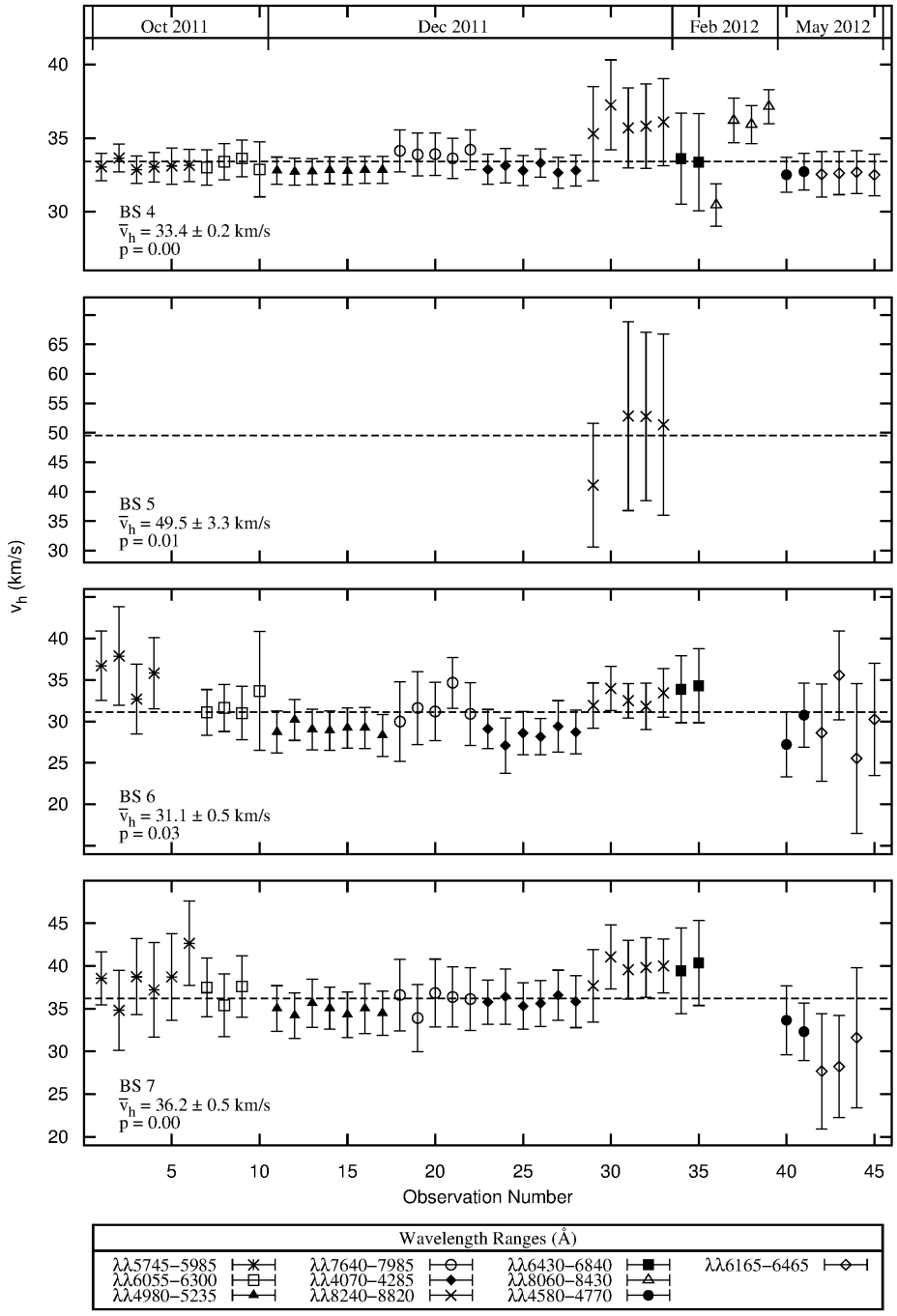

Figure 4: Radial Velocity Plots for BS4, BS5, BS6 and BS7. Note that for stars that exhibit variable radial velocity measurements, the mean value computed in the present work is not representative of a systemic radial velocity for the binary system. It is simply an average of the radial velocity measurements computed.

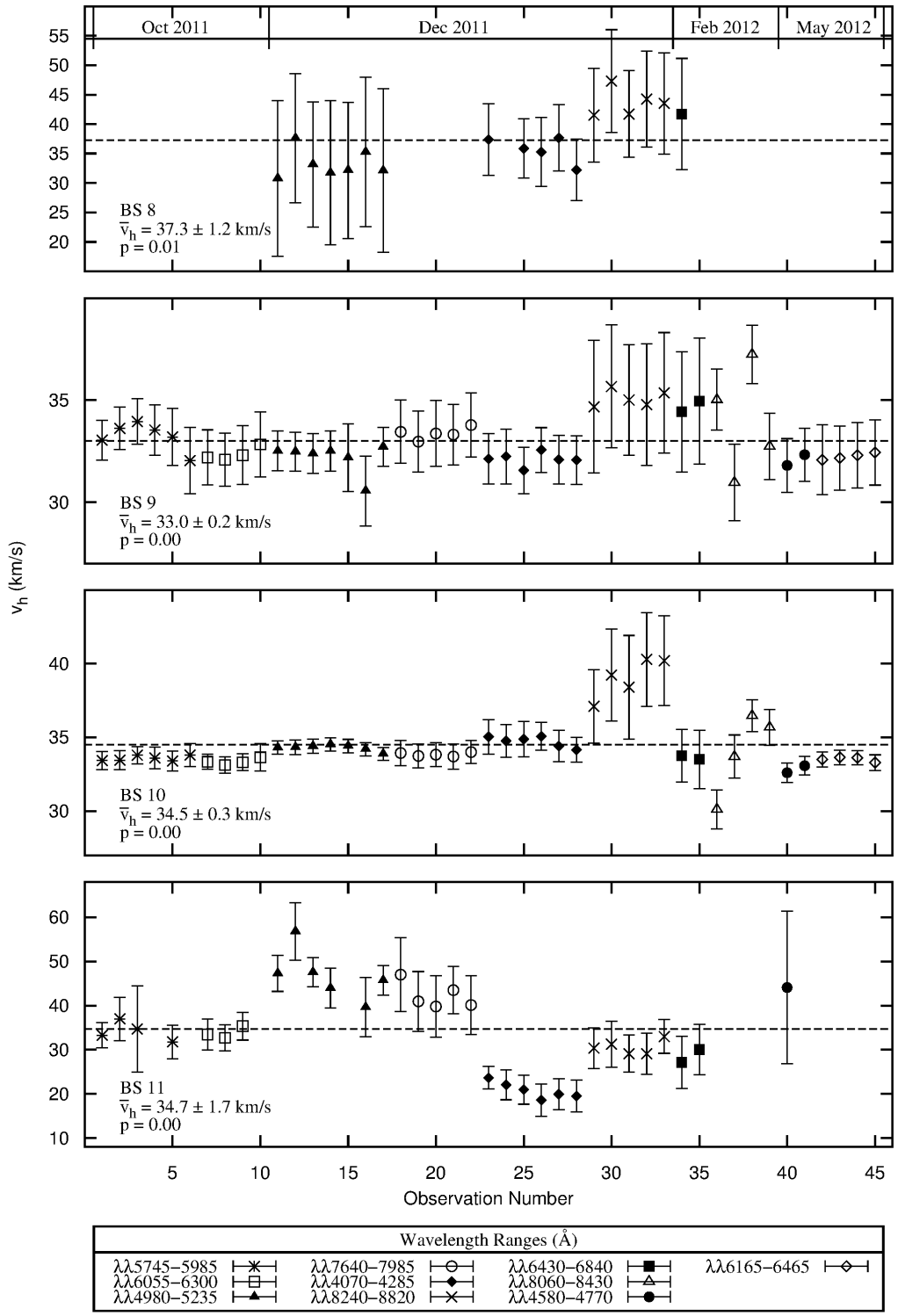

Figure 5: Radial Velocity Plots for BS8, BS9, BS10 and BS11. Note that for stars that exhibit variable radial velocity measurements, the mean value computed in the present work is not representative of a systemic radial velocity for the binary system. It is simply an average of the radial velocity measurements computed.

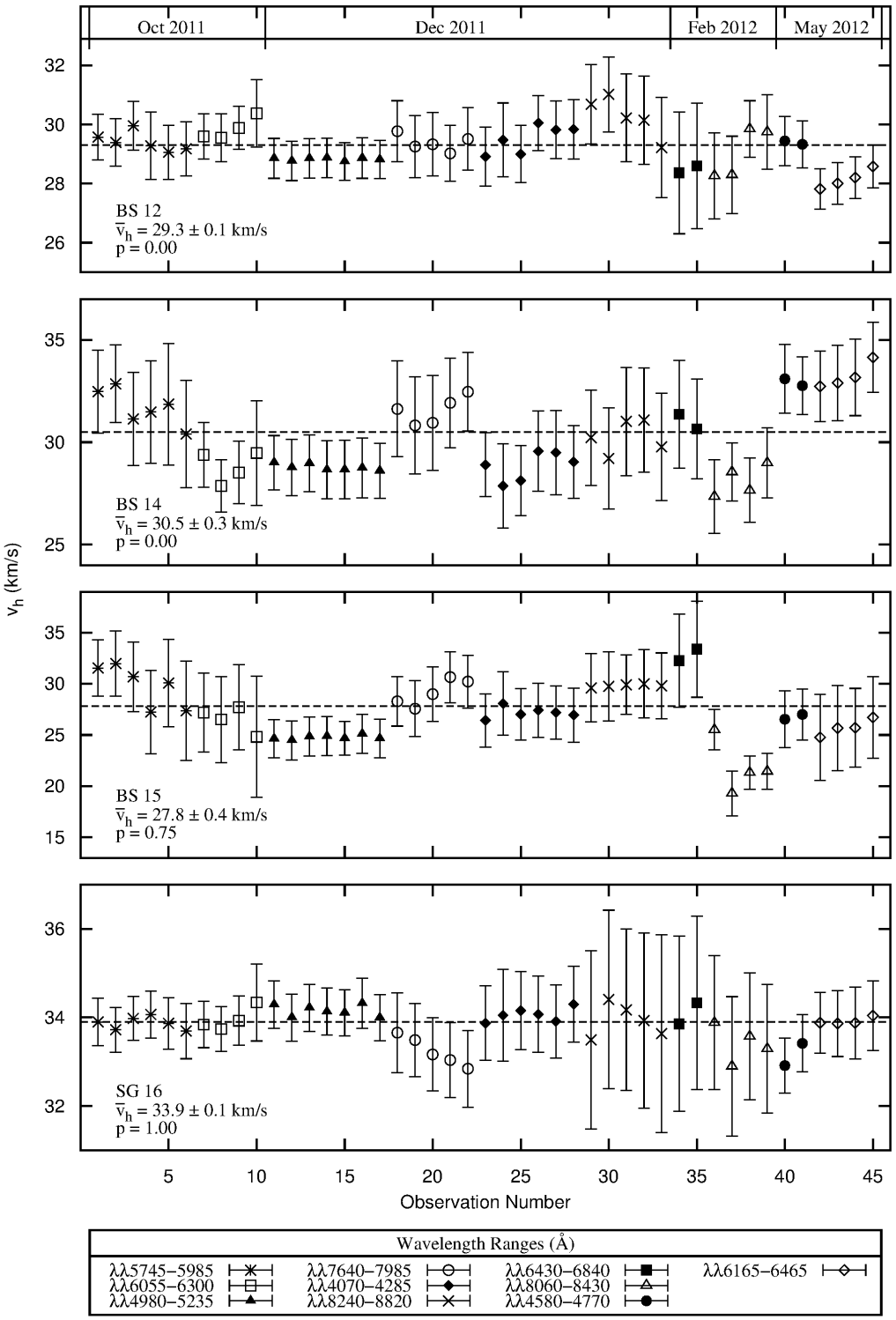

Figure 6: Radial Velocity Plots for BS12, BS14, BS15 and SG16. Note that for stars that exhibit variable radial velocity measurements, the mean value computed in the present work is not representative of a systemic radial velocity for the binary system. It is simply an average of the radial velocity measurements computed.

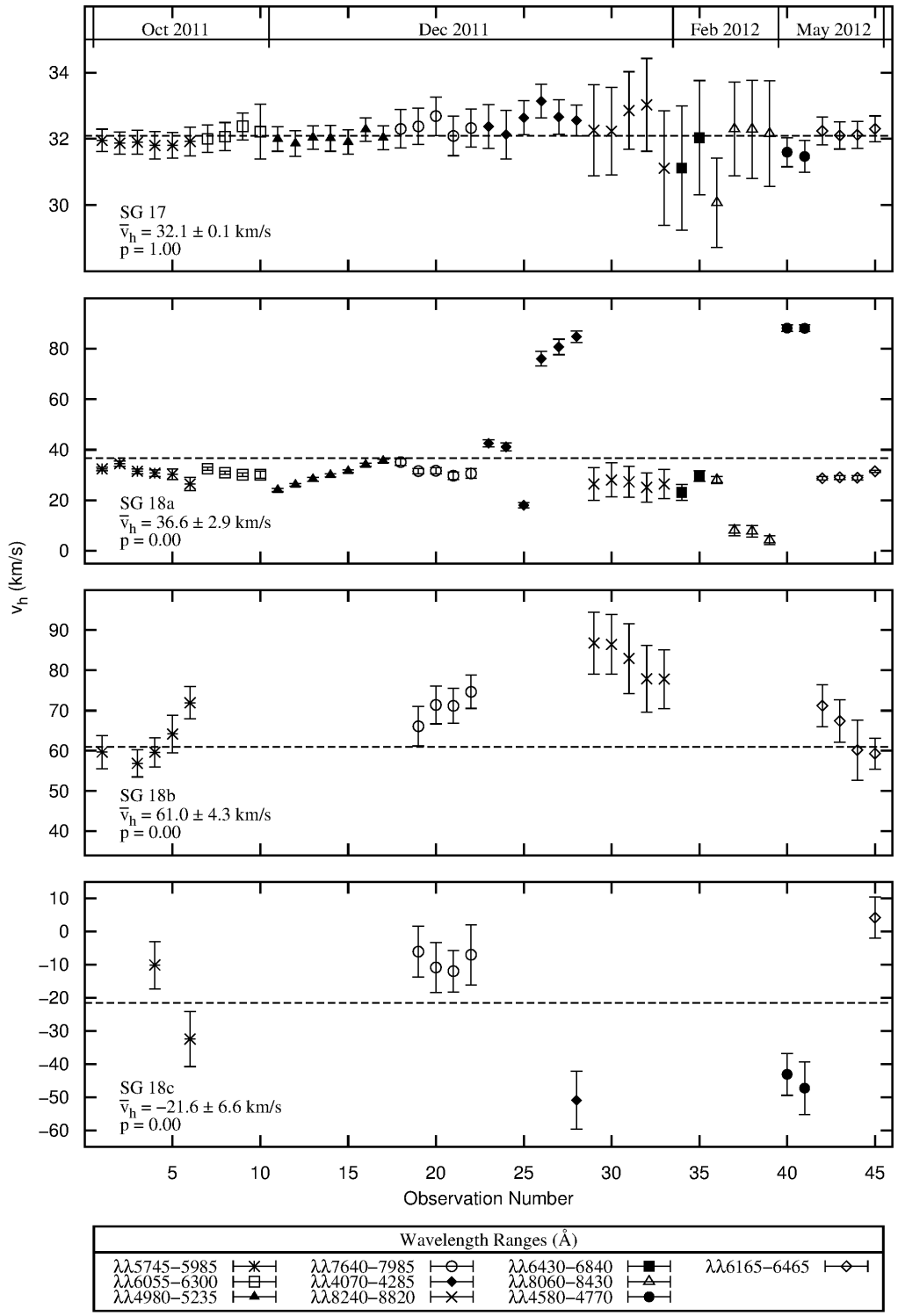

Figure 7: Radial Velocity Plots for SG17, SG18a, SG18b and SG18c. Note that for stars that exhibit variable radial velocity measurements, the mean value computed in the present work is not representative of a systemic radial velocity for the binary system. It is simply an average of the radial velocity measurements computed.

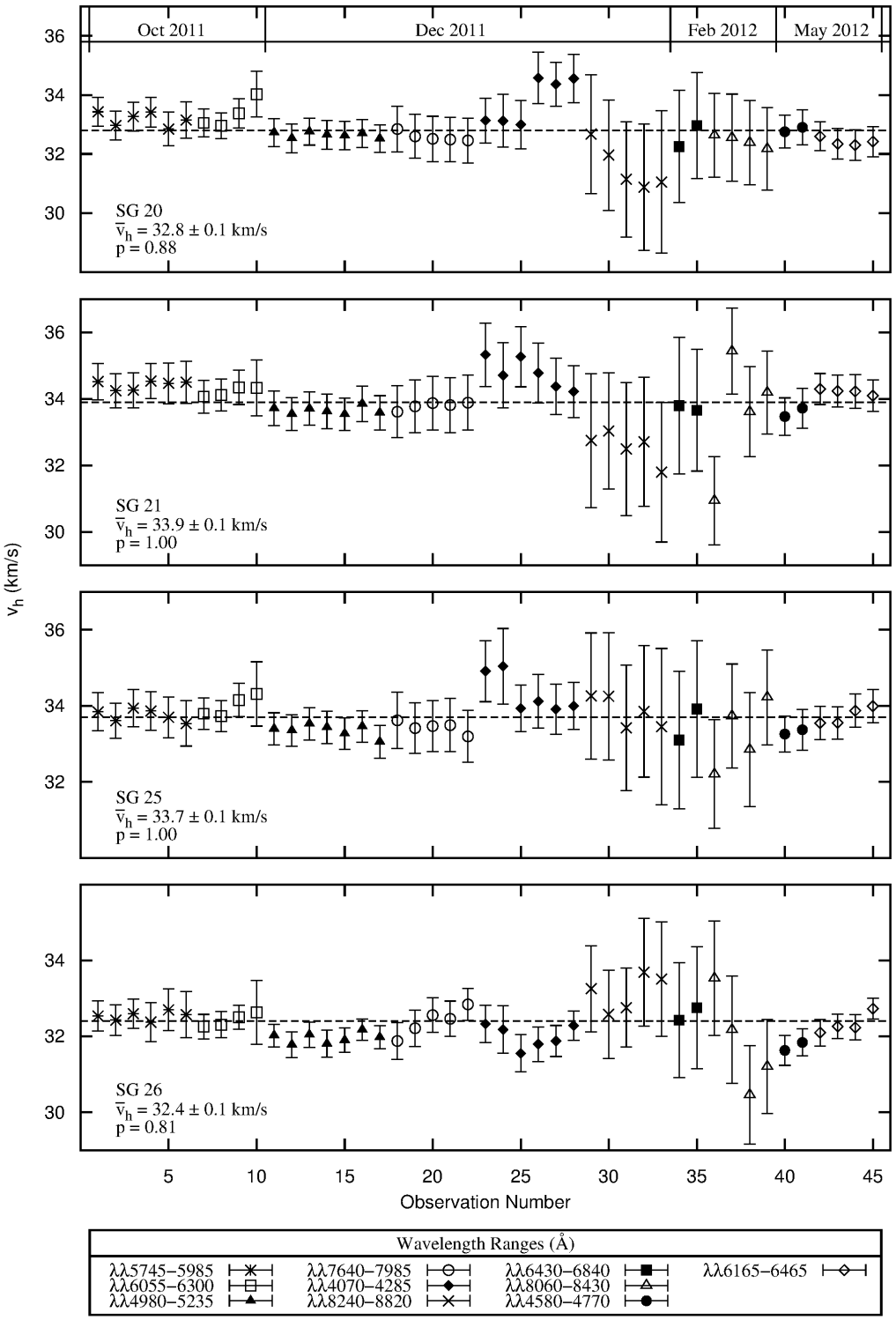

Figure 8: Radial Velocity Plots for SG20, SG21, SG25 and SG26. Note that for stars that exhibit variable radial velocity measurements, the mean value computed in the present work is not representative of a systemic radial velocity for the binary system. It is simply an average of the radial velocity measurements computed.

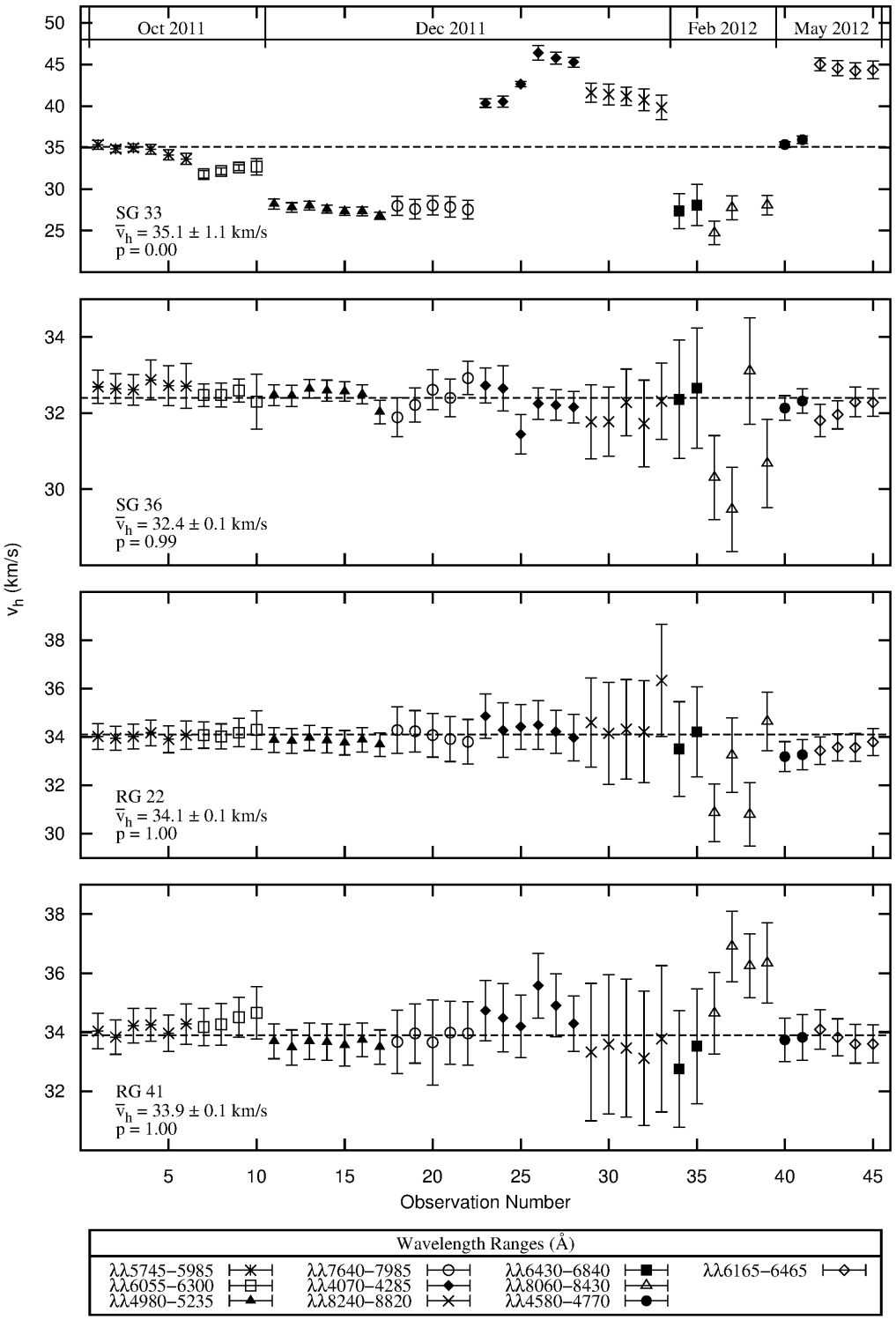

Figure 9: Radial Velocity Plots for SG33, SG36, RG22 and RG41. Note that for stars that exhibit variable radial velocity measurements, the mean value computed in the present work is not representative of a systemic radial velocity for the binary system. It is simply an average of the radial velocity measurements computed.

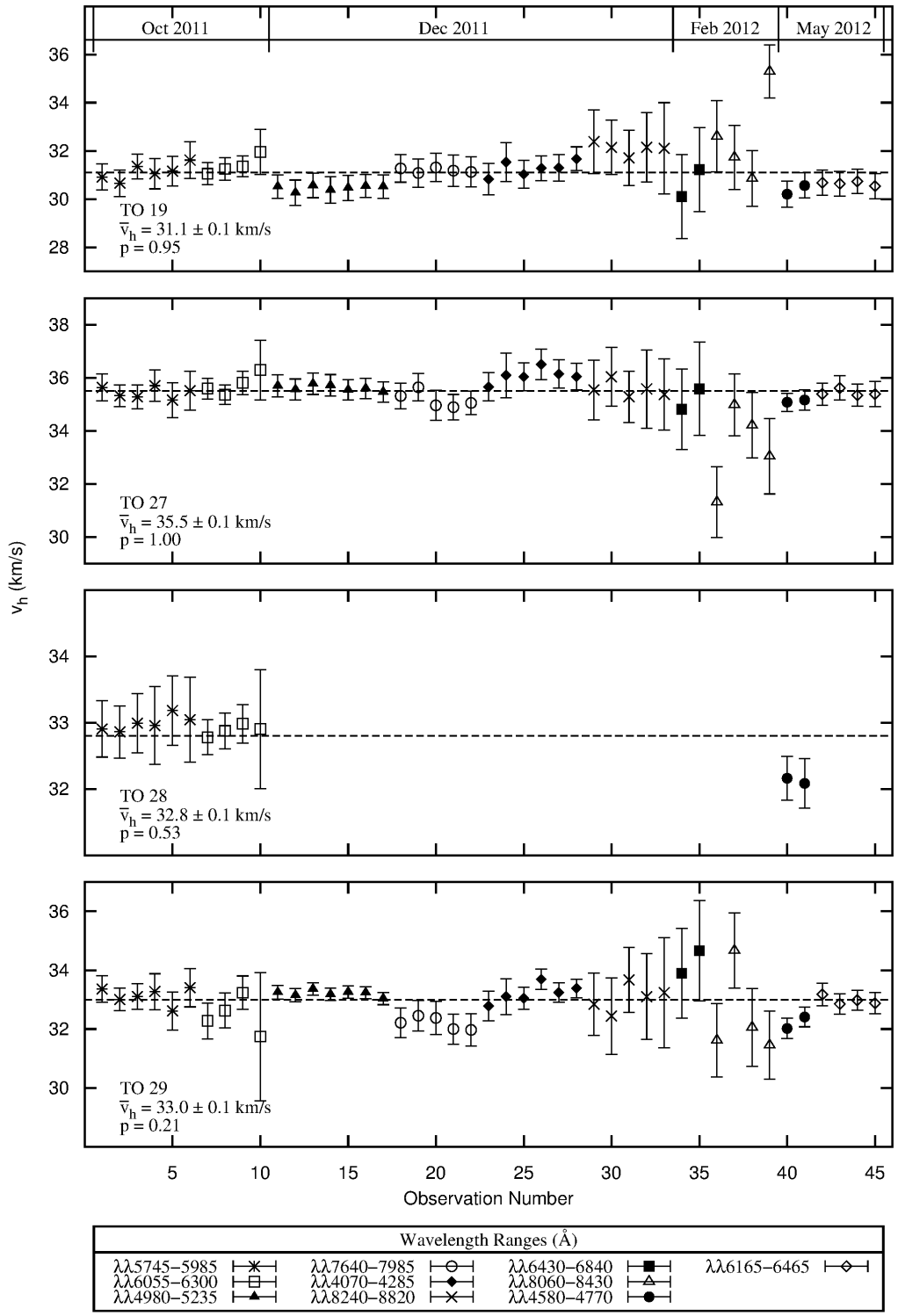

Figure 10: Radial Velocity Plots for TO19, TO27, TO28 and TO29. Note that for stars that exhibit variable radial velocity measurements, the mean value computed in the present work is not representative of a systemic radial velocity for the binary system. It is simply an average of the radial velocity measurements computed.

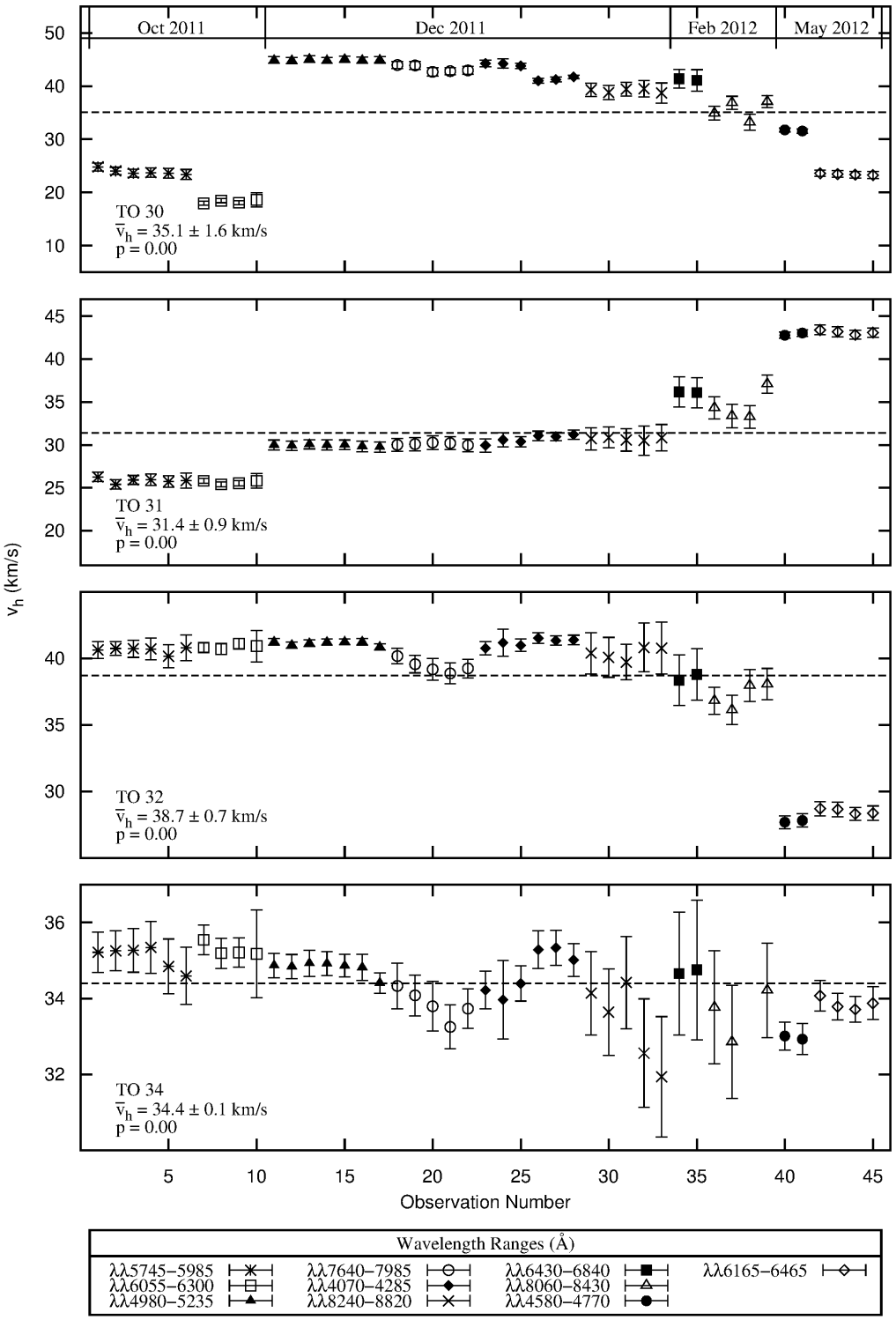

Figure 11: Radial Velocity Plots for TO30, TO 31, TO32 and TO34. Note that for stars that exhibit variable radial velocity measurements, the mean value computed in the present work is not representative of a systemic radial velocity for the binary system. It is simply an average of the radial velocity measurements computed.

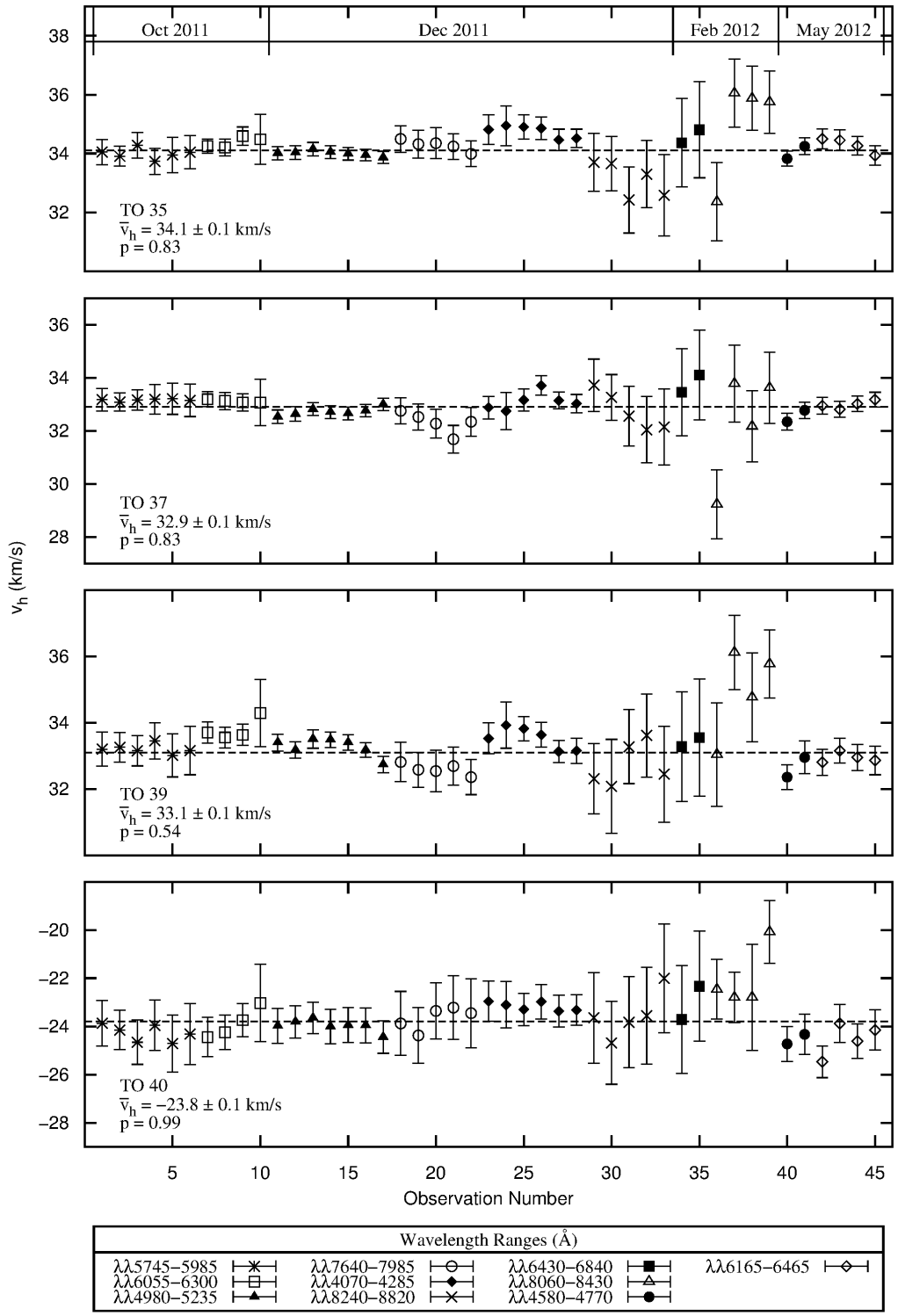

Figure 12: Radial Velocity Plots for TO35, TO37, TO39 and TO40. Note that for stars that exhibit variable radial velocity measurements, the mean value computed in the present work is not representative of a systemic radial velocity for the binary system. It is simply an average of the radial velocity measurements computed.

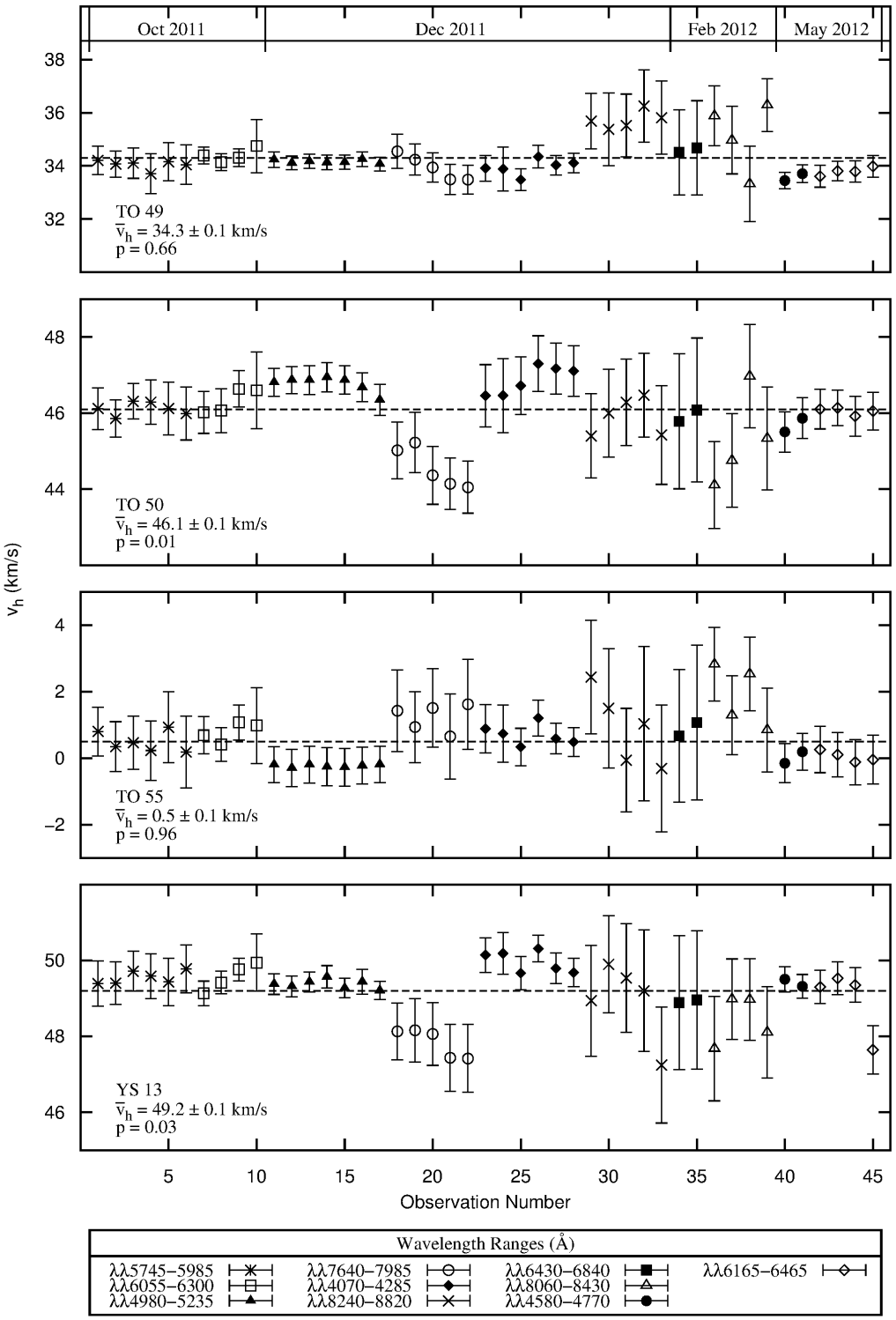

Figure 13: Radial Velocity Plots for TO49, TO50, TO55 and YS13. Note that for stars that exhibit variable radial velocity measurements, the mean value computed in the present work is not representative of a systemic radial velocity for the binary system. It is simply an average of the radial velocity measurements computed.

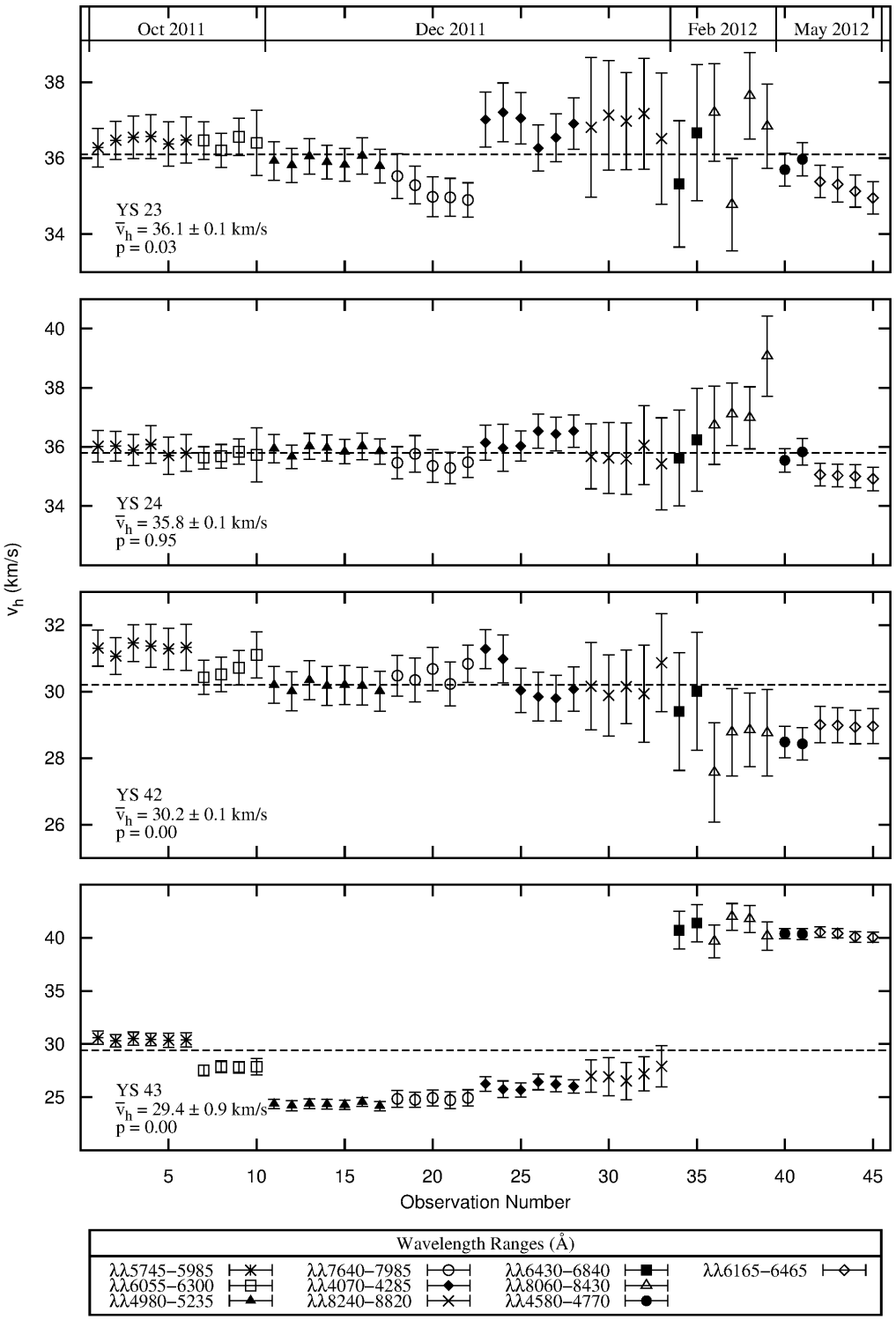

Figure 14: Radial Velocity Plots for YS23, YS24, YS42 and YS43. Note that for stars that exhibit variable radial velocity measurements, the mean value computed in the present work is not representative of a systemic radial velocity for the binary system. It is simply an average of the radial velocity measurements computed.

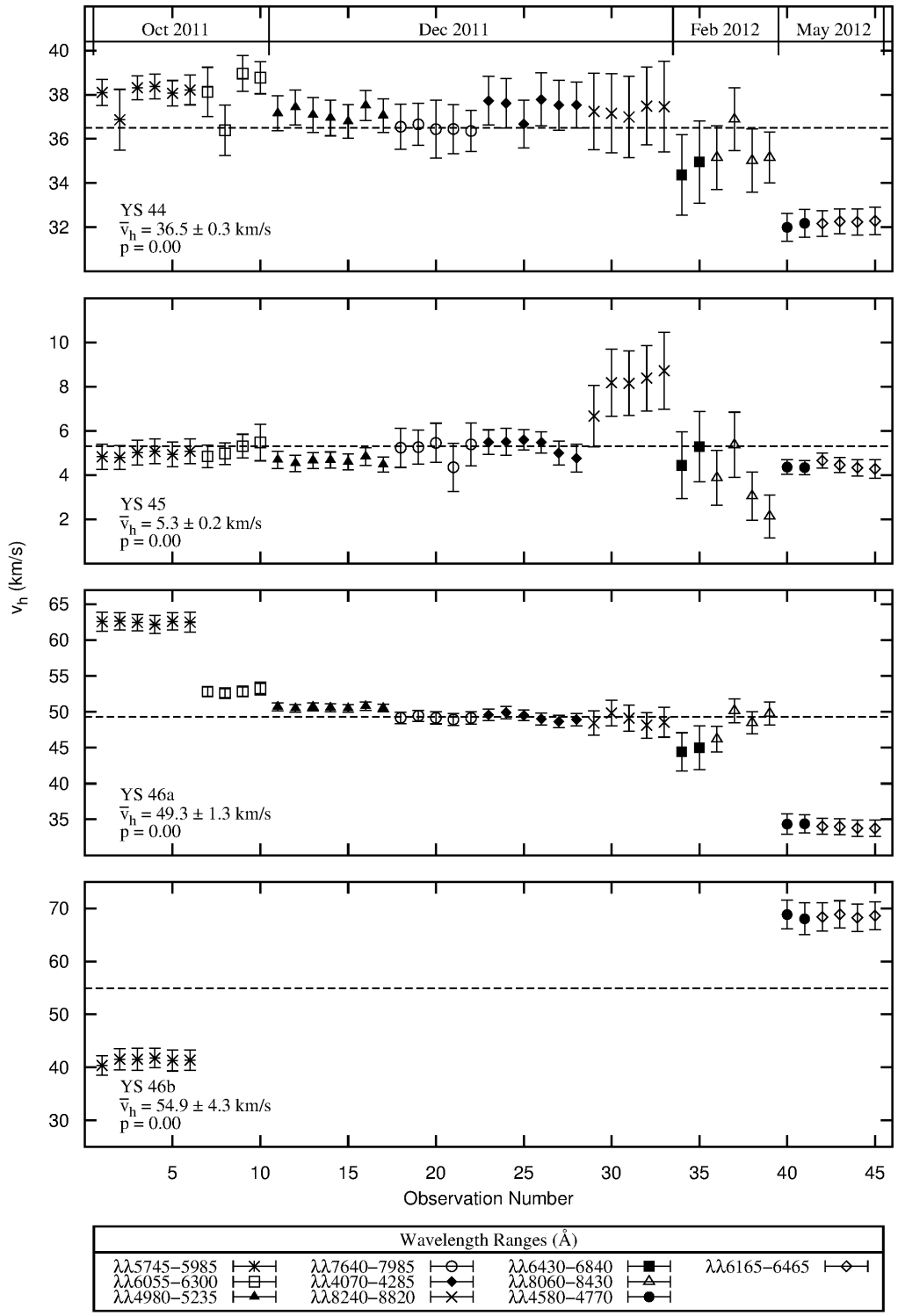

Figure 15: Radial Velocity Plots for YS44, YS45, YS46a and YS46b. Note that for stars that exhibit variable radial velocity measurements, the mean value computed in the present work is not representative of a systemic radial velocity for the binary system. It is simply an average of the radial velocity measurements computed.

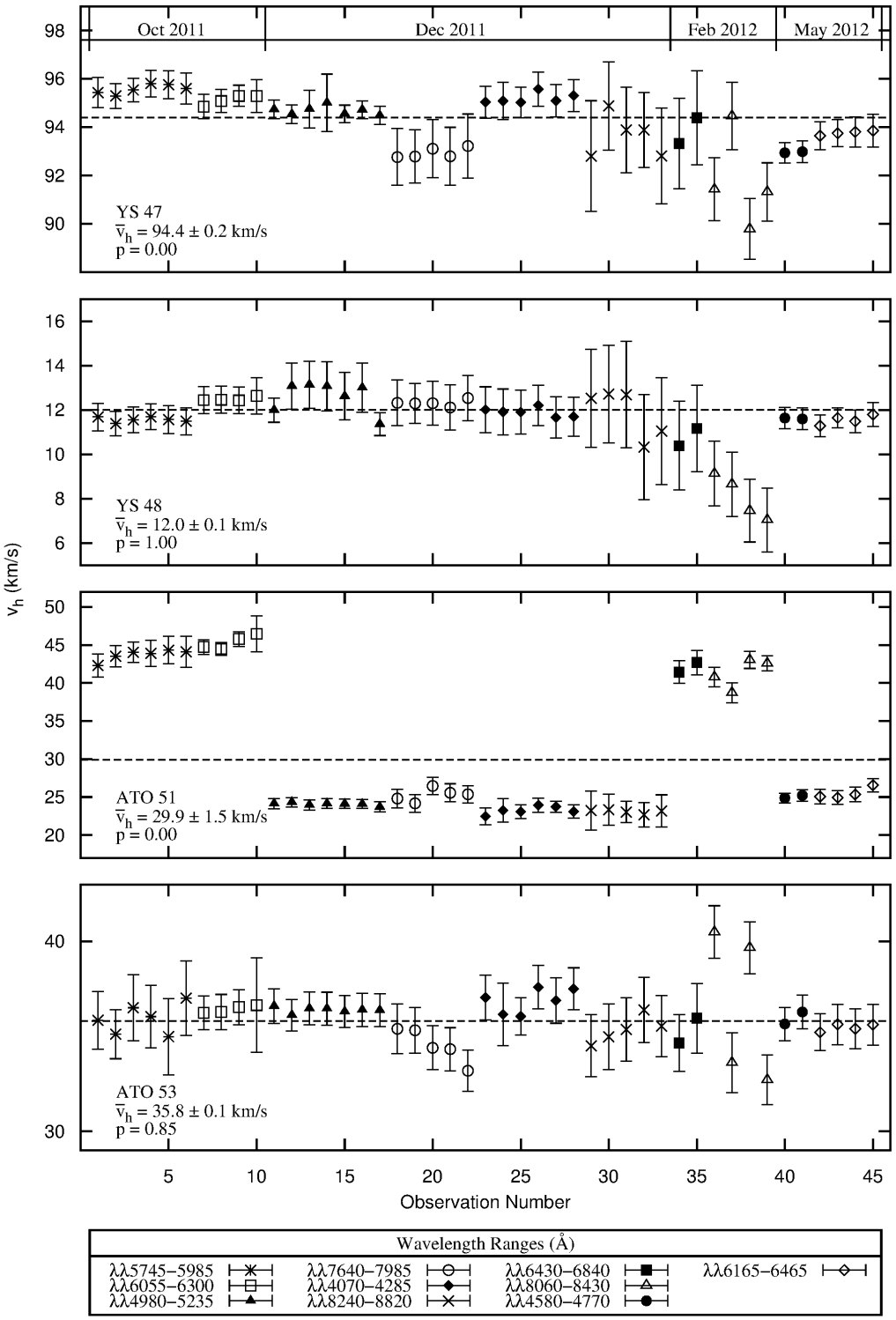

Figure 16: Radial Velocity Plots for YS47, YS48, ATO51 and ATO53. Note that for stars that exhibit variable radial velocity measurements, the mean value computed in the present work is not representative of a systemic radial velocity for the binary system. It is simply an average of the radial velocity measurements computed.

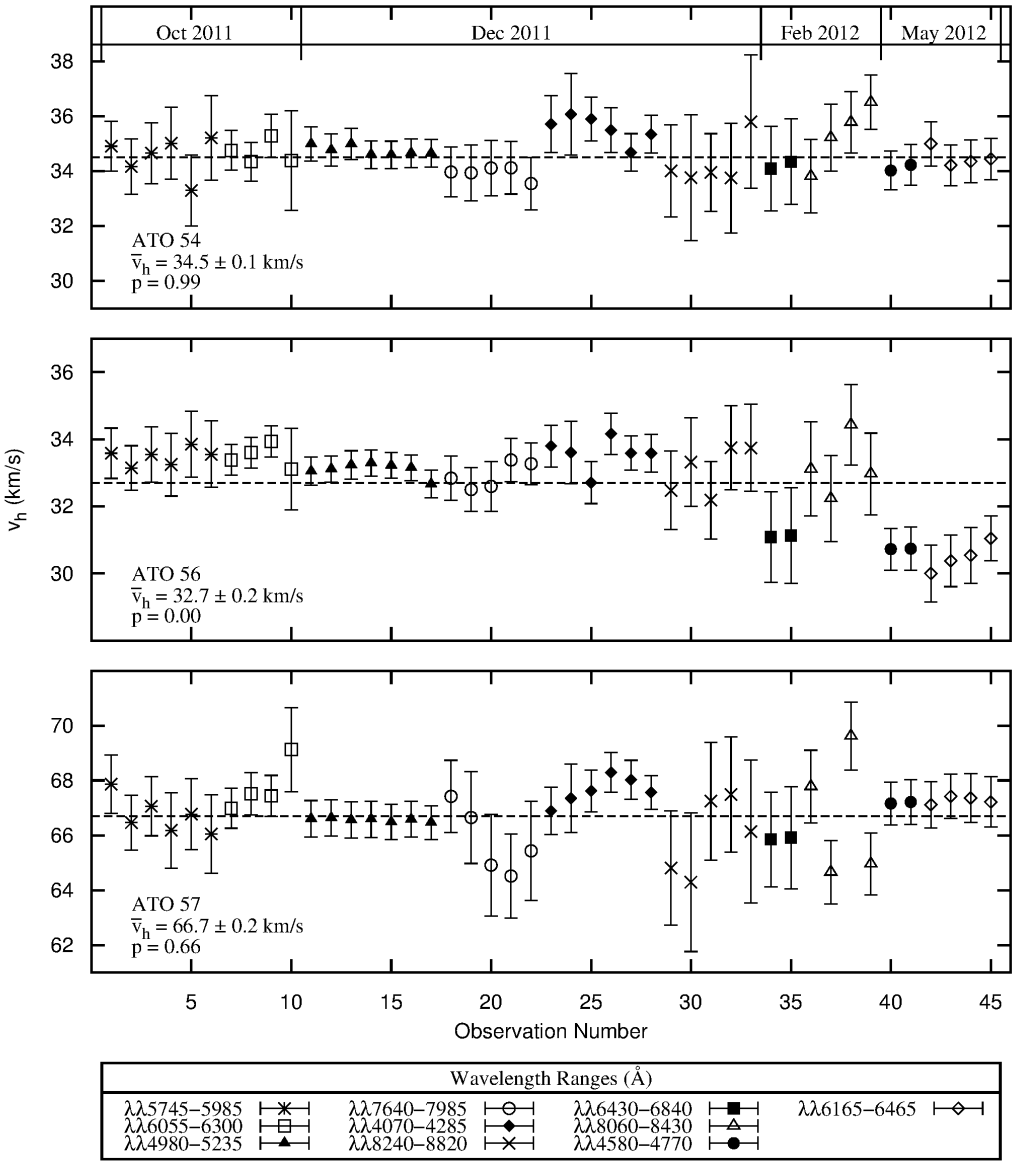

Figure 17: Radial Velocity Plots for ATO54, ATO56 and ATO 57. Note that for stars that exhibit variable radial velocity measurements, the mean value computed in the present work is not representative of a systemic radial velocity for the binary system. It is simply an average of the radial velocity measurements computed.

Appendix C Abundance Analysis Data

Table 1: Abundance Sensitivities to Parameter Changes

		$\frac{\Delta[X/H]}{\Delta T_{\rm eff}}$ $(\frac{\rm dex}{\rm K})$		$\frac{\Delta[X/H]}{\Delta \log(g)}$ $(\frac{\rm dex}{\rm dex})$		$\frac{\Delta[X/H]}{\Delta \xi_{\rm t}}$ $(\frac{\rm dex}{\rm km/s})$	
Star	Ion	+	−	+	−	+	−
TO37							
	[FeI/H]	0.0007	0.0008	-0.07	-0.06	-0.20	-0.25
	[FeII/H]	-0.0002	-0.0002	0.40	0.38	-0.25	-0.30
	[NiI/H]	0.0007	0.0007	-0.03	-0.02	-0.15	-0.15
	[CrI/H]	0.0009	0.0011	-0.10	-0.04	-0.30	-0.35
	[BaII/H]	0.0004	0.0003	0.23	0.28	-0.60	-0.65
	[YII/H]	0.0002	0.0002	0.40	0.40	-0.35	-0.40
	[NaI/H]	0.0005	0.0005	-0.07	-0.04	-0.05	-0.05
	[TiI/H]	0.0009	0.0009	-0.07	-0.02	-0.10	-0.05
	[TiII/H]	0.0002	0.0001	0.37	0.36	-0.40	-0.45
	[CaI/H]	0.0007	0.0008	-0.27	-0.20	-0.30	-0.25
	[SiI/H]	0.0004	0.0003	-0.10	-0.06	-0.10	-0.10
	[CI/H]	-0.0006	-0.0006	0.30	0.30	-0.05	0.00
	[OI/H]	-0.0008	-0.0008	0.23	0.22	-0.15	-0.15
	[AlI/H]	0.0004	0.0003	-0.10	-0.10	-0.05	-0.05
SG17							
	[FeI/H]	0.0007	0.0008	-0.10	-0.06	-0.35	-0.30
	[FeII/H]	-0.0004	-0.0005	0.43	0.44	-0.30	-0.30
	[NiI/H]	0.0007	0.0006	0.00	0.02	-0.30	-0.30
	[CrI/H]	0.0011	0.0012	-0.13	-0.10	-0.50	-0.45
	[BaII/H]	0.0003	0.0002	0.23	0.26	-0.65	-0.65
	[YII/H]	0.0001	-0.0013	1.33	-0.12	0.90	-1.90
	[NaI/H]	0.0006	0.0005	-0.07	-0.06	-0.10	-0.10
	[TiI/H]	0.0010	0.0011	-0.03	-0.04	-0.15	-0.15
	[TiII/H]	0.0001	0.0000	0.37	0.36	-0.60	-0.65
	[CaI/H]	0.0010	0.0009	-0.17	-0.18	-0.20	-0.25
	[SiI/H]	0.0002	0.0001	-0.03	-0.02	-0.10	-0.10
	[CI/H]	-0.0006	-0.0009	0.33	0.32	0.00	-0.05
	[OI/H]	-0.0009	-0.0012	0.30	0.34	-0.15	-0.10
	[AlI/H]	0.0004	0.0005	-0.17	-0.06	-0.15	0.00
SG16							
	[FeI/H]	0.0006	0.0005	0.00	0.00	-0.30	-0.35
	[FeII/H]	-0.0007	-0.0010	0.50	0.50	-0.15	-0.25
	[NiI/H]	0.0004	0.0001	0.13	0.12	-0.25	-0.35
	[CrI/H]	0.0013	0.0013	-0.13	-0.12	-0.40	-0.40
	[BaII/H]	0.0002	0.0002	0.23	0.28	-0.60	-0.60
	[YII/H]	0.0001	-0.0030	2.37	-0.78	2.70	-3.35

Abundance Sensitivities to Parameter Changes 1 – Continued

Star	Ion	$\frac{\Delta[X/H]}{\Delta T_{\rm eff}}$ $(\frac{\rm dex}{\rm K})$ +	−	$\frac{\Delta[X/H]}{\Delta \log(g)}$ $(\frac{\rm dex}{\rm dex})$ +	−	$\frac{\Delta[X/H]}{\Delta \xi_{\rm t}}$ $(\frac{\rm dex}{\rm km/s})$ +	−
	[NaI/H]	0.0006	0.0007	-0.10	-0.08	-0.15	-0.20
	[TiI/H]	0.0013	0.0013	-0.03	-0.04	-0.30	-0.35
	[TiII/H]	0.0000	0.0000	0.37	0.42	-0.40	-0.45
	[CaI/H]	0.0011	0.0012	-0.20	-0.20	-0.25	-0.35
	[SiI/H]	-0.0002	-0.0004	0.10	0.10	-0.10	-0.10
	[CI/H]	-0.0009	-0.0011	0.30	0.36	-0.05	0.00
	[OI/H]	-0.0013	-0.0015	0.30	0.38	-0.05	-0.10
	[AlI/H]	0.0005	0.0004	-0.13	-0.12	-0.10	-0.15
SG41							
	[FeI/H]	0.0007	0.0005	0.07	0.08	-0.40	-0.40
	[FeII/H]	-0.0009	-0.0012	0.53	0.52	-0.20	-0.25
	[NiI/H]	0.0004	0.0002	0.17	0.16	-0.30	-0.30
	[CrI/H]	0.0016	0.0016	-0.03	-0.06	-0.60	-0.65
	[BaII/H]	0.0002	0.0003	0.37	0.40	-0.65	-0.75
	[YII/H]	0.0000	0.0023	-1.07	1.32	-2.45	1.95
	[NaI/H]	0.0008	0.0009	-0.07	-0.04	-0.20	-0.20
	[TiI/H]	0.0015	0.0016	-0.03	0.00	-0.30	-0.35
	[TiII/H]	0.0000	-0.0001	0.40	0.42	-0.45	-0.50
	[CaI/H]	0.0014	0.0015	-0.13	-0.10	-0.40	-0.40
	[SiI/H]	-0.0002	-0.0004	0.17	0.18	-0.15	-0.15
	[CI/H]						
	[OI/H]	-0.0016	-0.0018	0.40	0.44	-0.10	-0.10
	[AlI/H]	0.0006	0.0006	-0.07	-0.04	-0.20	-0.15
YS42							
	[FeI/H]	0.0008	0.0007	-0.03	-0.04	-0.10	-0.20
	[FeII/H]	-0.0003	-0.0003	0.43	0.42	-0.25	-0.25
	[NiI/H]	0.0007	0.0008	0.00	0.00	-0.15	-0.10
	[CrI/H]	0.0011	0.0011	-0.03	-0.06	-0.25	-0.30
	[BaII/H]	0.0004	0.0002	0.37	0.34	-0.50	-0.60
	[YII/H]	0.0002	0.0002	0.40	0.40	-0.25	-0.30
	[NaI/H]	0.0006	0.0005	-0.03	-0.04	-0.05	-0.10
	[TiI/H]	0.0010	0.0011	-0.07	-0.02	-0.05	-0.05
	[TiII/H]	0.0002	0.0001	0.40	0.40	-0.30	-0.35
	[CaI/H]	0.0008	0.0009	-0.17	-0.10	-0.30	-0.30
	[SiI/H]	0.0004	0.0003	0.00	-0.02	-0.10	-0.10
	[CI/H]	-0.0007	-0.0008	0.33	0.34	-0.05	0.00
	[OI/H]	-0.0009	-0.0011	0.30	0.32	-0.20	-0.20
	[AlI/H]	0.0004	0.0004	-0.07	-0.06	-0.05	-0.10

Table 2: Equivalent Widths Part I: SGs

				Equivalent Width								
Ion	WL	EP	log(gf)	Solar	SG16	SG17	SG20	SG21	SG25	SG26	SG33	SG36
Fe I:												
	5752.032	4.55	-1.18	56.6	75.7	62.5	69.9	67.7	70.0	46.6	45.4	63.1
	5775.081	4.22	-1.30	57.9	75.8	63.7	71.9	91.8	80.4	47.7		58.1
	5778.450	2.59	-3.48	21.0	58.2	24.6	44.2	54.3	49.7		19.0	22.2
	5905.672	4.65	-0.73	64.3	79.1	66.3	75.5		78.5	55.9	43.3	44.9
	5916.247	2.45	-2.99	70.4		67.6	92.7		90.9	53.6	58.8	
	5927.786	4.65	-1.09	45.5	58.8	49.7	56.8	56.1	61.8	39.3	30.3	42.3
	5929.667	4.55	-1.41	43.8	61.2	37.1	63.4		56.6	31.8	49.2	42.7
	5930.173	4.65	-0.23	86.5	106.9	96.8	106.4	97.4	89.3	78.5	91.0	84.5
	5934.653	3.93	-1.17	74.3	105.7	75.8	88.7	100.6	104.6	73.9	71.9	75.4
	5969.559	4.28	-2.73	4.2								
	6055.992	4.73	-0.46	76.0	108.9	84.1	89.8	86.1	83.5	75.9	66.9	78.3
	6065.482	2.61	-1.53	114.4	177.7	119.3	167.2	172.0	155.1	114.7	117.8	114.3
	6078.491	4.80	-0.32	81.0	117.2	91.9	96.6	102.5	102.3	78.1	101.0	93.6
	6078.999	4.65	-1.12	44.1	75.4	43.9	65.7	71.9	64.0	40.7		41.0
	6083.660	3.88	-3.50	3.5								
	6085.259	2.76	-3.10	39.8	81.6	47.3	80.5	79.2	72.2	38.9	27.0	31.7
	6098.245	4.56	-1.88	21.0			38.0		41.5	20.1		24.9
	6102.171	4.83	-0.52	82.3	90.1	96.5	115.1	118.5	121.7	73.5		80.1
	6105.131	4.55	-2.05	10.4								
	6120.249	0.91	-5.96	7.6	27.1		30.1	24.7	21.1			
	6127.907	4.14	-1.40	49.9	90.9	66.3	86.5	88.3	81.6	52.6	39.3	44.7
	6151.617	2.18	-3.30	48.9	78.4	61.0	83.7	75.1	77.4	39.8	43.1	44.3
	6157.728	4.08	-1.26	60.1	95.3	70.6	94.5	96.3	82.4	68.7	77.1	68.3
	6159.368	4.61	-1.97	13.0								
	6165.360	4.14	-1.47	46.0	70.5	52.3	69.4	57.9	64.3	38.3	42.8	42.7
	6170.504	4.79	-0.44	80.7	138.3	92.4	130.7	119.5	127.5	75.1	66.9	80.4
	6173.336	2.22	-2.88	66.8	107.0	78.3	99.9	97.6	94.0	70.1	51.0	67.9
	6187.987	3.94	-1.72	42.9	66.7	61.1	68.3	77.9	69.9	49.2	41.9	40.9
	6213.429	2.22	-2.48	79.5	140.7	92.0	122.2	127.1	125.8	82.8	80.5	86.7
	6219.280	2.20	-2.43	88.7	128.8	104.1	129.4	125.8	118.3	81.9	92.4	92.0
	6226.730	3.88	-2.22	29.2	59.0	45.4	60.9	61.8	58.9	30.7	31.5	27.0
	6232.641	3.65	-1.22	85.7	129.1	97.2	125.6	125.8	113.2	75.2	79.2	84.8
	6240.645	2.22	-3.23	54.2	118.7	73.3	109.5	98.2	96.6	46.7		52.4
	6246.317	3.60	-0.73	124.5	158.9	124.3	147.5	154.5	149.3	101.9	115.3	109.5
	6252.554	2.40	-1.69	115.2	169.8	129.9	157.9	168.3	150.2	114.1	110.9	113.3
	6256.360	2.45	-2.41	99.2	173.0	113.2	145.3	155.0	155.8	95.8		100.6
	6265.130	2.17	-2.55	88.0	138.8	103.9	124.9		119.0	82.5	84.1	88.1
	6271.280	3.33	-2.72	26.8	63.1	36.2	64.1	56.0	54.2	27.0	27.4	27.0
	6290.974	4.73	-0.78	70.7	111.7	87.1	108.4	112.9	112.2	75.0	53.9	74.3
	6293.924	4.83	-1.72	18.6			22.0		40.1			
	6322.685	2.59	-2.43	79.3	133.4	103.9	106.2	123.8	116.8	88.5	83.5	87.1
	6335.328	2.20	-2.18	103.6	145.6	107.0	131.0	137.3		92.6	103.5	96.0
	6336.820	3.68	-0.91	107.6	153.3	104.7	134.6	140.4	135.9	94.7		98.8
	6344.148	2.43	-2.92	68.3	141.4	89.4		115.8	116.9	63.8	73.8	70.3
	6380.743	4.19	-1.38	50.3	74.5	63.5	73.7	56.5	69.6	47.8	55.7	46.9
	6392.538	2.28	-4.03	18.1	62.3	26.1	53.1	57.6	49.0			20.3
	6393.612	2.43	-1.57	126.4	191.1	141.6	177.6	186.5	176.8	120.0	118.2	124.8
	6408.018	3.69	-1.02	108.1	158.3	112.4	153.8	154.5	150.2	99.2	110.0	99.1
	6411.647	3.65	-0.59	135.1	175.2	137.3	166.9	163.7		115.5	116.9	
	6469.193	4.83	-0.77	67.3	107.4	79.0	102.6		106.0	68.5	68.6	79.9

Equivalent Widths Part I: SGs 2 – Continued

				Equivalent Width								
Ion	WL	EP	log(gf)	Solar	SG16	SG17	SG20	SG21	SG25	SG26	SG33	SG36
	6498.945	0.96	-4.70	30.7			72.1		68.0			38.5
	6533.940	4.56	-1.38	53.2	63.4	56.7	62.0	84.1	87.6			53.1
	6584.575	5.39	-1.34	10.1								
	6591.313	4.59	-2.07	25.3						24.3	29.6	32.5
	6592.913	2.73	-1.47	138.1	212.2		188.0	209.3	197.3	134.5	157.2	141.5
	6593.870	2.43	-2.42	91.3	141.6	102.4	130.6	152.7	132.8	92.0		94.0
	6597.557	4.79	-1.07	44.6	74.5	58.8	68.3	72.3	72.6	48.9	50.0	59.5
	6608.024	2.28	-4.03	18.5	55.9		53.8	61.5	58.4	23.7		18.6
	6627.540	4.55	-1.68	31.2	60.5	44.2	52.0	70.5	67.1	27.1	35.1	49.3
	6646.932	2.61	-3.99	12.8	46.4	18.8	40.0	43.7	43.3			
	6653.850	4.15	-2.52	22.8					43.6		28.5	32.6
	6667.417	2.45	-4.40	15.0	62.8		47.5	63.4	40.1			
	6667.711	4.58	-2.11	19.0			46.0					
	6703.567	2.76	-3.16	38.4	78.1	61.8	67.8	73.2	69.9	36.8	47.9	30.7
	6705.101	4.61	-1.39	51.7	80.7	61.2	72.8	64.6	69.0	53.2	61.2	
	6710.316	1.49	-4.88	16.7	76.7		53.7	59.2	52.3	16.0		
	6713.745	4.79	-1.52	17.8	53.9		35.0				21.4	28.4
	6715.383	4.61	-1.64	29.0	66.0		56.2	64.3	57.1	33.9	35.7	36.0
	6716.222	4.58	-1.92	18.6	57.3		48.6		53.6			
	6725.353	4.10	-2.30	18.9			35.2		43.8			
	6726.666	4.61	-1.13	50.3	73.7	60.6	70.8	78.1	76.0	45.7	69.1	54.0
	6733.151	4.64	-1.58	29.3	48.6		45.7	53.4	53.8		34.3	38.8
	6739.520	1.56	-4.79	13.7	50.4		45.5	66.1	53.6		10.4	
	6745.090	4.58	-2.16	18.1								
	6745.957	4.08	-2.77	20.1								
	6746.953	2.61	-4.35	14.1	25.8			33.8				
	6750.150	2.42	-2.62	74.3	107.7	91.2	108.4	107.6	102.1	79.1	76.1	75.6
	6752.716	4.64	-1.30	38.9		61.4	71.1	73.9	73.0	52.8		46.5
	6753.464	4.56	-2.29	13.9								
	6777.408	4.19	-2.82	19.6	50.7		39.7	57.3		25.9	21.3	
	6783.704	2.59	-3.98	33.0		39.9	89.8	78.4	82.4			
	6786.856	4.19	-2.07	31.4	77.4		49.8	64.9		42.7	42.9	46.9
	6793.259	4.08	-2.33	16.1	58.5							
	7802.473	5.09	-1.52	16.3								
	7807.909	4.99	-0.54	68.4	94.9	67.3	83.9	84.3	87.1	59.8	60.4	54.7
	7820.803	4.29	-2.64	9.7								
	7844.555	4.83	-1.81	12.8								
	7879.748	5.03	-1.65	28.3					50.8		41.2	
Fe II:												
	6084.110	3.20	-3.80	21.3	41.0	30.5	25.9	32.9	35.2	39.9		36.0
	6149.249	3.89	-2.88	40.4	48.4	56.7	52.9	45.9	53.5	60.6	53.4	58.1
	6238.392	3.89	-2.75	44.3		70.2	57.0	53.8	58.5	66.5	70.7	68.8
	6247.557	3.89	-2.44	56.8	55.5	73.5	51.4	64.6	69.2	81.2	76.9	83.5
	6369.462	2.89	-4.23	16.9	24.2	34.8			40.2	30.1	37.9	40.4
	6416.919	3.89	-2.88	38.2	43.3	58.0	42.5	42.3	50.5	59.8	66.9	56.6
	6456.380	3.90	-2.07	70.9	67.6	88.6	66.9	72.2	89.1	102.3		108.5
Ni I:												
	6086.280	4.26	-0.51	46.2	70.0	55.4	62.8	68.6	67.8	42.9	33.1	39.2
	6175.370	4.09	-0.53	56.8	69.8		71.8	71.2	71.4	51.5	50.0	57.8
	6204.605	4.09	-1.10	25.4	43.2	36.8	46.2	48.9	38.8	25.0		24.0
	6327.600	1.68	-3.23	39.6	87.6	61.6	77.1	78.1	75.5	30.4	17.4	35.2
	6378.260	4.15	-1.00	33.6	43.4	46.7	56.1	61.0	60.9	33.6	19.2	34.1

Equivalent Widths Part I: SGs 2 – Continued

				Equivalent Width								
Ion	WL	EP	log(gf)	Solar	SG16	SG17	SG20	SG21	SG25	SG26	SG33	SG36
	6643.640	1.68	-2.01	98.3	140.6	109.1	133.4	138.2	136.4	89.8	61.8	92.2
	6772.320	3.66	-0.98	49.7	77.8	66.9	69.2	82.5	67.6	54.0	34.9	52.9
Cr I:												
	4616.120	0.98	-1.19	100.6	149.8	114.6	140.1	138.4	123.5	103.0	92.5	94.3
	4651.290	0.98	-1.46	85.2		98.0	118.7	123.0	115.1	87.0	70.3	78.0
	6330.100	0.94	-2.99	30.2	70.2	38.7	64.7	65.0	54.5	15.7	14.5	19.4
Ba II:												
	5853.690	0.60	-1.00	62.3	90.2	85.0	85.9	80.4	85.1	81.3	75.4	80.5
	6141.730	0.70	-0.07	122.6	154.7	144.8	147.9	147.2	150.8	134.8	142.7	130.2
Y II:												
	5087.420	1.08	-0.17	49.4	61.4	67.3	65.4	58.5	65.9	62.9	48.1	66.5
Na I:												
	6154.230	2.10	-1.53	41.0	69.7	48.8	60.4	69.1	62.2	32.7	26.0	34.8
	6160.750	2.10	-1.23	63.0	96.5	72.5	84.2	95.2	94.8	50.1		53.2
Ti I:												
	5978.541	1.87	-0.50	27.5	71.2	35.4	68.0	69.8	53.3		13.5	
	6064.626	1.05	-1.94	15.5	50.6	18.9	47.2	58.9	43.6		7.5	
	6126.216	1.07	-1.43	24.1	70.3	38.6	64.9	70.5	50.9	21.1	9.0	19.4
	6258.102	1.44	-0.35	56.0	104.1	69.8	100.0	114.7	86.2	39.8	28.0	45.5
	6261.098	1.43	-0.48	58.5	107.3	71.3	98.7	109.6	91.8	37.1	35.4	44.7
Ti II:												
	4589.958	1.24	-1.78	75.1	98.6	96.3	88.4	93.4	96.7	103.9	84.2	109.4
	4708.665	1.24	-2.63	45.6	67.3		63.6	72.9	69.2	72.4		60.1
Ca I:												
	6122.226	1.89	-0.32	202.8	282.0	197.5	262.6	257.3	250.8	155.8	177.8	162.2
	6166.439	2.52	-1.14	66.8	103.4	78.7	96.1	94.6	94.6	62.1	56.1	62.4
	6464.680	2.52	-2.53	12.0								
	6572.800	0.00	-4.28	39.0	101.1	54.7	90.3	86.5	86.6	35.1		34.2
Si I:												
	6142.480	5.62	-1.54	42.6	52.0	50.2	45.0	43.0	50.7	39.2	24.0	41.7
	6145.010	5.62	-1.36	42.8	50.0	50.1	49.0	41.4	53.4	41.1	30.7	44.4
	6155.130	5.62	-0.78	92.4	94.0	95.1	90.9	89.8	100.3	82.4	86.1	89.1
C I:												
	6587.620	8.53	-1.00	17.7	14.6	23.4	12.7	15.3		34.2		32.9
O I:												
	7771.940	9.15	0.37	74.5	42.2	84.1	53.6	49.4	63.7	119.0		119.9
	7774.170	9.15	0.22	63.5	36.8	73.6	42.1	39.5	55.6	106.7		98.4
	7775.390	9.15	0.00	51.7	29.3	64.2	38.6	28.9	45.4	95.5		82.4
Al I:												
	6698.670	3.14	-1.95	30.2	60.2	35.9	51.5	58.8				25.0
	7835.310	4.02	-0.47	59.7	88.2	59.2	78.2	81.7	91.9	45.4		48.2
	7836.130	4.02	-0.31	69.6	98.7	75.2	90.6	93.2	103.6	58.8		51.3

Table 3: Equivalent Widths Part II: RGs and TOs

				Equivalent Widths						
Ion	WL	EP	log(gf)	Solar	RG22	RG41	TO35	TO37	TO0	TO49
Fe I:										
	5752.032	4.55	-1.18	56.6	87.8	80.4	64.0	52.2	49.3	
	5775.081	4.22	-1.30	57.9	84.8	90.1	56.8	50.1	54.2	56.1
	5778.450	2.59	-3.48	21.0	59.1	73.9	11.8	19.3	19.1	
	5905.672	4.65	-0.73	64.3	72.5	84.5	62.7	54.2	54.0	49.9
	5916.247	2.45	-2.99	70.4			47.8	51.9	50.7	55.3
	5927.786	4.65	-1.09	45.5	60.8	64.3	40.1	28.7	26.3	
	5929.667	4.55	-1.41	43.8	66.5	62.6		36.9	36.6	46.5
	5930.173	4.65	-0.23	86.5	106.4	110.9	87.3	89.0		80.1
	5934.653	3.93	-1.17	74.3	106.7	113.4	73.4	67.6	56.2	63.1
	5969.559	4.28	-2.73	4.2						
	6055.992	4.73	-0.46	76.0		102.5		79.2	68.3	75.9
	6065.482	2.61	-1.53	114.4	173.9	196.2	120.3	114.5	115.5	107.6
	6078.491	4.80	-0.32	81.0	108.7	110.2	75.0	90.6	69.7	78.8
	6078.999	4.65	-1.12	44.1	77.9	84.1	51.2		40.6	24.6
	6083.660	3.88	-3.50	3.5						
	6085.259	2.76	-3.10	39.8	93.3	103.2	28.4	22.9	40.3	25.8
	6098.245	4.56	-1.88	21.0			15.5	18.3	17.0	
	6102.171	4.83	-0.52	82.3	116.4	124.9	83.9	86.3	88.8	66.3
	6105.131	4.55	-2.05	10.4			13.4			13.7
	6120.249	0.91	-5.96	7.6	43.2	50.4				
	6127.907	4.14	-1.40	49.9	95.8	106.2	55.0	45.6	49.6	40.6
	6151.617	2.18	-3.30	48.9		97.5	46.0	36.3	45.1	35.0
	6157.728	4.08	-1.26	60.1	104.0	119.5	74.8	63.0	67.7	52.6
	6159.368	4.61	-1.97	13.0			14.7		16.3	
	6165.360	4.14	-1.47	46.0	70.7	82.9	48.1	45.9	43.9	44.7
	6170.504	4.79	-0.44	80.7			84.1	70.7	81.6	76.9
	6173.336	2.22	-2.88	66.8	104.1	138.2	65.7	70.0	66.0	54.4
	6187.987	3.94	-1.72	42.9	81.7	86.9	34.1	36.6	37.9	33.1
	6213.429	2.22	-2.48	79.5		176.5	81.7	81.8	74.6	71.7
	6219.280	2.20	-2.43	88.7	134.8		89.3	85.0	83.3	85.0
	6226.730	3.88	-2.22	29.2	57.5	68.6	26.1	22.7	22.9	32.4
	6232.641	3.65	-1.22	85.7	132.4	129.1	81.0	72.8	82.9	74.6
	6240.645	2.22	-3.23	54.2	115.5	127.3	49.9	39.9	42.9	35.4
	6246.317	3.60	-0.73	124.5	155.7	181.3	113.8		106.8	
	6252.554	2.40	-1.69	115.2	168.7	194.1	117.7	103.4	110.6	107.3
	6256.360	2.45	-2.41	99.2	179.4	204.5	98.9	91.9	90.6	78.5
	6265.130	2.17	-2.55	88.0	140.7	155.5	93.7	83.3	79.5	76.6
	6271.280	3.33	-2.72	26.8	67.9	77.1		27.8	17.7	21.2
	6290.974	4.73	-0.78	70.7	122.0	126.9	79.7	74.0	74.9	74.6
	6293.924	4.83	-1.72	18.6	50.8		13.3			23.4
	6322.685	2.59	-2.43	79.3	134.8	138.3	70.4	79.8	87.4	94.6
	6335.328	2.20	-2.18	103.6			95.9	87.6	93.9	83.8
	6336.820	3.68	-0.91	107.6	138.6	148.3	95.3	94.6	99.1	86.4
	6344.148	2.43	-2.92	68.3	136.1	155.8	65.9	63.2	59.0	56.0
	6380.743	4.19	-1.38	50.3	85.9	95.2	46.5	44.4	48.8	48.1
	6392.538	2.28	-4.03	18.1	58.7	79.9		13.2		14.8
	6393.612	2.43	-1.57	126.4	195.0	218.2	117.9	122.4	125.9	102.1
	6408.018	3.69	-1.02	108.1	164.0	177.3	97.1		93.9	94.3
	6411.647	3.65	-0.59	135.1	170.7	177.9	115.4	116.6	112.7	105.5
	6469.193	4.83	-0.77	67.3	113.8	83.0	57.7	71.1	60.9	60.9

Equivalent Widths Part II: RGs and TOs 3 – Continued

				Equivalent Widths						
Ion	WL	EP	log(gf)	Solar	RG22	RG41	TO35	TO37	TO0	TO49
	6498.945	0.96	-4.70	30.7	80.2	138.1		23.7		15.7
	6533.940	4.56	-1.38	53.2	81.6	80.0	39.2	34.2	39.0	42.4
	6584.575	5.39	-1.34	10.1						11.2
	6591.313	4.59	-2.07	25.3						
	6592.913	2.73	-1.47	138.1	205.5	235.3	119.6	117.8	121.2	
	6593.870	2.43	-2.42	91.3	140.2	157.6	85.9	85.1	87.5	
	6597.557	4.79	-1.07	44.6	79.0	80.6	58.0	45.1	46.6	29.5
	6608.024	2.28	-4.03	18.5	64.0	81.1	13.7		13.7	
	6627.540	4.55	-1.68	31.2	61.4	73.8		40.2	29.2	18.8
	6646.932	2.61	-3.99	12.8	40.5	53.9		10.5	9.4	6.8
	6653.850	4.15	-2.52	22.8			15.2	18.0		12.2
	6667.417	2.45	-4.40	15.0						8.2
	6667.711	4.58	-2.11	19.0						16.3
	6703.567	2.76	-3.16	38.4	81.2	94.1	24.4	38.5	26.9	30.3
	6705.101	4.61	-1.39	51.7	77.1	88.0	44.0	54.3	54.2	29.5
	6710.316	1.49	-4.88	16.7	70.3	90.1		11.5		6.8
	6713.745	4.79	-1.52	17.8		39.3	22.8		23.6	
	6715.383	4.61	-1.64	29.0		75.6	27.5	32.9	36.1	15.5
	6716.222	4.58	-1.92	18.6			18.3		26.9	7.9
	6725.353	4.10	-2.30	18.9	62.3	58.4		24.3	18.0	13.0
	6726.666	4.61	-1.13	50.3	82.7	97.1	47.3	56.2	45.7	45.3
	6733.151	4.64	-1.58	29.3	51.5		33.1	25.7	31.3	17.2
	6739.520	1.56	-4.79	13.7	54.0	84.2			10.2	
	6745.090	4.58	-2.16	18.1				19.2	19.4	
	6745.957	4.08	-2.77	20.1						
	6746.953	2.61	-4.35	14.1		50.7	12.6			9.2
	6750.150	2.42	-2.62	74.3	114.5	138.5	67.7	73.6	68.2	54.4
	6752.716	4.64	-1.30	38.9		91.0	31.0	33.5	38.9	33.2
	6753.464	4.56	-2.29	13.9						9.6
	6777.408	4.19	-2.82	19.6	53.3	61.0	16.7			15.5
	6783.704	2.59	-3.98	33.0	103.2				17.2	22.8
	6786.856	4.19	-2.07	31.4	79.9	76.8	26.3	39.8	40.8	20.9
	6793.259	4.08	-2.33	16.1						7.9
	7802.473	5.09	-1.52	16.3						9.1
	7807.909	4.99	-0.54	68.4	89.2	99.8	55.2	50.6	61.4	
	7820.803	4.29	-2.64	9.7						
	7844.555	4.83	-1.81	12.8			16.0			
	7879.748	5.03	-1.65	28.3	55.0			20.1	17.1	16.1
Fe II:										
	6084.110	3.20	-3.80	21.3	50.1	51.1	38.7	33.7	36.8	34.1
	6149.249	3.89	-2.88	40.4	48.4	44.6	60.2	61.3	58.8	64.7
	6238.392	3.89	-2.75	44.3	59.7	66.3	69.6	69.4	67.0	71.2
	6247.557	3.89	-2.44	56.8	49.9	57.1	91.1	73.3	83.2	89.4
	6369.462	2.89	-4.23	16.9	31.6	50.4	36.6	40.6	33.0	
	6416.919	3.89	-2.88	38.2	48.3	56.8	53.1	61.3	58.5	60.1
	6456.380	3.90	-2.07	70.9		89.5	117.2	100.4	112.3	110.7
Ni I:										
	6086.280	4.26	-0.51	46.2	68.6	72.2	44.2		41.0	37.2
	6175.370	4.09	-0.53	56.8	80.1	82.3	59.2	53.8	63.5	56.2
	6204.605	4.09	-1.10	25.4	45.8	50.1	24.8	20.9	19.1	17.5
	6327.600	1.68	-3.23	39.6	85.3	102.3	34.1	38.5	32.3	22.9
	6378.260	4.15	-1.00	33.6	57.6	56.8	31.2	32.1	28.6	

Equivalent Widths Part II: RGs and TOs 3 – Continued

				Equivalent Widths						
Ion	WL	EP	log(gf)	Solar	RG22	RG41	TO35	TO37	TO0	TO49
	6643.640	1.68	-2.01	98.3	142.2	159.8	85.3	80.2	86.2	69.3
	6772.320	3.66	-0.98	49.7	80.1	86.0	48.4	42.9	45.7	40.0
Cr I:										
	4616.120	0.98	-1.19	100.6	148.8	159.5	92.0	92.3	91.9	85.8
	4651.290	0.98	-1.46	85.2	130.2	146.6	73.9	73.4	76.2	72.8
	6330.100	0.94	-2.99	30.2	73.5	85.5	15.6	17.7	13.8	
Ba II:										
	5853.690	0.60	-1.00	62.3	95.7	103.9	80.9	78.3	78.5	75.6
	6141.730	0.70	-0.07	122.6	156.1	165.6	137.6	134.1	136.8	144.9
Y II:										
	5087.420	1.08	-0.17	49.4	66.6	69.2	68.1	61.5		59.7
Na I:										
	6154.230	2.10	-1.53	41.0	78.0	84.0	30.1	30.8	31.4	30.1
	6160.750	2.10	-1.23	63.0	104.8	109.4	53.5	51.6	50.4	45.4
Ti I:										
	5978.541	1.87	-0.50	27.5	75.4	90.7		29.0		29.2
	6064.626	1.05	-1.94	15.5	57.6	64.5				
	6126.216	1.07	-1.43	24.1	72.7	81.9		21.8		13.1
	6258.102	1.44	-0.35	56.0	116.5	133.7	45.2	41.3	38.9	35.5
	6261.098	1.43	-0.48	58.5	112.0	131.3	43.4	40.1	41.4	40.1
Ti II:										
	4589.958	1.24	-1.78	75.1	109.3	103.0	93.3	98.9	93.0	98.3
	4708.665	1.24	-2.63	45.6	71.7	96.5	61.5	61.7	56.1	
Ca I:										
	6122.226	1.89	-0.32	202.8	261.7	269.7	161.2	162.4	157.3	150.7
	6166.439	2.52	-1.14	66.8	102.5	112.7	62.5	62.2	63.1	52.1
	6464.680	2.52	-2.53	12.0						
	6572.800	0.00	-4.28	39.0	103.4	127.0				
Si I:										
	6142.480	5.62	-1.54	42.6	46.3	48.0	42.4	40.9	40.1	40.5
	6145.010	5.62	-1.36	42.8	50.8	54.2	48.1		43.2	38.6
	6155.130	5.62	-0.78	92.4	95.3	95.9	89.9	84.6	87.3	86.7
C I:										
	6587.620	8.53	-1.00	17.7	15.6			32.9	35.2	44.2
O I:										
	7771.940	9.15	0.37	74.5	38.8	44.3	127.5	135.1	120.7	133.8
	7774.170	9.15	0.22	63.5	41.5	37.0	115.2	121.1	108.5	126.7
	7775.390	9.15	0.00	51.7	32.0		97.7	94.5	92.1	111.2
Al I:										
	6698.670	3.14	-1.95	30.2		78.5	23.0		25.9	24.2
	7835.310	4.02	-0.47	59.7	95.4	95.9	46.3	46.3	45.3	52.3
	7836.130	4.02	-0.31	69.6	106.7	102.2	59.4			55.3

Table 4: Equivalent Widths Part III: YSs

				Equivalent Widths					
Ion	WL	EP	log(gf)	Solar	YS13	YS23	YS24	YS42	YS43
Fe I:									
	5752.032	4.55	-1.18	56.6	37.4	49.0	41.4	46.6	75.1
	5775.081	4.22	-1.30	57.9	37.5	57.9	25.9	60.5	83.0
	5778.450	2.59	-3.48	21.0	10.1	19.7	15.0	19.2	47.1
	5905.672	4.65	-0.73	64.3	42.4	56.8	39.5	59.9	81.0
	5916.247	2.45	-2.99	70.4		55.0	40.2	65.5	99.1
	5927.786	4.65	-1.09	45.5	34.8	38.4	31.1		55.9
	5929.667	4.55	-1.41	43.8	24.9	44.8	28.5	48.7	62.6
	5930.173	4.65	-0.23	86.5	69.6	89.9	70.0	90.8	101.8
	5934.653	3.93	-1.17	74.3	55.9	72.5	47.3	76.9	97.7
	5969.559	4.28	-2.73	4.2					
	6055.992	4.73	-0.46	76.0	57.8	71.9	68.3	70.7	87.7
	6065.482	2.61	-1.53	114.4	93.2	124.7	93.6		
	6078.491	4.80	-0.32	81.0	64.0	89.4	62.1	82.7	94.2
	6078.999	4.65	-1.12	44.1	16.6	54.6	30.8	28.8	76.7
	6083.660	3.88	-3.50	3.5					
	6085.259	2.76	-3.10	39.8	24.3	36.3	24.1	29.9	70.8
	6098.245	4.56	-1.88	21.0		21.5		20.4	43.0
	6102.171	4.83	-0.52	82.3	58.2	104.8	70.6	79.4	125.0
	6105.131	4.55	-2.05	10.4		12.3			
	6120.249	0.91	-5.96	7.6					26.1
	6127.907	4.14	-1.40	49.9	34.6	54.8	32.0	48.2	76.0
	6151.617	2.18	-3.30	48.9	28.9	45.5	28.4	42.8	74.3
	6157.728	4.08	-1.26	60.1	45.8	71.8	48.0	70.3	94.1
	6159.368	4.61	-1.97	13.0					
	6165.360	4.14	-1.47	46.0	30.3	45.0	31.3	43.6	70.3
	6170.504	4.79	-0.44	80.7	61.0	83.9	60.3	82.2	119.1
	6173.336	2.22	-2.88	66.8	52.3	65.1	51.6	71.4	104.7
	6187.987	3.94	-1.72	42.9	26.0	45.5	31.3	45.3	70.2
	6213.429	2.22	-2.48	79.5	66.0	83.9	68.2	83.5	136.0
	6219.280	2.20	-2.43	88.7	72.3	93.5	74.3	117.4	
	6226.730	3.88	-2.22	29.2	21.2		24.0	24.9	47.0
	6232.641	3.65	-1.22	85.7	62.4	86.9	62.8	106.9	119.6
	6240.645	2.22	-3.23	54.2	33.8	51.5	37.5	56.9	99.7
	6246.317	3.60	-0.73	124.5	111.8	127.0			
	6252.554	2.40	-1.69	115.2	94.8	122.7	102.3		
	6256.360	2.45	-2.41	99.2	75.5	102.1	85.8	128.0	162.9
	6265.130	2.17	-2.55	88.0	67.5	82.6	68.3	116.0	
	6271.280	3.33	-2.72	26.8	16.9	24.9	19.5	24.6	50.7
	6290.974	4.73	-0.78	70.7	42.9	77.0	64.1	72.2	116.1
	6293.924	4.83	-1.72	18.6		16.2			
	6322.685	2.59	-2.43	79.3	69.2	91.9	71.5	94.4	119.8
	6335.328	2.20	-2.18	103.6	75.9		84.5		
	6336.820	3.68	-0.91	107.6	77.5	107.2	80.4		141.4
	6344.148	2.43	-2.92	68.3	46.1	75.4	49.4	78.2	122.2
	6380.743	4.19	-1.38	50.3	38.4	53.6	34.9	53.2	78.9
	6392.538	2.28	-4.03	18.1		13.3		18.9	49.4
	6393.612	2.43	-1.57	126.4	107.5	133.3			
	6408.018	3.69	-1.02	108.1	74.9	107.4	80.2		142.8
	6411.647	3.65	-0.59	135.1		139.7			
	6469.193	4.83	-0.77	67.3	43.7		53.9	61.5	80.9

Equivalent Widths Part III: YSs 4 – Continued

				Equivalent Widths					
Ion	WL	EP	log(gf)	Solar	YS13	YS23	YS24	YS42	YS43
	6498.945	0.96	-4.70	30.7				30.4	73.5
	6533.940	4.56	-1.38	53.2	35.4	58.0	29.2	49.9	62.6
	6584.575	5.39	-1.34	10.1					
	6591.313	4.59	-2.07	25.3					
	6592.913	2.73	-1.47	138.1	113.8	145.1			
	6593.870	2.43	-2.42	91.3	66.5	82.9	72.9	87.4	
	6597.557	4.79	-1.07	44.6	43.1	49.0	30.6	42.0	62.8
	6608.024	2.28	-4.03	18.5				21.6	52.3
	6627.540	4.55	-1.68	31.2	19.2	30.6	21.7	38.5	50.8
	6646.932	2.61	-3.99	12.8					27.0
	6653.850	4.15	-2.52	22.8					
	6667.417	2.45	-4.40	15.0					
	6667.711	4.58	-2.11	19.0					
	6703.567	2.76	-3.16	38.4	22.9	32.2	20.4	41.8	64.1
	6705.101	4.61	-1.39	51.7	29.4	55.7	30.3	52.1	68.4
	6710.316	1.49	-4.88	16.7		10.6		10.6	45.0
	6713.745	4.79	-1.52	17.8					
	6715.383	4.61	-1.64	29.0		28.7	21.4	32.8	
	6716.222	4.58	-1.92	18.6		21.9		19.9	
	6725.353	4.10	-2.30	18.9		15.4			
	6726.666	4.61	-1.13	50.3	34.8	46.8	27.6	47.9	68.1
	6733.151	4.64	-1.58	29.3	21.6	26.2	18.8		50.9
	6739.520	1.56	-4.79	13.7					51.8
	6745.090	4.58	-2.16	18.1					
	6745.957	4.08	-2.77	20.1					
	6746.953	2.61	-4.35	14.1					
	6750.150	2.42	-2.62	74.3	53.4	71.0	60.2	69.2	112.4
	6752.716	4.64	-1.30	38.9	20.6	49.5	29.5	37.3	69.0
	6753.464	4.56	-2.29	13.9					
	6777.408	4.19	-2.82	19.6					
	6783.704	2.59	-3.98	33.0					
	6786.856	4.19	-2.07	31.4		40.6	27.5		61.7
	6793.259	4.08	-2.33	16.1					
	7802.473	5.09	-1.52	16.3		14.4			
	7807.909	4.99	-0.54	68.4	35.7	67.6	35.9	55.5	76.0
	7820.803	4.29	-2.64	9.7					
	7844.555	4.83	-1.81	12.8					
	7879.748	5.03	-1.65	28.3					
Fe II:									
	6084.110	3.20	-3.80	21.3	20.4	24.9	20.5	39.2	33.1
	6149.249	3.89	-2.88	40.4	37.4	49.1	45.2	67.0	55.4
	6238.392	3.89	-2.75	44.3	44.3	57.9	46.9	76.8	64.1
	6247.557	3.89	-2.44	56.8	51.8	63.5	62.2	93.7	72.4
	6369.462	2.89	-4.23	16.9	21.7	22.4	23.2	40.3	35.4
	6416.919	3.89	-2.88	38.2	37.5	46.4	41.4	62.6	49.1
	6456.380	3.90	-2.07	70.9	74.9	80.9	79.2	119.7	93.9
Ni I:									
	6086.280	4.26	-0.51	46.2	28.9	45.2	36.7	47.6	60.2
	6175.370	4.09	-0.53	56.8	37.8	56.4	55.3	69.2	69.3
	6204.605	4.09	-1.10	25.4	14.4	24.3	12.3	23.3	41.5
	6327.600	1.68	-3.23	39.6	31.1	38.2	28.3	45.5	79.6
	6378.260	4.15	-1.00	33.6	21.3	34.5	24.4	25.8	53.1

Equivalent Widths Part III: YSs 4 – Continued

				Equivalent Widths					
Ion	WL	EP	log(gf)	Solar	YS13	YS23	YS24	YS42	YS43
	6643.640	1.68	-2.01	98.3	75.9	91.2	76.6	96.5	139.8
	6772.320	3.66	-0.98	49.7	34.6	50.6	42.2	45.4	67.6
Cr I:									
	4616.120	0.98	-1.19	100.6	81.0	92.7	85.9	106.0	141.9
	4651.290	0.98	-1.46	85.2	68.4	86.4		87.8	126.2
	6330.100	0.94	-2.99	30.2	14.4	24.5	13.8	18.7	59.7
Ba II:									
	5853.690	0.60	-1.00	62.3	61.8	79.2	67.6	94.9	103.0
	6141.730	0.70	-0.07	122.6	113.9	148.2	120.2	159.9	168.5
Y II:									
	5087.420	1.08	-0.17	49.4	42.6	55.5	52.1	75.3	68.7
Na I:									
	6154.230	2.10	-1.53	41.0		37.2	23.4	34.4	60.9
	6160.750	2.10	-1.23	63.0		55.0	45.7	61.2	92.8
Ti I:									
	5978.541	1.87	-0.50	27.5	22.7	22.8	14.5		61.8
	6064.626	1.05	-1.94	15.5	12.3	14.0	14.9	7.2	37.5
	6126.216	1.07	-1.43	24.1	13.5	30.3		17.1	50.8
	6258.102	1.44	-0.35	56.0	31.4	48.0	33.2	43.9	88.2
	6261.098	1.43	-0.48	58.5	31.3	52.9	33.5	43.4	87.6
Ti II:									
	4589.958	1.24	-1.78	75.1	91.1	88.0	89.9	105.7	107.9
	4708.665	1.24	-2.63	45.6	57.2	46.6	59.9	63.7	74.3
Ca I:									
	6122.226	1.89	-0.32	202.8	153.0	206.8	142.6	167.9	245.5
	6166.439	2.52	-1.14	66.8	49.3	72.7	48.7	62.5	95.8
	6464.680	2.52	-2.53	12.0					
	6572.800	0.00	-4.28	39.0					83.0
Si I:									
	6142.480	5.62	-1.54	42.6	31.5	48.1	30.9	40.6	49.5
	6145.010	5.62	-1.36	42.8	28.7	44.1	28.1	46.4	50.5
	6155.130	5.62	-0.78	92.4	70.8	99.1		93.9	92.6
C I:									
	6587.620	8.53	-1.00	17.7	23.3	21.8	22.5	29.9	8.8
O I:									
	7771.940	9.15	0.37	74.5	85.6	104.4	90.6	138.8	76.4
	7774.170	9.15	0.22	63.5	71.0	87.1	74.1	123.9	65.6
	7775.390	9.15	0.00	51.7	58.0	69.8	60.0	95.3	47.1
Al I:									
	6698.670	3.14	-1.95	30.2	20.3				
	7835.310	4.02	-0.47	59.7	35.5	56.5	35.7	43.3	72.9
	7836.130	4.02	-0.31	69.6	40.7	66.2	46.1	53.3	80.5

Table 5: Equivalent Widths Part IV: YSs

				Equivalent Widths					
Ion	WL	EP	log(gf)	Solar	YS44	YS45	YS46	YS47	YS48
Fe I:									
	5752.032	4.55	-1.18	56.6	70.6	48.6	40.0	59.4	69.1
	5775.081	4.22	-1.30	57.9	77.4	46.3	52.2	63.8	73.5
	5778.450	2.59	-3.48	21.0	55.0	12.8		23.6	34.4
	5905.672	4.65	-0.73	64.3	72.5	51.5	41.6	53.7	74.8
	5916.247	2.45	-2.99	70.4		50.8			
	5927.786	4.65	-1.09	45.5		30.7	37.2	46.6	52.7
	5929.667	4.55	-1.41	43.8	54.1	32.5		46.9	58.3
	5930.173	4.65	-0.23	86.5	108.2	76.4		79.9	105.6
	5934.653	3.93	-1.17	74.3	100.8	61.8	62.4	78.8	104.6
	5969.559	4.28	-2.73	4.2					
	6055.992	4.73	-0.46	76.0	98.5	61.3	90.8	78.2	104.4
	6065.482	2.61	-1.53	114.4			148.6		
	6078.491	4.80	-0.32	81.0	108.7	75.0	105.0	88.2	110.4
	6078.999	4.65	-1.12	44.1	79.8	27.6	37.4	45.9	76.9
	6083.660	3.88	-3.50	3.5					
	6085.259	2.76	-3.10	39.8	82.1	25.5	53.9	54.2	60.6
	6098.245	4.56	-1.88	21.0		10.3		25.8	39.3
	6102.171	4.83	-0.52	82.3	98.8	71.9	105.6	107.1	131.5
	6105.131	4.55	-2.05	10.4					
	6120.249	0.91	-5.96	7.6	35.2				
	6127.907	4.14	-1.40	49.9	82.1	38.5	63.2	55.4	62.5
	6151.617	2.18	-3.30	48.9	87.5	36.7	59.6	56.1	63.2
	6157.728	4.08	-1.26	60.1	102.3	56.5	77.7	75.9	78.8
	6159.368	4.61	-1.97	13.0					
	6165.360	4.14	-1.47	46.0	73.3	35.3	55.3	49.3	58.2
	6170.504	4.79	-0.44	80.7	138.1	71.0		96.5	116.3
	6173.336	2.22	-2.88	66.8	114.0	58.2	63.5	73.0	93.8
	6187.987	3.94	-1.72	42.9	74.5	35.1	51.1	50.3	68.6
	6213.429	2.22	-2.48	79.5		69.1	84.7	87.3	125.2
	6219.280	2.20	-2.43	88.7		79.0			
	6226.730	3.88	-2.22	29.2	55.2	22.2	40.1	35.2	43.6
	6232.641	3.65	-1.22	85.7		66.8	87.9	95.1	121.9
	6240.645	2.22	-3.23	54.2	110.1	45.2	61.2	76.0	88.2
	6246.317	3.60	-0.73	124.5					177.5
	6252.554	2.40	-1.69	115.2					
	6256.360	2.45	-2.41	99.2	175.0	86.0			
	6265.130	2.17	-2.55	88.0		72.7			
	6271.280	3.33	-2.72	26.8	61.4	18.9	41.0	33.1	41.8
	6290.974	4.73	-0.78	70.7	111.2	69.5	80.0	88.6	118.3
	6293.924	4.83	-1.72	18.6					
	6322.685	2.59	-2.43	79.3		68.1	79.3	83.2	108.6
	6335.328	2.20	-2.18	103.6					
	6336.820	3.68	-0.91	107.6					148.3
	6344.148	2.43	-2.92	68.3	137.5	60.9	80.5	98.7	101.9
	6380.743	4.19	-1.38	50.3	87.3	44.0	35.7	63.8	61.8
	6392.538	2.28	-4.03	18.1	67.9	15.0	21.7		34.9
	6393.612	2.43	-1.57	126.4					
	6408.018	3.69	-1.02	108.1	157.3				150.7
	6411.647	3.65	-0.59	135.1					199.4
	6469.193	4.83	-0.77	67.3	99.9	47.1	43.8	58.6	66.4

Equivalent Widths Part IV: YSs 5 – Continued

				Equivalent Widths					
Ion	WL	EP	log(gf)	Solar	YS44	YS45	YS46	YS47	YS48
	6498.945	0.96	-4.70	30.7	90.2		37.5	33.8	69.0
	6533.940	4.56	-1.38	53.2	77.8	36.2	50.1	47.2	
	6584.575	5.39	-1.34	10.1					
	6591.313	4.59	-2.07	25.3					
	6592.913	2.73	-1.47	138.1					
	6593.870	2.43	-2.42	91.3		79.1			
	6597.557	4.79	-1.07	44.6	69.0	34.1	44.4	50.7	58.9
	6608.024	2.28	-4.03	18.5	51.9	11.9		27.0	39.8
	6627.540	4.55	-1.68	31.2	57.0	26.2	34.8	40.9	42.0
	6646.932	2.61	-3.99	12.8	30.1			19.0	24.6
	6653.850	4.15	-2.52	22.8					
	6667.417	2.45	-4.40	15.0					
	6667.711	4.58	-2.11	19.0					
	6703.567	2.76	-3.16	38.4	81.1	28.0	27.6	45.2	54.5
	6705.101	4.61	-1.39	51.7	77.5	34.3	46.7	50.6	66.0
	6710.316	1.49	-4.88	16.7	70.4		19.2	23.9	36.1
	6713.745	4.79	-1.52	17.8					
	6715.383	4.61	-1.64	29.0		22.2	26.4	38.0	45.6
	6716.222	4.58	-1.92	18.6		19.2		30.6	35.1
	6725.353	4.10	-2.30	18.9		18.6			29.1
	6726.666	4.61	-1.13	50.3	81.0	38.3	42.9	46.6	67.3
	6733.151	4.64	-1.58	29.3	62.6	21.9	23.1	36.4	41.6
	6739.520	1.56	-4.79	13.7	68.1			23.0	
	6745.090	4.58	-2.16	18.1					
	6745.957	4.08	-2.77	20.1					
	6746.953	2.61	-4.35	14.1					
	6750.150	2.42	-2.62	74.3		63.4		78.7	98.6
	6752.716	4.64	-1.30	38.9		28.6	32.8	41.9	61.8
	6753.464	4.56	-2.29	13.9					
	6777.408	4.19	-2.82	19.6					
	6783.704	2.59	-3.98	33.0					
	6786.856	4.19	-2.07	31.4	72.2	24.7	47.5	42.2	50.6
	6793.259	4.08	-2.33	16.1					
	7802.473	5.09	-1.52	16.3		16.3			
	7807.909	4.99	-0.54	68.4	86.1	50.4	75.8	72.0	76.9
	7820.803	4.29	-2.64	9.7					
	7844.555	4.83	-1.81	12.8					
	7879.748	5.03	-1.65	28.3					
Fe II:									
	6084.110	3.20	-3.80	21.3	44.8	25.1	20.4	24.0	18.0
	6149.249	3.89	-2.88	40.4	60.4	44.5	44.6	43.9	34.6
	6238.392	3.89	-2.75	44.3	66.7	49.5	55.1	58.1	41.4
	6247.557	3.89	-2.44	56.8	73.3	60.1	52.4	63.7	50.5
	6369.462	2.89	-4.23	16.9	42.5	22.4	18.8	26.0	16.9
	6416.919	3.89	-2.88	38.2	54.1	42.0	20.4	46.4	33.7
	6456.380	3.90	-2.07	70.9	98.2	84.3		84.0	
Ni I:									
	6086.280	4.26	-0.51	46.2	66.6	35.4	57.3	48.9	52.2
	6175.370	4.09	-0.53	56.8	74.4	48.7	69.6	58.7	58.4
	6204.605	4.09	-1.10	25.4	48.7	19.8	30.9	24.1	29.5
	6327.600	1.68	-3.23	39.6	93.2	27.9	36.4	44.0	52.1
	6378.260	4.15	-1.00	33.6	64.3	26.1	22.3	38.3	36.5

Equivalent Widths Part IV: YSs 5 – Continued

Ion	WL	EP	log(gf)	Equivalent Widths					
				Solar	YS44	YS45	YS46	YS47	YS48
	6643.640	1.68	-2.01	98.3	149.7	83.2	67.9	101.9	115.6
	6772.320	3.66	-0.98	49.7	78.5	45.0		58.4	63.8
Cr I:									
	4616.120	0.98	-1.19	100.6	152.4	84.2		118.0	142.6
	4651.290	0.98	-1.46	85.2	137.3	71.2	60.8	96.9	111.4
	6330.100	0.94	-2.99	30.2	66.8	15.6	22.5	35.5	50.4
Ba II:									
	5853.690	0.60	-1.00	62.3	107.6	64.0	35.6	70.9	80.1
	6141.730	0.70	-0.07	122.6	177.2	119.8	136.6	128.7	160.4
Y II:									
	5087.420	1.08	-0.17	49.4	76.7	47.8	55.5	49.2	60.2
Na I:									
	6154.230	2.10	-1.53	41.0	77.8	27.6	58.1	51.6	52.2
	6160.750	2.10	-1.23	63.0	105.8	45.1	85.1	77.3	81.8
Ti I:									
	5978.541	1.87	-0.50	27.5	71.6	24.7	30.9	40.1	54.8
	6064.626	1.05	-1.94	15.5	42.8	9.6	21.8	22.0	29.5
	6126.216	1.07	-1.43	24.1	65.5	16.2	35.5	31.0	45.9
	6258.102	1.44	-0.35	56.0	106.3	44.1	69.2	64.1	76.9
	6261.098	1.43	-0.48	58.5	107.0	38.6	78.5	67.0	77.8
Ti II:									
	4589.958	1.24	-1.78	75.1	105.9	85.1	49.0	85.1	81.4
	4708.665	1.24	-2.63	45.6	74.4	46.9	48.8	52.5	51.9
Ca I:									
	6122.226	1.89	-0.32	202.8	242.2	159.7	261.7	221.2	325.1
	6166.439	2.52	-1.14	66.8	98.0	55.7	87.1	81.5	97.7
	6464.680	2.52	-2.53	12.0					
	6572.800	0.00	-4.28	39.0	100.6		53.0		76.6
Si I:									
	6142.480	5.62	-1.54	42.6	52.7	32.7	47.5	42.4	38.8
	6145.010	5.62	-1.36	42.8	52.7	34.1	46.1	43.3	
	6155.130	5.62	-0.78	92.4	98.4	76.3	99.8	91.3	92.9
C I:									
	6587.620	8.53	-1.00	17.7	16.5	18.6		18.8	9.3
O I:									
	7771.940	9.15	0.37	74.5	61.5	83.9	60.5	77.3	48.5
	7774.170	9.15	0.22	63.5	54.1	73.2	52.1	67.6	38.5
	7775.390	9.15	0.00	51.7	42.6	60.5	38.6	53.9	26.4
Al I:									
	6698.670	3.14	-1.95	30.2				43.5	
	7835.310	4.02	-0.47	59.7	84.2	36.6	74.9	60.4	69.7
	7836.130	4.02	-0.31	69.6	98.3	51.1	91.5	84.3	81.8

Table 6. Abundance Values Part I: SGs

Ion	SG16	SG17	SG20	SG21	SG25	SG26	SG33	SG36
[FeI/H]	$0.13^{+0.10}_{-0.10}$	$0.12^{+0.09}_{-0.09}$	$0.12^{+0.08}_{-0.07}$	$0.14^{+0.11}_{-0.11}$	$0.22^{+0.09}_{-0.08}$	$0.07^{+0.08}_{-0.09}$	$0.17^{+0.11}_{-0.13}$	$0.18^{+0.09}_{-0.10}$
[FeII/H]	$0.13^{+0.19}_{-0.36}$	$0.12^{+0.12}_{-0.37}$	$0.12^{+0.18}_{-0.45}$	$0.14^{+0.18}_{-0.57}$	$0.22^{+0.14}_{-0.29}$	$0.07^{+0.10}_{-0.28}$	$0.17^{+0.14}_{-0.43}$	$0.18^{+0.11}_{-0.35}$
[NiI/H]	$0.04^{+0.11}_{-0.12}$	$0.17^{+0.08}_{-0.08}$	$0.10^{+0.09}_{-0.12}$	$0.12^{+0.10}_{-0.16}$	$0.15^{+0.08}_{-0.10}$	$-0.01^{+0.08}_{-0.08}$	$-0.19^{+0.13}_{-0.13}$	$0.06^{+0.08}_{-0.08}$
[CrI/H]	$-0.04^{+0.18}_{-0.18}$	$0.15^{+0.12}_{-0.16}$	$-0.01^{+0.14}_{-0.16}$	$-0.07^{+0.18}_{-0.21}$	$0.01^{+0.14}_{-0.15}$	$0.06^{+0.20}_{-0.20}$	$-0.05^{+0.15}_{-0.17}$	$0.02^{+0.11}_{-0.12}$
[BaII/H]	$-0.05^{+0.17}_{-0.23}$	$0.12^{+0.11}_{-0.23}$	$0.04^{+0.15}_{-0.26}$	$-0.12^{+0.18}_{-0.33}$	$0.06^{+0.13}_{-0.19}$	$0.04^{+0.12}_{-0.21}$	$0.11^{+0.16}_{-0.32}$	$0.10^{+0.13}_{-0.27}$
[YII/H]	$-0.19^{+1.30}_{-0.96}$	$0.08^{+0.48}_{-0.33}$	$0.01^{+1.20}_{-0.93}$	$-0.21^{+1.27}_{-1.21}$	$0.01^{+1.03}_{-0.78}$	$-0.06^{+0.27}_{-0.36}$	$-0.18^{+0.34}_{-0.51}$	$0.15^{+0.26}_{-0.42}$
[NaI/H]	$0.09^{+0.09}_{-0.10}$	$0.12^{+0.06}_{-0.07}$	$0.00^{+0.07}_{-0.09}$	$0.14^{+0.09}_{-0.12}$	$0.19^{+0.11}_{-0.12}$	$-0.06^{+0.06}_{-0.06}$	$-0.09^{+0.30}_{-0.30}$	$0.02^{+0.06}_{-0.06}$
[TiI/H]	$0.07^{+0.15}_{-0.16}$	$0.15^{+0.10}_{-0.11}$	$0.12^{+0.11}_{-0.13}$	$0.20^{+0.15}_{-0.17}$	$0.12^{+0.12}_{-0.13}$	$-0.11^{+0.16}_{-0.16}$	$-0.12^{+0.13}_{-0.13}$	$0.06^{+0.10}_{-0.10}$
[TiII/H]	$0.05^{+0.20}_{-0.29}$	$0.14^{+0.24}_{-0.36}$	$0.02^{+0.20}_{-0.37}$	$0.09^{+0.25}_{-0.49}$	$0.14^{+0.16}_{-0.26}$	$0.26^{+0.15}_{-0.26}$	$-0.04^{+0.34}_{-0.48}$	$0.30^{+0.34}_{-0.45}$
[CaI/H]	$0.12^{+0.16}_{-0.20}$	$0.18^{+0.10}_{-0.17}$	$0.11^{+0.14}_{-0.20}$	$0.02^{+0.16}_{-0.26}$	$0.24^{+0.13}_{-0.17}$	$0.06^{+0.12}_{-0.16}$	$0.10^{+0.20}_{-0.27}$	$0.11^{+0.11}_{-0.19}$
[SiI/H]	$0.07^{+0.06}_{-0.08}$	$0.08^{+0.03}_{-0.02}$	$0.03^{+0.05}_{-0.09}$	$-0.03^{+0.06}_{-0.12}$	$0.11^{+0.05}_{-0.07}$	$-0.02^{+0.05}_{-0.05}$	$-0.13^{+0.12}_{-0.13}$	$0.06^{+0.05}_{-0.06}$
[CI/H]	$0.16^{+0.32}_{-0.38}$	$0.00^{+0.23}_{-0.34}$	$0.05^{+0.30}_{-0.41}$	$0.16^{+0.34}_{-0.50}$		$0.08^{+0.25}_{-0.31}$		$0.05^{+0.25}_{-0.35}$
[OI/H]	$-0.11^{+0.20}_{-0.30}$	$0.02^{+0.13}_{-0.30}$	$0.08^{+0.18}_{-0.35}$	$-0.05^{+0.19}_{-0.44}$	$0.04^{+0.15}_{-0.26}$	$0.29^{+0.11}_{-0.17}$		$0.16^{+0.12}_{-0.21}$
[AlI/H]	$0.17^{+0.09}_{-0.10}$	$0.10^{+0.07}_{-0.08}$	$0.10^{+0.08}_{-0.11}$	$0.14^{+0.08}_{-0.14}$	$0.33^{+0.07}_{-0.08}$	$-0.02^{+0.08}_{-0.09}$		$-0.03^{+0.06}_{-0.10}$

Table 7. Abundance Values Part II: RGs and TOs

Ion	RG22	RG41	TO35	TO37	TO0	TO49
[FeI/H]	$0.15^{+0.10}_{-0.09}$	$-0.13^{+0.10}_{-0.12}$	$0.18^{+0.08}_{-0.09}$	$0.11^{+0.08}_{-0.10}$	$0.13^{+0.08}_{-0.09}$	$0.03^{+0.09}_{-0.09}$
[FeII/H]	$0.15^{+0.20}_{-0.59}$	$-0.13^{+0.22}_{-0.64}$	$0.18^{+0.11}_{-0.26}$	$0.11^{+0.09}_{-0.28}$	$0.13^{+0.09}_{-0.26}$	$0.03^{+0.12}_{-0.25}$
[NiI/H]	$0.05^{+0.12}_{-0.19}$	$-0.27^{+0.14}_{-0.20}$	$0.15^{+0.08}_{-0.08}$	$0.05^{+0.10}_{-0.10}$	$0.08^{+0.08}_{-0.09}$	$-0.06^{+0.11}_{-0.11}$
[CrI/H]	$-0.05^{+0.18}_{-0.19}$	$-0.45^{+0.16}_{-0.17}$	$0.06^{+0.11}_{-0.12}$	$0.02^{+0.12}_{-0.13}$	$0.02^{+0.12}_{-0.13}$	$-0.07^{+0.12}_{-0.13}$
[BaII/H]	$-0.07^{+0.24}_{-0.46}$	$-0.71^{+0.27}_{-0.49}$	$0.12^{+0.13}_{-0.20}$	$0.06^{+0.11}_{-0.22}$	$0.10^{+0.09}_{-0.20}$	$-0.04^{+0.18}_{-0.24}$
[YII/H]	$-0.19^{+0.78}_{-1.54}$		$0.19^{+0.25}_{-0.33}$	$0.03^{+0.25}_{-0.36}$		$-0.14^{+0.29}_{-0.37}$
[NaI/H]	$0.18^{+0.09}_{-0.10}$	$0.01^{+0.08}_{-0.09}$	$0.06^{+0.07}_{-0.07}$	$0.02^{+0.06}_{-0.06}$	$0.03^{+0.05}_{-0.06}$	$-0.02^{+0.08}_{-0.08}$
[TiI/H]	$0.11^{+0.15}_{-0.16}$	$-0.22^{+0.14}_{-0.15}$	$0.13^{+0.11}_{-0.11}$	$0.21^{+0.13}_{-0.14}$	$-0.01^{+0.09}_{-0.09}$	$0.10^{+0.14}_{-0.15}$
[TiII/H]	$0.10^{+0.25}_{-0.48}$	$-0.42^{+0.48}_{-0.64}$	$0.14^{+0.16}_{-0.24}$	$0.18^{+0.15}_{-0.28}$	$0.20^{+0.16}_{-0.28}$	$0.06^{+0.29}_{-0.35}$
[CaI/H]	$0.09^{+0.16}_{-0.19}$	$-0.13^{+0.16}_{-0.19}$	$0.15^{+0.14}_{-0.16}$	$0.12^{+0.12}_{-0.17}$	$0.13^{+0.11}_{-0.16}$	$-0.01^{+0.13}_{-0.16}$
[SiI/H]	$0.03^{+0.10}_{-0.21}$	$-0.11^{+0.12}_{-0.22}$	$0.13^{+0.06}_{-0.06}$	$0.04^{+0.05}_{-0.06}$	$0.07^{+0.05}_{-0.05}$	$0.04^{+0.06}_{-0.06}$
[CI/H]	$0.14^{+0.36}_{-0.51}$			$0.02^{+0.24}_{-0.31}$	$0.04^{+0.21}_{-0.28}$	$0.14^{+0.28}_{-0.33}$
[OI/H]	$-0.12^{+0.29}_{-0.52}$	$-0.09^{+0.31}_{-0.55}$	$0.17^{+0.12}_{-0.16}$	$0.29^{+0.12}_{-0.19}$	$0.15^{+0.10}_{-0.17}$	$0.27^{+0.13}_{-0.17}$
[AlI/H]	$0.27^{+0.07}_{-0.07}$	$0.15^{+0.07}_{-0.07}$	$0.04^{+0.06}_{-0.08}$	$-0.02^{+0.05}_{-0.08}$	$0.05^{+0.09}_{-0.11}$	$0.06^{+0.06}_{-0.08}$

Table 8. Abundance Values Part III: YSs

Ion	YS13	YS23	YS24	YS42	YS43
[FeI/H]	$-0.28\ ^{+0.07}_{-0.09}$	$0.12\ ^{+0.06}_{-0.08}$	$-0.22\ ^{+0.08}_{-0.09}$	$-0.14\ ^{+0.07}_{-0.08}$	$-0.08\ ^{+0.08}_{-0.08}$
[FeII/H]	$-0.28\ ^{+0.09}_{-0.37}$	$0.12\ ^{+0.08}_{-0.28}$	$-0.22\ ^{+0.10}_{-0.37}$	$-0.14\ ^{+0.10}_{-0.38}$	$-0.08\ ^{+0.12}_{-0.42}$
[NiI/H]	$-0.27\ ^{+0.08}_{-0.08}$	$0.10\ ^{+0.07}_{-0.07}$	$-0.17\ ^{+0.10}_{-0.09}$	$-0.20\ ^{+0.10}_{-0.09}$	$-0.16\ ^{+0.08}_{-0.08}$
[CrI/H]	$-0.30\ ^{+0.10}_{-0.12}$	$0.07\ ^{+0.12}_{-0.13}$	$-0.24\ ^{+0.12}_{-0.14}$	$-0.34\ ^{+0.10}_{-0.12}$	$-0.20\ ^{+0.10}_{-0.11}$
[BaII/H]	$-0.35\ ^{+0.15}_{-0.33}$	$0.29\ ^{+0.13}_{-0.24}$	$-0.24\ ^{+0.15}_{-0.33}$	$-0.41\ ^{+0.15}_{-0.32}$	$-0.25\ ^{+0.15}_{-0.31}$
[YII/H]	$-0.41\ ^{+0.22}_{-0.41}$	$0.17\ ^{+0.21}_{-0.32}$	$-0.23\ ^{+0.23}_{-0.42}$	$-0.33\ ^{+0.24}_{-0.41}$	$-0.40\ ^{+0.25}_{-0.41}$
[NaI/H]	$-0.34\ ^{+0.07}_{-0.08}$	$0.04\ ^{+0.06}_{-0.07}$	$-0.19\ ^{+0.08}_{-0.09}$	$-0.08\ ^{+0.12}_{-0.13}$	$0.02\ ^{+0.07}_{-0.08}$
[TiI/H]	$-0.16\ ^{+0.13}_{-0.13}$	$0.20\ ^{+0.10}_{-0.11}$	$-0.16\ ^{+0.16}_{-0.17}$	$-0.31\ ^{+0.10}_{-0.10}$	$-0.15\ ^{+0.10}_{-0.10}$
[TiII/H]	$0.03\ ^{+0.14}_{-0.38}$	$0.17\ ^{+0.15}_{-0.28}$	$0.02\ ^{+0.14}_{-0.37}$	$-0.36\ ^{+0.15}_{-0.36}$	$-0.19\ ^{+0.15}_{-0.35}$
[CaI/H]	$-0.22\ ^{+0.09}_{-0.12}$	$0.17\ ^{+0.09}_{-0.10}$	$-0.24\ ^{+0.11}_{-0.14}$	$-0.22\ ^{+0.11}_{-0.14}$	$-0.04\ ^{+0.10}_{-0.12}$
[SiI/H]	$-0.22\ ^{+0.04}_{-0.04}$	$0.10\ ^{+0.04}_{-0.04}$	$-0.22\ ^{+0.06}_{-0.06}$	$-0.06\ ^{+0.04}_{-0.05}$	$-0.08\ ^{+0.04}_{-0.04}$
[CI/H]	$-0.01\ ^{+0.21}_{-0.36}$	$-0.01\ ^{+0.20}_{-0.29}$	$-0.08\ ^{+0.23}_{-0.37}$	$-0.02\ ^{+0.23}_{-0.37}$	$-0.33\ ^{+0.25}_{-0.37}$
[OI/H]	$-0.12\ ^{+0.13}_{-0.31}$	$0.10\ ^{+0.11}_{-0.23}$	$-0.12\ ^{+0.14}_{-0.32}$	$0.33\ ^{+0.15}_{-0.31}$	$0.16\ ^{+0.14}_{-0.30}$
[AlI/H]	$-0.22\ ^{+0.07}_{-0.08}$	$0.03\ ^{+0.04}_{-0.05}$	$-0.22\ ^{+0.06}_{-0.08}$	$-0.16\ ^{+0.04}_{-0.06}$	$0.00\ ^{+0.04}_{-0.06}$

Table 9. Abundance Values Part IV: YSs

Ion	YS44	YS45	YS46	YS47	YS48
[FeI/H]	$-0.22\ ^{+0.09}_{-0.09}$	$-0.11\ ^{+0.06}_{-0.07}$	$-0.27\ ^{+0.11}_{-0.12}$	$-0.05\ ^{+0.08}_{-0.09}$	$-0.02\ ^{+0.08}_{-0.07}$
[FeII/H]	$-0.22\ ^{+0.15}_{-0.41}$	$-0.11\ ^{+0.08}_{-0.22}$	$-0.27\ ^{+0.18}_{-0.55}$	$-0.05\ ^{+0.11}_{-0.38}$	$-0.02\ ^{+0.10}_{-0.44}$
[NiI/H]	$-0.29\ ^{+0.10}_{-0.10}$	$-0.12\ ^{+0.06}_{-0.06}$	$-0.35\ ^{+0.21}_{-0.21}$	$-0.14\ ^{+0.09}_{-0.08}$	$-0.17\ ^{+0.09}_{-0.08}$
[CrI/H]	$-0.45\ ^{+0.11}_{-0.12}$	$-0.20\ ^{+0.09}_{-0.10}$	$-0.71\ ^{+0.47}_{-0.48}$	$-0.08\ ^{+0.12}_{-0.14}$	$-0.19\ ^{+0.13}_{-0.15}$
[BaII/H]	$-0.64\ ^{+0.21}_{-0.29}$	$-0.15\ ^{+0.11}_{-0.19}$	$-0.85\ ^{+0.37}_{-0.53}$	$-0.28\ ^{+0.15}_{-0.32}$	$-0.09\ ^{+0.15}_{-0.34}$
[YII/H]	$-0.66\ ^{+0.30}_{-0.39}$	$-0.23\ ^{+0.18}_{-0.26}$	$-0.36\ ^{+0.35}_{-0.56}$	$-0.35\ ^{+0.26}_{-0.42}$	$-0.05\ ^{+0.22}_{-0.41}$
[NaI/H]	$0.04\ ^{+0.05}_{-0.06}$	$-0.16\ ^{+0.04}_{-0.05}$	$0.08\ ^{+0.09}_{-0.10}$	$0.09\ ^{+0.06}_{-0.07}$	$-0.06\ ^{+0.05}_{-0.07}$
[TiI/H]	$-0.28\ ^{+0.10}_{-0.11}$	$-0.07\ ^{+0.09}_{-0.10}$	$-0.10\ ^{+0.15}_{-0.16}$	$-0.03\ ^{+0.10}_{-0.11}$	$-0.10\ ^{+0.11}_{-0.12}$
[TiII/H]	$-0.60\ ^{+0.24}_{-0.35}$	$-0.06\ ^{+0.16}_{-0.25}$	$-0.63\ ^{+0.54}_{-0.70}$	$-0.17\ ^{+0.14}_{-0.36}$	$-0.12\ ^{+0.18}_{-0.39}$
[CaI/H]	$-0.22\ ^{+0.12}_{-0.13}$	$-0.09\ ^{+0.08}_{-0.09}$	$-0.05\ ^{+0.19}_{-0.22}$	$0.07\ ^{+0.11}_{-0.13}$	$0.04\ ^{+0.11}_{-0.14}$
[SiI/H]	$-0.13\ ^{+0.04}_{-0.04}$	$-0.14\ ^{+0.03}_{-0.03}$	$-0.06\ ^{+0.07}_{-0.07}$	$-0.06\ ^{+0.04}_{-0.04}$	$-0.10\ ^{+0.04}_{-0.04}$
[CI/H]	$0.04\ ^{+0.28}_{-0.35}$	$-0.16\ ^{+0.18}_{-0.24}$		$0.03\ ^{+0.25}_{-0.38}$	$-0.07\ ^{+0.22}_{-0.37}$
[OI/H]	$0.03\ ^{+0.18}_{-0.27}$	$-0.09\ ^{+0.11}_{-0.19}$	$-0.21\ ^{+0.24}_{-0.43}$	$0.06\ ^{+0.14}_{-0.30}$	$-0.16\ ^{+0.13}_{-0.31}$
[AlI/H]	$0.10\ ^{+0.06}_{-0.07}$	$-0.18\ ^{+0.08}_{-0.08}$	$0.08\ ^{+0.08}_{-0.10}$	$0.09\ ^{+0.08}_{-0.09}$	$-0.07\ ^{+0.04}_{-0.07}$

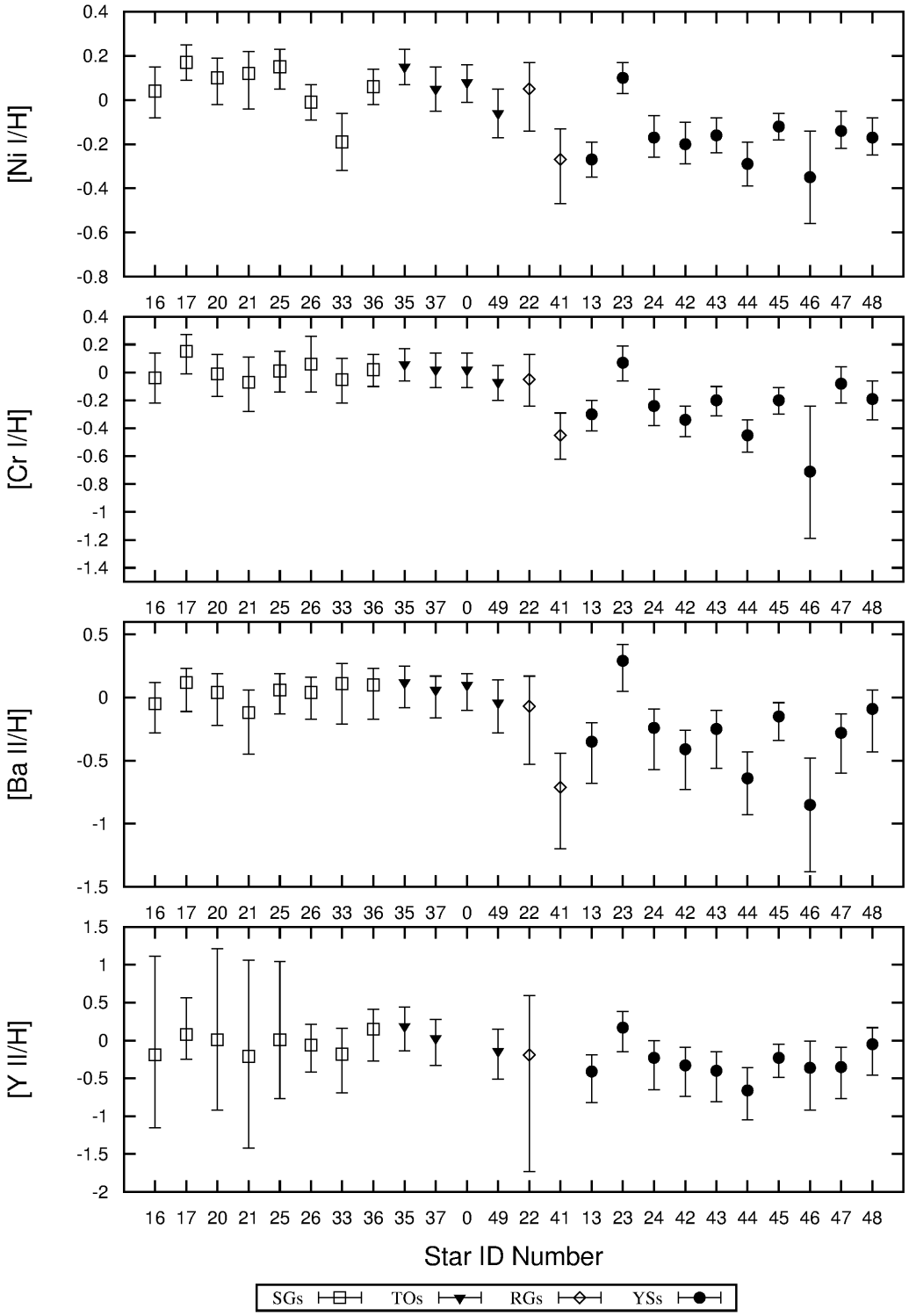

Figure 18: Abundance plots for [Ni I/H], [Cr I/H], [Ba II/H] and [Y II/H].

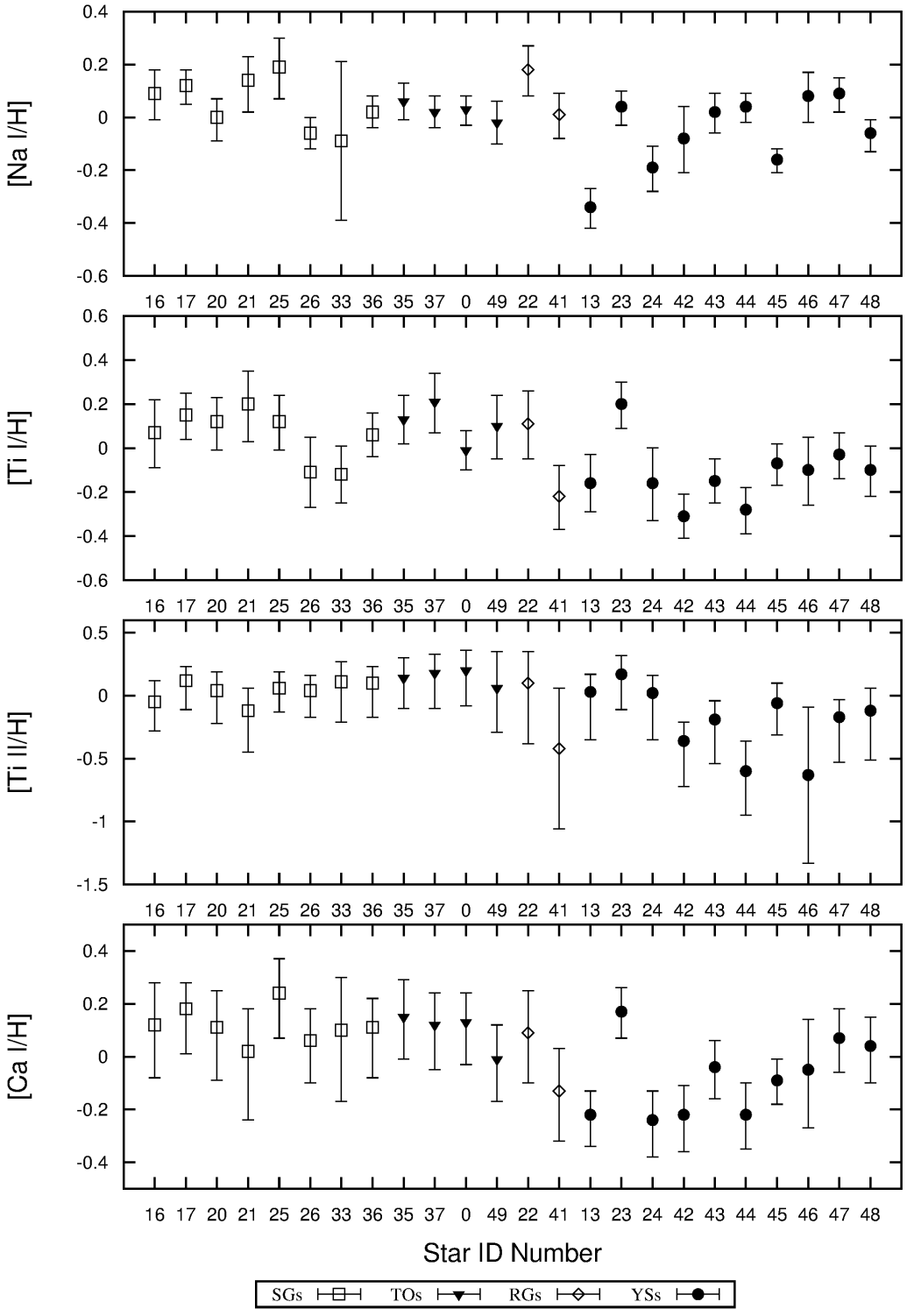

Figure 19: Abundance plots for [Na I/H], [Ti I/H], [Ti II/H] and [Ca I/H].

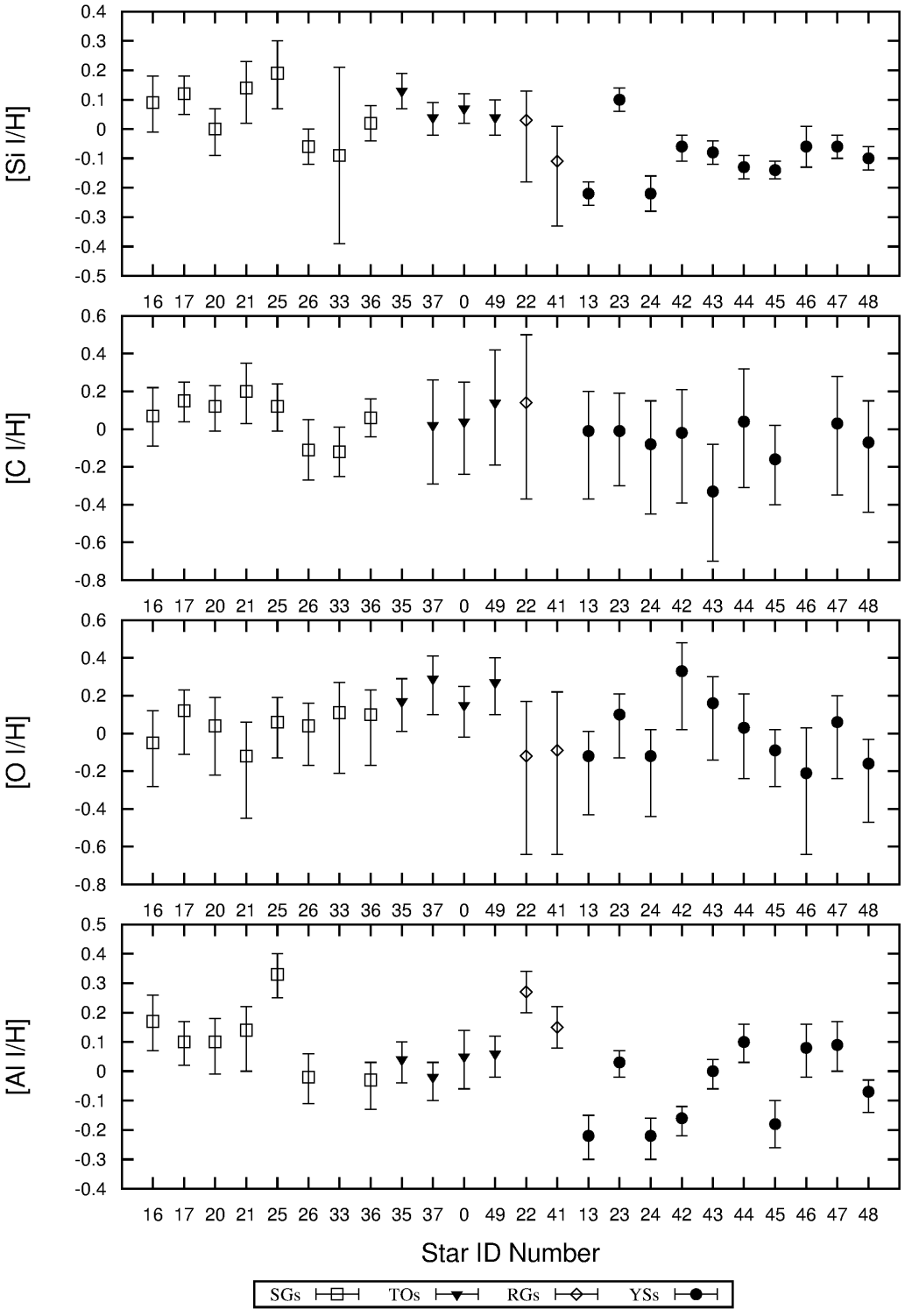

Figure 20: Abundance plots for [Si I/H], [C I/H], [O I/H] and [Al I/H].

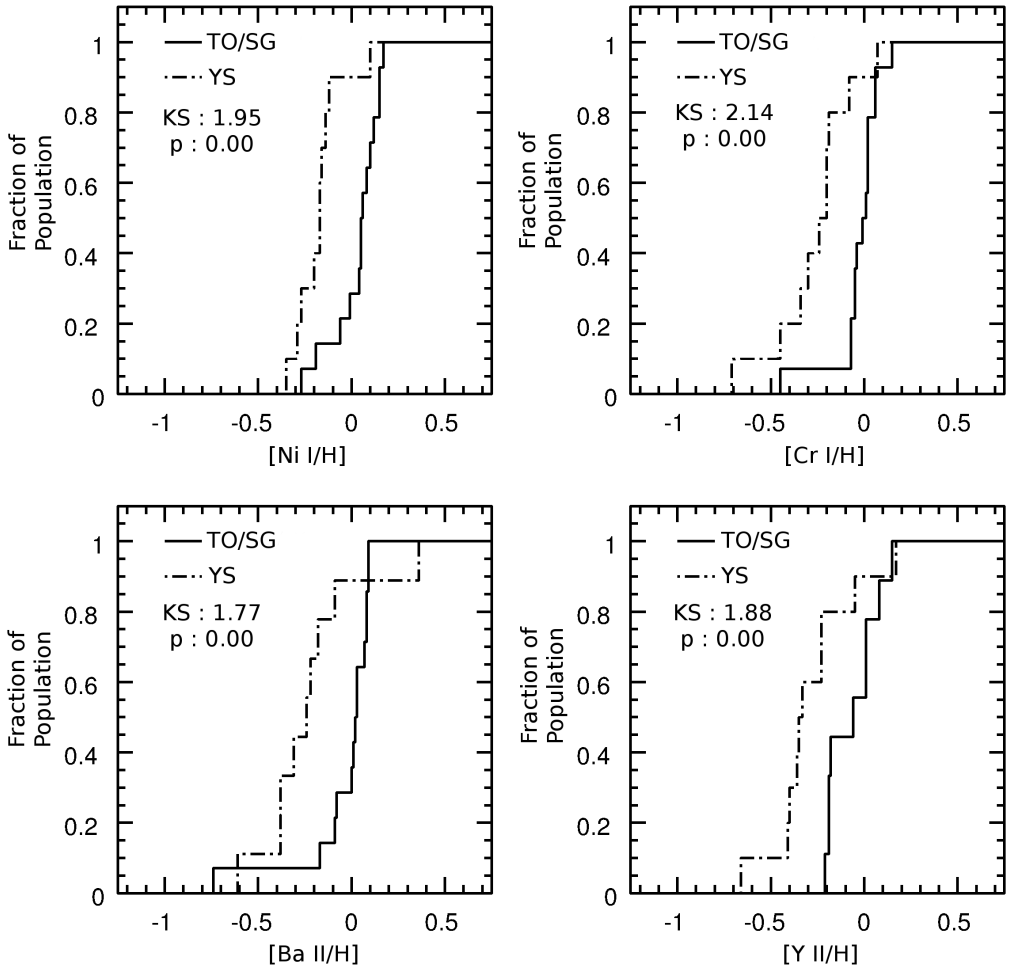

Figure 21: KS test for [Ni I/H], [Cr I/H], [Ba II/H] and [Y II/H].

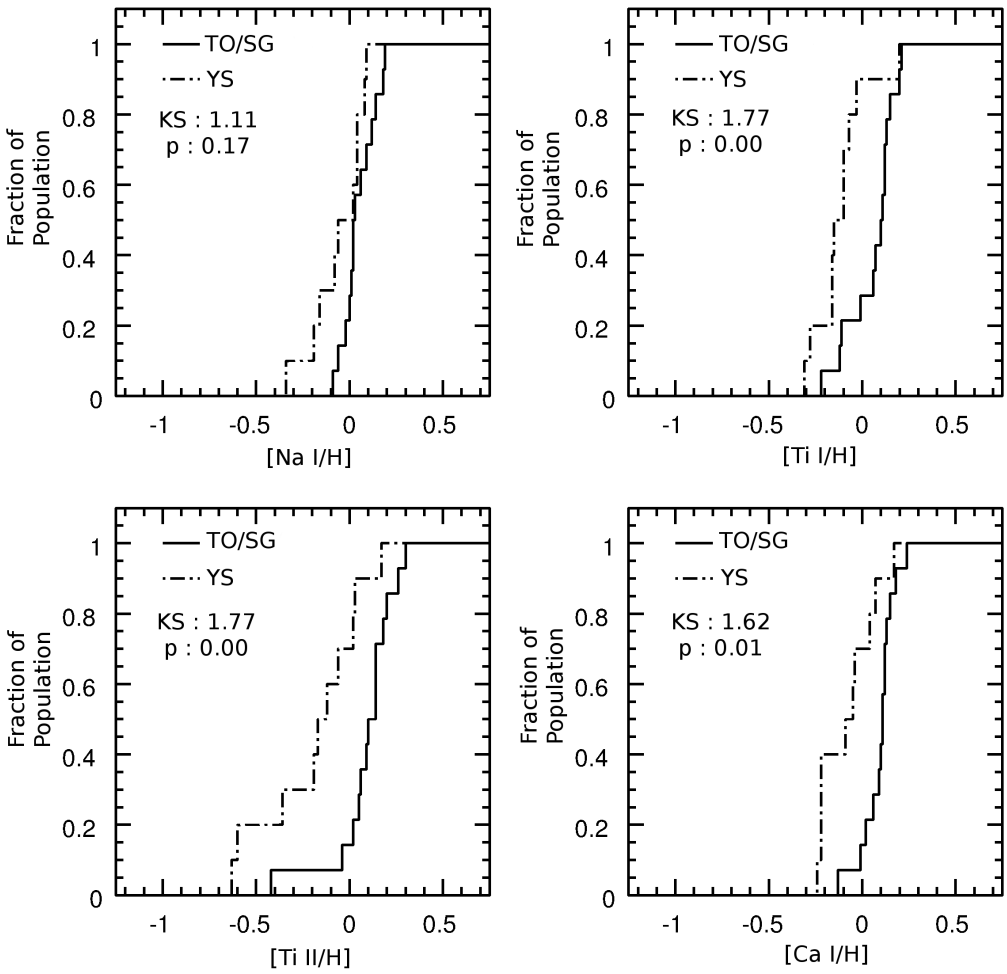

Figure 22: KS test for [Na I/H], [Ti I/H], [Ti II/H] and [Ca I/H].

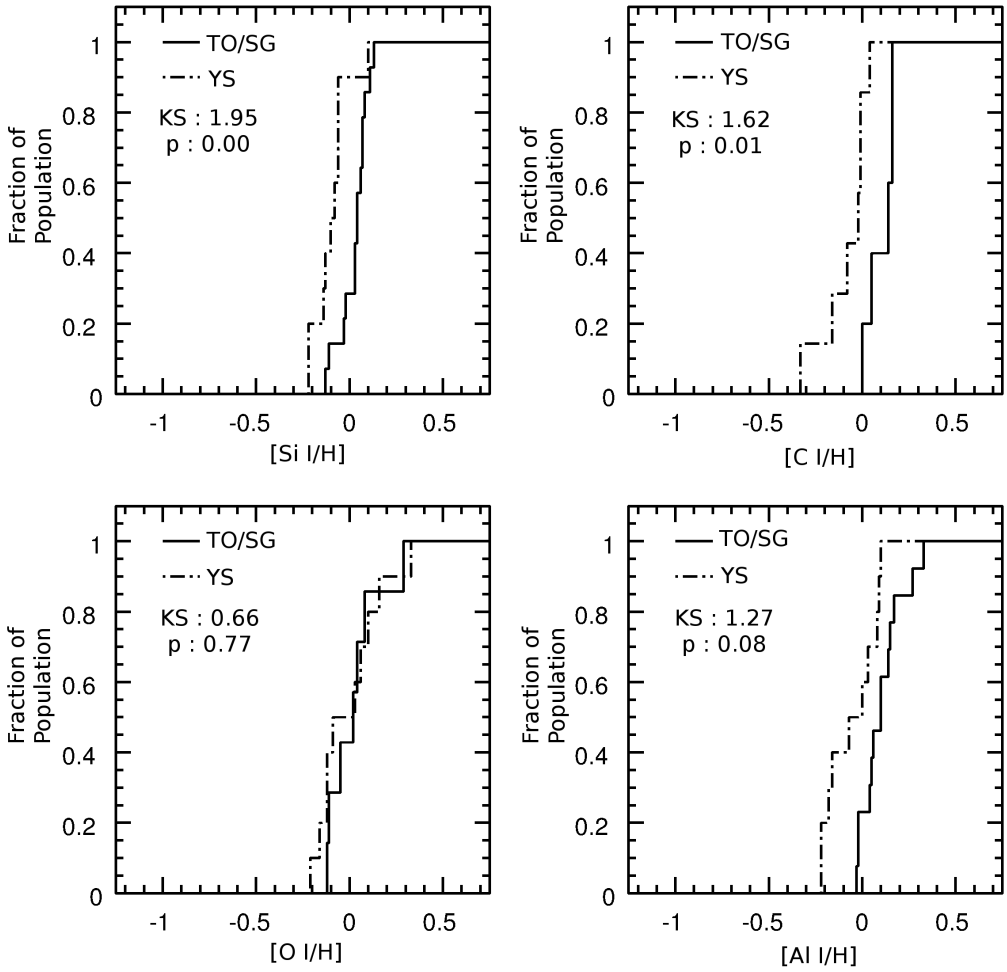

Figure 23: KS test for [Si I/H], [C I/H], [O I/H] and [Al I/H].

Appendix D Notes On Individual Yellow Stragglers

YS 13

Sanders (1977), Yadav et al. (2008) and Balaguer-Núñez et al. (2007) all determined that the proper motion of YS 13 indicated that it is not likely a member of M67. This star appears to have a variable radial velocity with $p = 0.03$, and while it is not a systemic radial velocity of the likely binary system, it does have an average radial velocity of $v_h = 49.2 \pm 0.1$ km/s (consistent with the Yadav et al. (2008) value of $v_{h,y} = 49.6 \pm 0.6$ km/s; no Mathieu et al. (1986) data are available) and a range of 3.1 km/s in the radial velocity measurements made in the present study. The abundance pattern of this star closely resembles that of a field star, HIP 44441, that lies in the general direction of M67 and is approximately 4 Gyr old (Bensby et al., 2004). Considering all of these points, it seems likely that YS 13 is not a member of M67 but is likely a field star in the field of view of the cluster.

YS 23

Though Balaguer-Núñez et al. (2007) find that the proper motion of YS 23 did not confirm cluster membership, Yadav et al. (2008) concluded that this star has a cluster membership probability of 96%. Unfortunately, no Sanders (1977) membership probability data was available for this star. The present study finds that this star has a variable radial velocity with $p = 0.03$, and though it does not represent a systemic velocity of the likely binary system, it has an average radial velocity of $v_h = 36.1 \pm 0.1$ km/s with a range of 2.3 km/s. This average radial velocity is consistent with the cluster mean derived by Mathieu (1983) of 33.5 ± 0.5 km/s. Given that the photometry of YS 23 indicates that it could potentially be a binary comprised of two near turnoff stars, it is perhaps not surprising that the metallicity of this star more closely matches that of the SGs and TOs than the YSs. The proposition that this star is a binary, comprised of two normal cluster members is an attractive one.

YS 24

Sanders (1977), Yadav et al. (2008) and Balaguer-Núñez et al. (2007) each indicate that YS 24 is not a cluster member considering its proper motion with respect to the cluster. However, this work finds that this star has a constant radial velocity to within 2σ and that the average radial velocity of this star ($v_h = 35.8 \pm 0.1$ km/s) is consistent with the cluster mean radial velocity. It is noted however, that the radial velocity determined in the present work is not consistent with the

value determined by Yadav et al. (2008) of $v_{h,y} = 52.9 \pm 0.7$ km/s. Given the likelihood that this star exists as a single star, assuming that this star is a true cluster member, the photometry indicates that it could be a photometric blend of a SG and a MS star roughly 1.5 mag fainter. The metallicity of this star, however, is unlike that of the typical SGs in the current study and is more similar to that of the field star, HIP 44441 (Bensby et al., 2004). In light of these points, it is suggested that YS 24 may simply be a field star with a radial velocity similar to that of M67, and is not a bona fide cluster member.

YS 42

Mathieu & Latham (1986) discuss this star noting that it is a spectroscopic binary with an orbital period of roughly 1500 days. They also note that it possesses three traits supporting the star's membership in M67: 1) this star has proper motion membership probability of 95% (Sanders, 1977) 2) the systemic velocity of this binary (32.7 ± 0.2 km/s) is in agreement with the cluster mean velocity (33.5 ± 0.5 km/s) and 3) this star has a spatial location that appears one core radius from the cluster center. They go on to explore multiple star systems but conclude that a binary of a BS and a RG is not a satisfactory explanation because the composite photometry of such a system would not agree with the *uvby* photometry of Nissen et al. (1987). Mathieu et al. (1990) show that a triple system is also an unsatisfactory explanation because this would ultimately require a triple system of three subgiants with similar colors, and the "correlation-dip depths" are significantly more shallow than those of stars on the giant branch with comparable visual magnitudes as well as main sequence stars with comparable color. They propose that two options remain; either the membership status of YS 42 is incorrect despite its proper motion, radial velocity and spatial location or it truly is an anomalous star, "possibly in an evolutionary phase linked to the blue straggler phenomenon."

Additionally, both Yadav et al. (2008) and Balaguer-Núñez et al. (2007) find that the proper motion of YS 42 indicates that this star is indeed a cluster member. The present work finds that this star exhibits a variable radial velocity ($p = 0.00$) with an average value (not systemic) of $v_h = 30.2 \pm 0.1$ km/s, consistent with the value of Mathieu et al. (1986) ($v_{h,m} = 32.2 \pm 2.2$ km/s), the value of Yadav et al. (2008) ($v_{h,y} = 33.6 \pm 0.6$ km/s) and the cluster mean. The Yadav et al. (2008) photometry of this star indicates that if YS 42 is a blend or binary, one of the components must be bluer than the turnoff (likely a BS) in order to achieve its location blueward of the giant branch. It is noted that for most elements, the abundances of YS 42 tend to be lower than, but not inconsistent with, those of YS 43, a star that is suspected to have experienced RLOF mass transfer

and will be discussed below. If the abundances of YS 42 are significantly lower than those of YS 43, then it could be possible that YS 42 is a contaminating field star, despite its proper motion and radial velocity data. This makes it quite difficult to make any conclusions about YS 42, however, subsequent studies investigating the abundance patterns of mass transfer BSs and the abundance of lithium (Glebbeek et al., 2010) in particular in both YS 42 and YS 43 could provide further clues.

YS 43

Landsman et al. (1997) note that the finding that YS 43 is a single lined spectroscopic binary with a circular orbit and a period of 42.8 days (Mathieu et al., 1990) contradicts the claim of Janes & Smith (1984) that this star could be explained as a photometric binary of a lower giant branch star and a near-turnoff star because such a system would exhibit a secondary correlation peak due to the similar magnitudes of the two components. The present work supports the findings of Mathieu et al. (1990) in that it finds no secondary peak in the cross correlation function indicating that a secondary, should one exist, would have to be significantly fainter than the primary. Landsman et al. (1997) addresses the detection of a companion in YS 43. Specifically, Landsman et al. (1997) notes that the ultraviolet detection of YS 43 (Stecher et al., 1997) "almost certainly implies that the secondary is a hot white dwarf" because if the source of the ultraviolet radiation were more luminous than a WD, the resulting B-V magnitude of YS 43 would not match what is observed. Landsman et al. (1997) follows up on these studies and the suggestion that YS 43 is the result of RLOF mass transfer (Verbunt & Phinney, 1995) by imaging YS 43 with the Goddard High Resolution Spectrograph on Hubble Space Telescope. These observations revealed a broad Lyα absorption feature; further confirmation of the WD nature of the secondary component of YS 43 according to Landsman et al. (1997). Furthermore, from the computation of the WD mass ($\sim 0.22 M_{\odot}$) and the corresponding evolutionary track, Landsman et al. (1997) determine that the mass transfer for this system must have stopped roughly 75 Myr ago and that YS 43 must have evolved to its current location in the CMD from a BS location in that time period.

There is consensus between Sanders (1977), Yadav et al. (2008) and Balaguer-Núñez et al. (2007) that the proper motion of YS 43 indicates that this star is a true cluster member. The current work determines that this star exhibits a variable radial velocity with $p = 0.00$ and finds an average (not systemic) radial velocity of $\mathrm{v_h} = 29.4 \pm 0.9$ km/s, consistent with the value of Mathieu et al. (1986) ($\mathrm{v_{h,m}} = 32.0 \pm 6.3$ km/s) and the cluster mean. The photometry of this star could be achieved by a blend or binary system of a SG and a RG. Additionally, the abundance pattern is not

inconsistent with that found for RG 41 (a radial velocity constant star to within 3σ and Yadav et al. (2008) cluster membership probability of 98%), though it appears to tend to be slightly higher. So it is, perhaps, fortunate that the previous studies of this star have determined the WD nature of the companion in this system, otherwise the photometry and abundance pattern of YS 43 might lead one to believe that it was likely a binary system comprised of a SG and a RG. This, however, is an excellent example of how the true nature of these YSs can be easily misinterpreted.

The determination of the abundances of this star of are particular importance because it is believed to be an evolved BS that has undergone RLOF mass transfer. Recall, however, that no s-process element enhancements were seen for this star. These abundance determinations can still provide a means for comparison with current models dealing with the evolution of mass transfer systems, though. Glebbeek et al. (2010) predicts that lithium may provide the most robust means to distinguish between a collisional or RLOF mass transfer origin for BSs, thus a follow-up study to determine the lithium abundance of this star, and perhaps others in this YS sample may provide observational data to compare with this prediction.

YS 44

Mathieu et al. (1986) found YS 44 to be single lined spectroscopic binary; Mathieu et al. (1990) note that the lack of a detection of the secondary component in this case is unsurprising due to the report of Janes & Smith (1984) that this star could be a binary comprised of a giant star and a fainter near-turnoff. Mathieu et al. (1990) state that such a system would require two stars of equal mass, the secondary would be 1.6 magnitudes fainter than the primary and the velocity separation of the components would only be 10 km/s. They claim that it should be detectable with high resolution, high signal-to-noise spectra. However, the finding in the present study that the location of YS 44 cannot be achieved with the bluest turnoff star (but instead requires that one component be a BS) encourages that the situation for this star be reconsidered.

Sanders (1977), Yadav et al. (2008) and Balaguer-Núñez et al. (2007) all agree that YS 44 is likely a cluster member based on its proper motion. The present study finds that YS 44 exhibits a variable radial velocity ($p = 0.00$), with an average radial velocity of $v_h = 36.5 \pm 0.3$ km/s and a range of roughly 7.0 km/s. This average radial velocity is consistent with that of Mathieu et al. (1986), $v_{h,m} = 33.0 \pm 3.5$ km/s. The Yadav et al. (2008) photometry indicates that the composite photometry of a RG and a BS could achieve the observed location of YS 44 on the CMD, however, the magnitude of the BS would need to be roughly 1.5 magnitudes fainter than the RG to create the

observed photometry. It is possible that the BS could contribute very little to the cross correlation resulting in a single peak in the cross correlation function. However, it cannot be ruled out that the RG could exist in a binary with some other type of unseen companion, and create an optical blend with a BS. An analysis of a RG-BS binary system could further elucidate the validity of this scenario. The the abundance pattern of YS 44 tends to mimic that of RG 41, however, as was seen for YS 43, this particular abundance pattern could be representative of a binary system that was previously subject to mass transfer.

YS 45

Though Balaguer-Núñez et al. (2007) lists YS 45 as a non-member and Sanders (1977) determines a membership probability for this star of 0%, Yadav et al. (2008) determined a membership probability of 84%, so its true proper motion membership status is unclear. The radial velocity data is not entirely helpful in clearing up the matter. The current study finds that YS 45 has a variable radial velocity with $p = 0.00$, an average radial velocity of $v_h = 5.3 \pm 0.2$ km/s and a range of about 4.5 km/s. This radial velocity agrees with both Mathieu et al. (1986) ($v_{h,m} = 3.6 \pm 1.0$ km/s) and Yadav et al. (2008) ($v_{h,y} = 4.0 \pm 0.6$ km/s). Though the radial velocity value is substantially lower than the cluster mean, it is not an unrealistic value for a cluster member to possess, as was seen in §6.1. The observed photometry of YS 45 indicates that if it is, indeed, a cluster member and a binary system, one of the components would necessarily have to be a BS. Again, a BS-RG binary system would need to be analyzed to consider specific parameters. The mass of the components of such a binary system could make the system more susceptible to dyanamical interactions in the cluster (like mass segregation) causing the system to exhibit a peculiar velocity. As previously stated, numerous others have noted the results of such dynamical interactions on BSs in particular in the form of central and/or bimodal spatial distributions of BSs. The abundance pattern of YS 45 is not illuminating either. The Fe-peak and s-process elements tend to be more similar to the normal SGs and TOs, however other elements like Na, Ca, and Si appear more similar to the field star HIP 44441 (Bensby et al., 2004). Thus, further study of this star is recommended before it is determined to be a non-member.

YS 46

The proper motion membership information for YS 46 indicates that it is not a cluster member. Both Sanders (1977) and Yadav et al. (2008) report membership probabilities of 0% and Balaguer-Núñez et al. (2007) also reports this star as a non-member. The radial velocity information

in the present study agrees with the findings of Mathieu et al. (1986) that this star is a double lined spectroscopic binary. An average radial velocity was computed for both correlation peaks in the cross correlation function, however, keep in mind that this is not a computation of the systemic radial velocity of the binary system, as previously stated for the other variable radial velocity stars. $v_{h,A} = 49.3 \pm 1.3$ km/s was computed for the larger of the two cross correlation peaks (component A) and $v_{h,B} = 54.9 \pm 4.3$ km/s was computed for the smaller of the two peaks (component B). The average radial velocities of the two components are a bit higher than the cluster mean, however, they are not completely unrealistic radial velocity values for cluster members as was seen in §6.1 and the values for both componets range over roughly 29 km/s. The observed photometry for this binary indicates that it must comprise a RG and a BS with roughly the same magnitude. Abundances were computed for component A. The abundance pattern for this star is quite perplexing. Some of the Fe-peak elements match those of the field star HIP 44441 (Bensby et al., 2004) while others appear similar to the SGs and TOs. The same is true for the s-process elements as well. It is noted, however, that the abundance values computed for this star are likely unreliable given the star's double lined nature.

YS 47

Sanders (1977) and Yadav et al. (2008) both give cluster membership probabilities of 0% for YS 47 and Balaguer-Núñez et al. (2007) also reports it as a non-member. The present work finds that it has a variable radial velocity with $p = 0.00$, an average radial velocity of $v_h = 94.4 \pm 0.2$ km/s and a range of only 3 km/s. This radial velocity is significantly different than that of the cluster mean, and this value is not a realistic value for other cluster members as was shown in §6.1. Furthermore, assuming that YS 47 is a binary system, the observed photmetry indicates that it must be comprised of a RG and a BS that is roughly 0.7 mag fainter, but the metallicity for this star is significantly higher than that of RG 41. It is also significantly higher than that of the field star HIP 44441 (Bensby et al., 2004). Because the proposed BS component could contribute significantly to the observed spectrum, an abundance analysis of the BSs may lead to further insights on the true nature of this object, however it is expected that this star is likely a contaminating field star.

YS 48

Sanders (1977) and Yadav et al. (2008) both give membership probabilities for YS 48 of 0%. Balaguer-Núñez et al. (2007) also lists this star as non-member. The present study determined an average radial velocity for this star of $v_h = 12.0 \pm 0.1$ km/s which is substantially lower than the

cluster mean, but as was presented in §6.1, is not an unrealistic value for other cluster members. Keep in mind, however, that the present work also found that the radial velocity of this star is constant to 3σ. These data support the hypothesis that this star is simply a contaminating field star, however, note that the abundance pattern for this star is consistently higher than that of the field star HIP 44441 of Bensby et al. (2004). The possibility that this star is a cluster member of some anomalous evolutionary state is unlikely. However, the possibility that this star is a normal cluster member that forms an optical blend with some other object cannot be ruled out. If YS 48 is a normal cluster member in an optical blend, the other component would have to be a BS in order to generate the observed photometry of this object.

Bibliography

Balaguer-Núñez, L., Galadí-Enríquez, D., & Jordi, C. 2007, A&A, 470, 585

Bensby, T., Feltzing, S., Lundstroem, I., & Ilyin, I. 2004, VizieR Online Data Catalog, 343, 30185

Böhm-Vitense, E. 1989, Introduction to stellar astrophysics. Vol. 2. Stellar atmospheres.

Bressan, A., Marigo, P., Girardi, L., Salasnich, B., Dal Cero, C., Rubele, S., & Nanni, A. 2012, MNRAS, 427, 127

Bubar, E. J. & King, J. R. 2010, AJ, 140, 293

Clark, L. L., Sandquist, E. L., & Bolte, M. 2004, AJ, 128, 3019

Edvardsson, B., Andersen, J., Gustafsson, B., Lambert, D. L., Nissen, P. E., & Tomkin, J. 1993, A&A, 275, 101

Eggen, O. J. & Sandage, A. R. 1964, ApJ, 140, 130

Ferraro, F. R., Beccari, G., Rood, R. T., Bellazzini, M., Sills, A., & Sabbi, E. 2004, ApJ, 603, 127

Ferraro, F. R., Clementini, G., Fusi Pecci, F., & Buonanno, R. 1991, MNRAS, 252, 357

Ferraro, F. R., Clementini, G., Fusi Pecci, F., Sortino, R., & Buonanno, R. 1992, MNRAS, 256, 391

Ferraro, F. R., Paltrinieri, B., Fusi Pecci, F., Cacciari, C., Dorman, B., Rood, R. T., Buonanno, R., Corsi, C. E., Burgarella, D., & Laget, M. 1997, A&A, 324, 915

Friel, E. D. & Boesgaard, A. M. 1992, ApJ, 387, 170

Friel, E. D. & Janes, K. A. 1993, A&A, 267, 75

Garcia Lopez, R. J., Rebolo, R., & Beckman, J. E. 1988, PASP, 100, 1489

Geller, A. M., Hurley, J. R., & Mathieu, R. D. 2013, AJ, 145, 8

Geller, A. M. & Mathieu, R. D. 2011, Nature, 478, 356

—. 2012, AJ, 144, 54

Geller, A. M., Mathieu, R. D., Harris, H. C., & McClure, R. D. 2008, AJ, 135, 2264

Glebbeek, E., Sills, A., Hu, H., & Stancliffe, R. J. in , American Institute of Physics Conference Series, Vol. 1314, American Institute of Physics Conference Series, ed. V. KalogeraM. van der Sluys, 113–119

Gray, D. F. 2005, The Observation and Analysis of Stellar Photospheres

Gray, R. O., McGahee, C. E., Griffin, R. E. M., & Corbally, C. J. 2011, AJ, 141, 160

Hesser, J. E., McClure, R. D., Hawarden, T. G., Cannon, R. D., von Rudloff, R., Kruger, B., & Egles, D. 1984, PASP, 96, 406

Hills, J. G. & Day, C. A. 1976, Astrophys. Lett., 17, 87

Hobbs, L. M. & Thorburn, J. A. 1991, AJ, 102, 1070

Hurley, J. R., Pols, O. R., Aarseth, S. J., & Tout, C. A. 2005, MNRAS, 363, 293

Jacobson, H. R., Pilachowski, C. A., & Friel, E. D. 2011, AJ, 142, 59

Janes, K. A. & Smith, G. H. 1984, AJ, 89, 487

King, J. R. 1997, PASP, 109, 776

King, J. R., Stephens, A., Boesgaard, A. M., & Deliyannis, C. 1998, AJ, 115, 666

Kinman, T. D. 1965, ApJ, 142, 655

Kurucz, R. L. 1970, SAO Special Report, 309

Kurucz, R. L. in , IAU Symposium, Vol. 149, The Stellar Populations of Galaxies, ed. B. BarbuyA. Renzini, 225

Landsman, W., Aparicio, J., Bergeron, P., Di Stefano, R., & Stecher, T. P. 1997, ApJ, 481, L93

Leonard, P. J. T. 1996, ApJ, 470, 521

Mapelli, M., Sigurdsson, S., Colpi, M., Ferraro, F. R., Possenti, A., Rood, R. T., Sills, A., & Beccari, G. 2004, ApJ, 605, L29

Mathieu, R. D. 1983, PhD thesis, California Univ., Berkeley.

Mathieu, R. D. & Latham, D. W. 1986, AJ, 92, 1364

Mathieu, R. D., Latham, D. W., & Griffin, R. F. 1990, AJ, 100, 1859

Mathieu, R. D., Latham, D. W., Griffin, R. F., & Gunn, J. E. 1986, AJ, 92, 1100

McClure, R. D. 1983, ApJ, 268, 264

McCrea, W. H. 1964, MNRAS, 128, 147

Meyer, B. S. 1994, ARA&A, 32, 153

Montgomery, K. A., Marschall, L. A., & Janes, K. A. 1993, AJ, 106, 181

Nissen, P. E., Twarog, B. A., & Crawford, D. L. 1987, AJ, 93, 634

North, P., Berthet, S., & Lanz, T. 1994, A&A, 292, 350

North, P. & Lanz, T. 1991, A&A, 251, 489

Önehag, A., Gustafsson, B., & Korn, A. 2014, A&A, 562, A102

Pietrinferni, A., Cassisi, S., Salaris, M., & Castelli, F. 2004, ApJ, 612, 168

Preston, G. W. & Sneden, C. 2000, AJ, 120, 1014

Preston, G. W. & Sneden, C. The A-Star Puzzle, ed. , J. ZverkoJ. ZiznovskyS. J. Adelman & W. W. Weiss, 403–410

Prialnik, D. 2000, An Introduction to the Theory of Stellar Structure and Evolution

Racine, R. 1971, ApJ, 168, 393

Sandage, A. R. 1953, AJ, 58, 61

Sanders, W. L. 1977, A&AS, 27, 89

Sills, A., Karakas, A., & Lattanzio, J. 2009, ApJ, 692, 1411

Sneden, C., Bean, J., Ivans, I., Lucatello, S., & Sobeck, J. 2012a, MOOG: LTE line analysis and spectrum synthesis, astrophysics Source Code Library

Sneden, C., Preston, G. W., & Cowan, J. J. 2003, ApJ, 592, 504

Sneden, C., Uomoto, A., Cottrell, P., & Fitzpatrick, M. 2012b, SPECTRE: Manipulation of single-order spectra, astrophysics Source Code Library

Stecher, T. P., Cornett, R. H., Greason, M. R., Landsman, W. B., Hill, J. K., Hill, R. S., Bohlin, R. C., Chen, P. C., Collins, N. R., Fanelli, M. N., Hollis, J. I., Neff, S. G., O'Connell, R. W., Offenberg, J. D., Parise, R. A., Parker, J., Roberts, M. S., Smith, A. M., & Waller, W. H. 1997, PASP, 109, 584

Stryker, L. L. 1993, PASP, 105, 1081

Tautvaisiene, G., Edvardsson, B., Tuominen, I., & Ilyin, I. 2000, VizieR Online Data Catalog, 336, 499

Taylor, B. J. 2007, AJ, 133, 370

Tian, B., Deng, L., Han, Z., & Zhang, X. B. 2006, A&A, 455, 247

van den Bergh, S., Demers, S., & Kunkel, W. E. 1980, ApJ, 239, 112

Verbunt, F. & Phinney, E. S. 1995, A&A, 296, 709

Woods, T. E., Ivanova, N., van der Sluys, M. V., & Chaichenets, S. 2012, ApJ, 744, 12

Yadav, R. K. S., Bedin, L. R., Piotto, G., Anderson, J., Cassisi, S., Villanova, S., Platais, I., Pasquini, L., Momany, Y., & Sagar, R. 2008, A&A, 484, 609